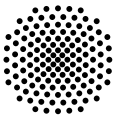

University of Stuttgart
Institute for Theoretical Physics I

Application of Machine Learning to Find Exceptional Points

By

Patrick Egenlauf

Institute for Theoretical Physics I
University of Stuttgart
Pfaffenwaldring 57
70569 Stuttgart

First examiner: Prof. Dr. Jörg Main
Second examiner: Prof. Dr. Christian Holm

This thesis is submitted for the degree of
Master of Science

July 12, 2023

Table of contents

List of Abbreviations

CB conduction band

CCC central-cell corrections

c.p. cyclic permutation

EP exceptional point

GP Gaussian process

GPR Gaussian process regression

LML log marginal likelihood

LO longitudinal optical

RBF radial basis function

SE squared exponential

VB valence band

1 Introduction

In open quantum systems, resonances can occur. These are quasi-bound states which can decay. By introducing a complex scaling, e.g. according to Reinhardt [1], and thus non-Hermitian operators, the complex energy eigenvalues of the resonances can be calculated. Here, the real part represents their energy, while the imaginary part unveils their lifetime.

Resonances can degenerate, where a special case is the so-called exceptional point (EP) at which not only the eigenvalues but also the eigenvectors degenerate. Thus, the two resonances coalesce at the EP. An isolated EP can be described by a two-dimensional matrix model [2]. A property of such an EP is that the two associated eigenvalues exchange their positions after one adiabatic orbit in parameter space around the EP. In 2007 the existence of these EPs was proven for the hydrogen atom in electric and magnetic fields by Cartarius [3]. Due to limitations especially in magnetic field strengths, EPs in the hydrogen atom are not experimentally accessible.

In 2014, a remarkable discovery by Kazimierczuk *et al.* [4] revealed a mesmerizing hydrogen-like spectrum within cuprous oxide (Cu_2O). This revelation stemmed from the resemblance between an exciton, a quasi-particle in a semiconductor consisting of electron and hole, and their atomic counterpart, the hydrogen atom. However, the fact that the excitons are environed by Cu_2O necessitated consideration of the band structure to precisely describe the observed spectrum. This discovery kindled excitement as it provided a rare opportunity to bridge the realms of experimental and theoretical physics, inviting an enthralling dialogue between theory and experiment. For Cu_2O the field strengths to observe EPs of resonances with small quantum numbers are much lower compared to the field strengths for the hydrogen atom, which is why it is favorable to find EPs in this system. This was already done for a hydrogen-like model, but to obtain experimentally comparable results the above mentioned band structure terms need to be considered. However, this increases the computational cost drastically for each diagonalization of the Hamiltonian due to its complexity. The existing methods to find EPs are based on a Taylor expansion around the EP [5, 6]. Due to the computational expensive diagonalizations of the Hamiltonian, these methods are inefficient or even not

applicable. Hence, a new method is required to accurately and efficiently identify EPs in Cu_2O.

Inspired by the remarkable advances in machine learning, especially within the realm of physics, a novel method on the foundation of Gaussian process regression (GPR) [7] is developed. As a prominent member of the supervised machine learning family, GPR serves as a powerful and innovative approach to predict the positions of EPs in Cu_2O. The used data to train a GPR model is obtained by simulations. Hence, the error is only due to numerical inaccuracies, which can be neglected. Unlike neural networks, GPR offers the advantage of precisely passing through the provided training points, which is a key motivation for its utilization. Yet, the optimization of the searching process goes beyond the new method. An efficient algorithm is devised to enhance the search for EPs in Cu_2O, which contributes to the discovery of promising EPs and thus enables a possible experimental verification of these data.

1.1 Structure of this thesis

The present thesis is organized into four primary parts. In Chapter 2, the theoretical basics necessary to understand this thesis are presented. First, excitons and the semiconductor cuprous oxide are introduced in Section 2.1. To account for all effects on the system, the Hamiltonian of excitons in Cu_2O is described in Section 2.2. Section 2.3 is about resonances, which occur, when applying external electric and magnetic fields to the system. The numerical method to diagonalize the exciton Hamiltonian of Cu_2O is explained in Section 2.4. EPs are presented in Section 2.5 by means of a simple example, and the existing methods to find them are briefly summarized.

To develop the new method, basic knowledge of GPR is required. This is provided in Chapter 3.

The GPR method is developed gradually by means of low-dimensional matrix models in Chapter 4. In Section 4.1, the stepwise grouping algorithm is developed to acquire the initial training set. A two-dimensional simple example as well as a five-dimensional matrix model serves to demonstrate the GPR model training in Section 4.2. In higher-dimensional systems, it is not straightforward to select the eigenvalues belonging to the EP in each iteration step, so a similarity measure is introduced in Section 4.3 to solve this problem. The iterative process is constructed and the new GPR method is applied to the matrix models. To terminate the procedure, possible convergence criteria are discussed in Section 4.4 and convergence tests are performed to determine the accuracy of the predictions.

The results are presented in Chapter 5. First, the differences to the matrix models accompanied by the consideration of the external electric and magnetic fields are introduced. In Section 5.1, the GPR method is applied to Cu_2O and the results are shown. To minimize the number of diagonalizations, in Section 5.2, the convergence radius of the method is investigated. All results, including the identified EPs using the GPR method as well as additional insights associated with the stepwise grouping algorithm are presented.

All major points of the previous Chapters are summarized in Chapter 6 and a short outlook for possible further studies is given.

Appendix A contains an implementation of the stepwise grouping algorithm in Python. Further details on the optimization of the training process required to apply the GPR method to Cu_2O are provided in Appendix B. A separate conclusion in German is also included.

2 | Theoretical Basics

In this chapter the theoretical basics to understand this thesis are introduced in separate sections. For the sake of clarity, the different topics are not or only weakly connected with each other. First, the physical system, i.e. excitons in cuprous oxide, is introduced in Section 2.1. To get an accurate description of the system, the band structure of Cu_2O needs to be considered, which is explained in Section 2.2. Section 2.3 is about resonances. After introducing all relevant parameters, the method to obtain the eigenvalues of the exciton Hamiltonian is explained in Section 2.4. Then, exceptional points (EPs) are discussed in Section 2.5 by means of an example and the methods to find them are shown.

2.1 Excitons in cuprous oxide

Cuprous oxide Cu_2O is a red-colored crystal in which copper and oxygen ions are arranged in a cubic lattice, as depicted in Figure 2.1a [8]. The copper ions have a face-centered cubic structure, whereas the oxygen ions have a body-centered cubic structure. The unit cell is highlighted in green and consists of four copper ions and one oxygen ion. Figure 2.1b shows a part of the band structure of Cu_2O. The transitions of the yellow and green excitons, relevant for this thesis, are plotted with the respective color.

The band structure consists of valence bands (VBs) and conduction bands (CBs). In the ground state all electrons are in the VBs and none of them in the CBs, making it non-conducting [9]. Electrons can be excited from the VB into the CB by supplying energy, e.g. light. A positive charged hole remains in the VB which interacts with the excited electron via the Coulomb interaction. This hydrogen-like quasi-particle consisting of electron and hole is called exciton and can be described in a simple hydrogen-like model by the Hamiltonian

$$\mathcal{H} = E_\mathrm{g} + \frac{\boldsymbol{p}_\mathrm{e}^2}{2m_\mathrm{e}} + \frac{\boldsymbol{p}_\mathrm{h}^2}{2m_\mathrm{h}} - \frac{e^2}{4\pi\varepsilon_0\varepsilon|\boldsymbol{r}_\mathrm{e} - \boldsymbol{r}_\mathrm{h}|} \,, \tag{2.1}$$

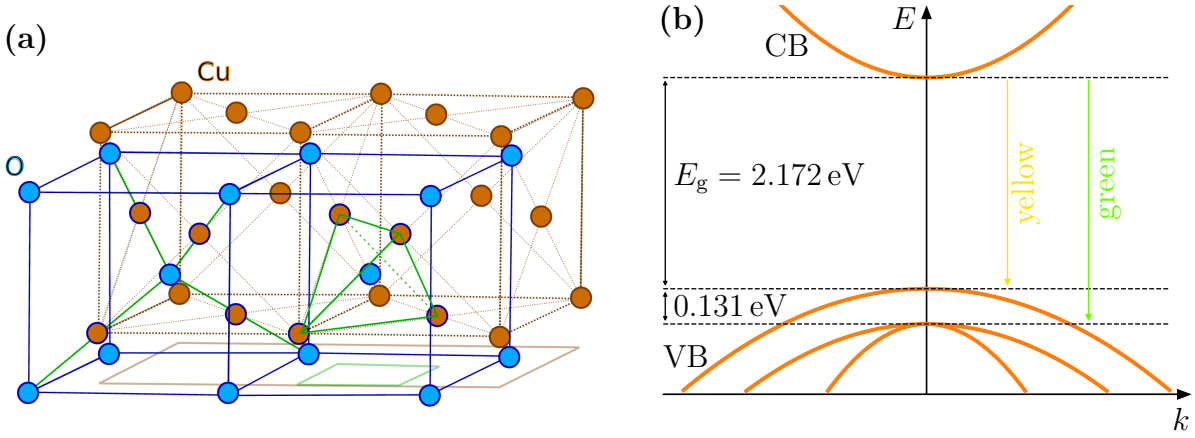

Figure 2.1: **(a)** The crystal structure of Cu_2O consists of two shifted lattices of copper (brown) and oxygen ions (blue), the former having a face-centered cubic structure and the latter a body-centered cubic structure. Four copper ions and one oxygen ion form the unit cell, which is highlighted in green. Taken from [10]. **(b)** The band structure of Cu_2O is made up of several valence bands (VBs) and conduction bands (CBs). These are separated by the band gap energy E_g. The relevant transitions are from the two highest VBs to the lowest CB, which form the yellow and green excitons.

where E_g is the band gap between VB and CB, $\boldsymbol{p}_{e/h}$ are the momenta of the electron (e) and the hole (h) and $m_{e/h}$ the corresponding masses [10]. Thus, the second and third terms define the kinetic energy of the respective particle. The last term represents the Coulomb interaction, in which ε is the dielectric constant that takes into account the screening of the crystal. The similarity to the Hamiltonian of hydrogen can be visualized by introducing the total mass $M = m_e + m_h$, the reduced mass $\mu = \frac{m_e m_h}{M}$, as well as relative and center-of-mass coordinates [9]. To further illustrate the analogy to the hydrogen atom, the Bohr radius a_{exc} and the Rydberg energy $E_{R,exc}$ of the exciton are given by

$$a_{exc} = a_0 \frac{m_0 \varepsilon}{\mu} \quad \text{and} \quad E_{R,exc} = E_{R,H} \frac{\mu}{m_0 \varepsilon} \,, \tag{2.2}$$

where a_0 and $E_{R,H}$ are the corresponding quantities of hydrogen [10]. Due to the similar mass of electron and hole, the reduced mass cannot be simplified to $\mu_H \approx m_e$ as in the hydrogen model. Both quantities in Equation (2.2) can be calculated by inserting material parameters of Cu_2O which results in [4, 11]

$$a_{exc} = 1.11\,\text{nm}\,, \tag{2.3a}$$

$$E_{R,exc} = 92\,\text{meV} \ll E_g\,. \tag{2.3b}$$

To accurately describe excitons in Cu_2O, the hydrogen-like model is not sufficient because the band structure has to be taken into account. Applying external magnetic and electric fields also affects the system. Thus, the corrections which are necessary for an accurate description are explained in the next section.

2.2 Hamiltonian of Cu_2O

The yellow and the green excitons as depicted in Figure 2.1b can be described by the Hamiltonian [12]

$$\mathcal{H} = E_\mathrm{g} + \mathcal{H}_\mathrm{e}(\boldsymbol{p}_\mathrm{e}) + \mathcal{H}_\mathrm{h}(\boldsymbol{p}_\mathrm{h}) + V(\boldsymbol{r}_\mathrm{e} - \boldsymbol{r}_\mathrm{h}) + V_\mathrm{CCC}(\boldsymbol{r})\,. \tag{2.4}$$

Here, E_g is the band gap energy also shown in Figure 2.1b and $\mathcal{H}_\mathrm{e/h}$ is the kinetic energy term for the electron and hole, respectively. The interaction between electron and hole is considered by $V(\boldsymbol{r}_\mathrm{e} - \boldsymbol{r}_\mathrm{h})$ and for excitons with small spatial extensions the central-cell corrections $V_\mathrm{CCC}(\boldsymbol{r})$ are included as well [8, 10].

2.2.1 Band structure terms

The point group of Cu_2O is the octahedral group O_h. Expressed by the symbol $\Gamma_i^\pm$, the irreducible representations utilized in hereafter are further elucidated in reference [13]. The Γ_6^+ CB in Cu_2O, i.e. the lowest CB, is approximately parabolic, which is why only the electron mass is modified compared to the one in vacuum m_0, leading to the kinetic energy term of the electron [8]

$$\mathcal{H}_\mathrm{e} = \frac{\boldsymbol{p}_\mathrm{e}^2}{2m_\mathrm{e}}\,. \tag{2.5}$$

Due to non-parabolic VBs the kinetic term of the hole looks much more complicated. The Γ_5^+ VB is split into the highest Γ_7^+ VB and the Γ_8^+ one underneath due to the spin-orbit coupling [8]. At the Γ-point, which is the maximum of the VB in Figure 2.1b, the VB is threefold degenerate which can be described by a quasi-spin $\boldsymbol{I}$ in the three-dimensional Hilbert space. The three orbital Bloch functions xy, yz, and zx, which transform in accordance with the Γ_5^+ symmetry group, are conveniently denoted by such a quasi-spin [10]. Considering also the hole spin $\boldsymbol{S}_\mathrm{h}$ results in a sixfold degeneracy. As already mentioned the spin-orbit coupling divides the band leading to the Γ_7^+ band with a twofold degeneracy and the lower Γ_8^+ band, which is fourfold degenerate.

Luttinger and Kohn [14] developed a suitable framework for treating degenerate valence bands, as discussed in this context. They employed a perturbation-based approach

to eliminate interband coupling terms from the kinetic energy description, resulting in an effective Hamiltonian confined to the relevant bands of interest [8]. The interaction with other bands is accounted for by adjusting the coupling terms between the studied bands through a process known as renormalization. By considering the crystal's symmetry, the relatively straightforward Suzuki-Hensel Hamilton operator [15], with only a few free parameters, remains. These parameters, referred to as Luttinger parameters, can be determined by fitting the Suzuki-Hensel Hamiltonian to spin-DFT calculations, specifically for Cu_2O [16, 17].

The kinetic energy model for the hole is based on the Suzuki-Hensel Hamiltonian, which incorporates the fitted parameters. This leads to

$$\begin{aligned}\mathcal{H}_\mathrm{h}\left(\boldsymbol{p}_\mathrm{h}\right) = \mathcal{H}_\mathrm{so} + \frac{1}{2\hbar^2 m_0}\Big\{&\hbar^2\left(\gamma_1 + 4\gamma_2\right)\boldsymbol{p}_\mathrm{h}^2 \\ &+ 2\left(p_1 + 2p_2\right)\boldsymbol{p}_\mathrm{h}^2\left(\boldsymbol{I}\cdot\boldsymbol{S}_\mathrm{h}\right) \\ &- 6\gamma_2\left(p_{\mathrm{h}1}^2\boldsymbol{I}_1^2 + \text{c.p.}\right) - 12p_2\left(p_{\mathrm{h}1}^2\boldsymbol{I}_1\boldsymbol{S}_{\mathrm{h}1} + \text{c.p.}\right) \\ &- 12\gamma_3\left(\left\{p_{\mathrm{h}1}, p_{\mathrm{h}2}\right\}\left\{\boldsymbol{I}_1, \boldsymbol{I}_2\right\} + \text{c.p.}\right) \\ &- 12p_3\left(\left\{p_{\mathrm{h}1}, p_{\mathrm{h}2}\right\}\left(\boldsymbol{I}_1\boldsymbol{S}_{\mathrm{h}2} + \boldsymbol{I}_2\boldsymbol{S}_{\mathrm{h}1}\right) + \text{c.p.}\right)\Big\}\,,\end{aligned} \tag{2.6}$$

with the anti-commutator $\{a, b\} = \frac{1}{2}(ab + ba)$, the momenta $\boldsymbol{p}_{\mathrm{e/h}}$ of electron and hole, the Luttinger parameters γ_i and p_i, cyclic permutation (c.p.) and the spin-orbit coupling term

$$\mathcal{H}_\mathrm{so} = \frac{2}{3}\Delta\left(1 + \frac{1}{\hbar^2}\boldsymbol{I}\cdot\boldsymbol{S}_\mathrm{h}\right)\,. \tag{2.7}$$

The Cartesian coordinates x, y, and z are represented by the indices $i = 1, 2, 3$ pertaining to the Luttinger parameters, momenta as well as quasi- and hole spin. By introducing the effective hole spin $\boldsymbol{J} = \boldsymbol{I} + \boldsymbol{S}_\mathrm{h}$, the spin-orbit coupling Hamiltonian is diagonal. The yellow and green series illustrated in Figure 2.1b are thus defined by $J = \frac{1}{2}$ and $J = \frac{3}{2}$, respectively.

Interaction between electron and hole is described by the screened Coulomb potential

$$V(\boldsymbol{r}_\mathrm{e} - \boldsymbol{r}_\mathrm{h}) = -\frac{e^2}{4\pi\varepsilon_0\varepsilon|\boldsymbol{r}_\mathrm{e} - \boldsymbol{r}_\mathrm{h}|}\,, \tag{2.8}$$

with the dielectric constant $\varepsilon = \varepsilon_{\mathrm{s}1}$ in the low-frequency regime and the positions $\boldsymbol{r}_{\mathrm{e/h}}$ of electron and hole, respectively.

2.2.2 Center-of-mass transformation

There is a translational symmetry in the system, since the Hamiltonian (2.4) depends only on the difference $\boldsymbol{r}_\mathrm{e} - \boldsymbol{r}_\mathrm{h}$ between the two coordinates, making the center-of-mass momentum a good quantum number [8]. To take advantage of this, the relative and center-of-mass coordinates [10, 18–20]

$$\boldsymbol{r} = \boldsymbol{r}_\mathrm{e} - \boldsymbol{r}_\mathrm{h}\,, \qquad \boldsymbol{R} = \frac{m_\mathrm{e}}{m_\mathrm{e}+m_\mathrm{h}}\boldsymbol{r}_\mathrm{e} + \frac{m_\mathrm{h}}{m_\mathrm{e}+m_\mathrm{h}}\boldsymbol{r}_\mathrm{h}\,, \tag{2.9a}$$

$$\boldsymbol{p} = \frac{m_\mathrm{h}}{m_\mathrm{e}+m_\mathrm{h}}\boldsymbol{p}_\mathrm{e} - \frac{m_\mathrm{e}}{m_\mathrm{e}+m_\mathrm{h}}\boldsymbol{p}_\mathrm{h}\,, \qquad \boldsymbol{P} = \boldsymbol{p}_\mathrm{e} + \boldsymbol{p}_\mathrm{h} \tag{2.9b}$$

are incorporated to streamline the description. Here, $\boldsymbol{r}$ is the relative coordinate and $\boldsymbol{R}$ the center-of-mass coordinate with their respective momenta $\boldsymbol{p}$ and $\boldsymbol{P}$.

2.2.3 Central-cell corrections

For the accurate modeling of excitons with small spatial extension, such as states with a principal quantum number of $n \leq 2$, the central-cell corrections (CCC) $V_\mathrm{CCC}(\boldsymbol{r})$ need to be considered as additional terms in the Hamiltonian (2.4) [8].

Due to their opposing charges, the electron and hole that make up an exciton interact via the Coulomb potential. When the relative motion of the electron and hole is slow in comparison to the motion of the ionic cores of the crystal, the crystal environment modifies this interaction, resulting in the screened dielectric constant ε_s. This requirement is not met for small principal quantum numbers, necessitating further modifications to the dielectric constant. The electronic dielectric constant ε_b must be used in its place if the motion of the electron and hole is significantly faster than that of the ionic cores. At the frequency associated with a specific optical phonon branch, which governs the relevant motion of the crystal's cores, the transition between both regimes occurs. The excitons of the yellow and green series in cuprous oxide are influenced by two relevant longitudinal optical (LO) branches. Modeling the behavior of the dielectric constant in the transition areas is necessary for an accurate description.

Haken derived and discussed the fundamental potential arising from the Fröhlich interaction involving a single phonon branch [21–23]. Generalizing this potential to account for two phonon branches yields [24]

$$V^\mathrm{H}(r) = -\frac{e^2}{4\pi\varepsilon_0 r}\left[\frac{1}{\varepsilon_\mathrm{s1}} + \frac{1}{2\varepsilon_1^*}\left(\mathrm{e}^{-\frac{r}{\rho_\mathrm{h1}}} + \mathrm{e}^{-\frac{r}{\rho_\mathrm{e1}}}\right) + \frac{1}{2\varepsilon_2^*}\left(\mathrm{e}^{-\frac{r}{\rho_\mathrm{h2}}} + \mathrm{e}^{-\frac{r}{\rho_\mathrm{e2}}}\right)\right]\,, \tag{2.10}$$

where ε_i^* is given by

$$\frac{1}{\varepsilon_i^*} = \frac{1}{\varepsilon_{\mathrm{b}i}} - \frac{1}{\varepsilon_{\mathrm{s}i}} \tag{2.11}$$

and the polaron radii are defined via

$$\rho_{\mathrm{e}i} = \sqrt{\frac{\hbar}{2m_{\mathrm{e}}\omega_{\mathrm{LO}i}}}\,, \quad \rho_{\mathrm{h}i} = \sqrt{\frac{\hbar\gamma_1}{2m_0\omega_{\mathrm{LO}i}}}\,. \tag{2.12}$$

The two pertinent LO phonon branches and their corresponding energies $\hbar\omega_{\mathrm{LO}i}$ are indicated by the indices $i = 1, 2$.

In order to consider the momentum dependence of the dielectric constant for small exciton extensions, a contact potential [8, 24, 25]

$$V_d = -V_0 V_{\mathrm{uc}} \delta(\boldsymbol{r}) \tag{2.13}$$

is used. To address minor deviations between theoretical predictions and experimental observations, the value of V_0 is introduced as a fitting parameter. The volume of the unit cell is described by $V_{\mathrm{uc}} = a_{\mathrm{g}}^3$.

The electron and hole spin interact via [24]

$$\mathcal{H}_{\mathrm{exch}} = J_0 \left(\frac{1}{4} - \frac{1}{\hbar^2}\boldsymbol{S}_{\mathrm{e}} \cdot \boldsymbol{S}_{\mathrm{h}}\right) V_{\mathrm{uc}} \delta(\boldsymbol{r}) = J_0 \left(1 - \frac{1}{2\hbar^2}\boldsymbol{S}^2\right) V_{\mathrm{uc}} \delta(\boldsymbol{r})\,, \tag{2.14}$$

where $\boldsymbol{S} = \boldsymbol{S}_{\mathrm{e}} + \boldsymbol{S}_{\mathrm{h}}$ is the total spin. Depending on how closely the spins are aligned, it causes a splitting of states with S admixture [8].

Regarding all above mentioned corrections, the CCC are given by

$$V_{\mathrm{CCC}} = V^{\mathrm{H}} + V_d + \mathcal{H}_{\mathrm{exch}}\,. \tag{2.15}$$

2.2.4 Considering external electric and magnetic fields

External fields need to be applied to observe exceptional points, which will be explained in Section 2.5. Additionally, these fields reduce the symmetry of the system [8]. When an external magnetic field $\boldsymbol{B}$ is applied, the minimum coupling $\boldsymbol{p}_{\mathrm{e}} \to \boldsymbol{p}_{\mathrm{e}} + e\boldsymbol{A}(\boldsymbol{r}_{\mathrm{e}})$ and $\boldsymbol{p}_{\mathrm{h}} \to \boldsymbol{p}_{\mathrm{h}} - e\boldsymbol{A}(\boldsymbol{r}_{\mathrm{h}})$ has to be introduced. Here,

$$\boldsymbol{A}\left(\boldsymbol{r}_{\mathrm{e/h}}\right) = \frac{1}{2}\left(\boldsymbol{B} \times \boldsymbol{r}_{\mathrm{e/h}}\right) \tag{2.16}$$

is a vector potential for a homogeneous magnetic field. The Hamiltonian can be rewritten

Table 2.1: Material parameters of Cu_2O used in this thesis.

Gap energy	$E_g = 2.172\,08\,\text{eV}$	[4]
Electron mass	$m_e = 0.99\,m_0$	[26]
Hole mass	$m_h = 0.58\,m_0$	[26]
Spin-orbit coupling	$\Delta = 0.131\,\text{eV}$	[16]
Valence band parameters	$\gamma_1 = 1.76$	[16]
	$\gamma_2 = 0.7532$	[16]
	$\gamma_3 = -0.3668$	[16]
	$p_1 = -0.020$	[16]
	$p_2 = -0.0037$	[16]
	$p_3 = -0.0337$	[16]
Fourth Luttinger parameter	$\kappa = -0.5$	[11]
Dielectric constants	$\varepsilon_{s1} = 7.5$	[27]
	$\varepsilon_{b1} = \varepsilon_{s2} = 7.11$	[27]
	$\varepsilon_{b2} = 6.46$	[27]
Exchange interaction	$J_0 = 0.792\,\text{eV}$	[24]
Short distance correction	$V_0 = 0.539\,\text{eV}$	[24]
Lattice constant	$a_g = 0.426\,96\,\text{nm}$	[28]
Energy of Γ_4^--LO phonons	$\hbar\omega_{LO1} = 18.7\,\text{meV}$	[25]
	$\hbar\omega_{LO2} = 87\,\text{meV}$	[25]
Landé factor of the electron	$g_c = 2.1$	[29]

in the form

$$\mathcal{H}_B = \mathcal{H}(B=0) + eB\mathcal{H}_1 + (eB)^2\,\mathcal{H}_2 \tag{2.17}$$

for a field with magnitude B. In [11] the terms for $\mathcal{H}_1$ and $\mathcal{H}_2$ can be found for three different configurations of the magnetic field along the axes [001], [110] and [111].

Not only the minimal coupling but also the interaction between the magnetic field and the spins needs to be considered via the Hamiltonian [11]

$$\mathcal{H}_B = \mu_B \left[g_c \boldsymbol{S}_e + \left(3\kappa + \frac{g_s}{2}\right) \boldsymbol{I} - g_s \boldsymbol{S}_h \right] \cdot \frac{\boldsymbol{B}}{\hbar}\,, \tag{2.18}$$

where μ_B is the Bohr magneton, κ the fourth Luttinger parameter and g_c and $g_s \approx 2$ the Landé factors of electron and hole, respectively.

Applying an external electric field $\boldsymbol{f}$ leads to the Hamiltonian

$$\mathcal{H}_f(\boldsymbol{r}_e - \boldsymbol{r}_h) = -e\,(\boldsymbol{r}_e - \boldsymbol{r}_h) \cdot \boldsymbol{f}\,, \tag{2.19}$$

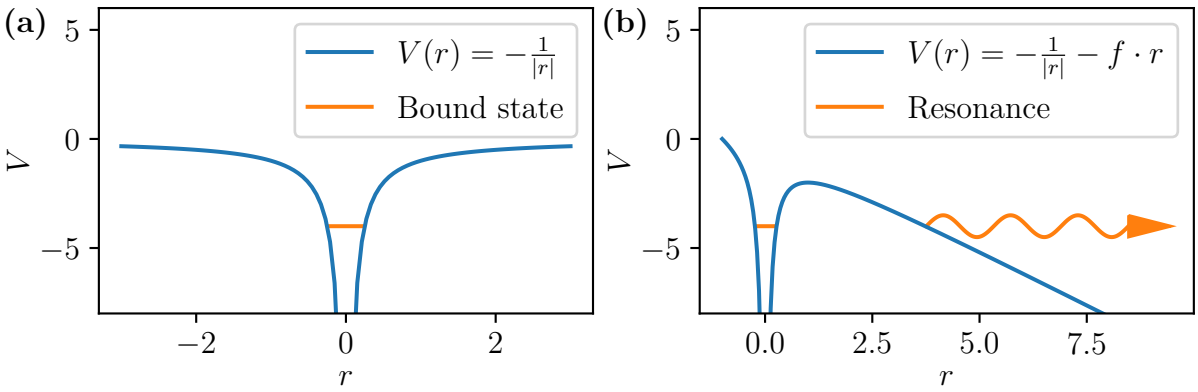

Figure 2.2: **(a)** A Coulomb potential can have bound states with infinite lifetime. **(b)** Applying an external electric field f results in a Coulomb-Stark potential. The previously bound state can now tunnel through the potential barrier and thus has a finite lifetime. This is called resonance or quasi-bound state.

which is just added to Equation (2.4) to describe the system. This results in the Hamiltonian

$$\mathcal{H} = E_\mathrm{g} + \mathcal{H}_\mathrm{e}(\boldsymbol{p}_\mathrm{e}) + \mathcal{H}_\mathrm{h}(\boldsymbol{p}_\mathrm{h}) + V(\boldsymbol{r}_\mathrm{e} - \boldsymbol{r}_\mathrm{h}) + V_\mathrm{CCC}(\boldsymbol{r}) + \mathcal{H}_B + \mathcal{H}_f\,. \tag{2.20}$$

All material parameters of Cu_2O introduced in this section are listed in Table 2.1.

2.3 Resonances

Both bound and quasi-bound states can occur in quantum systems. The latter are also called resonances, which have a certain lifetime and enough energy to decay into two or more subsystems [9, 30, 31]. An example of such a quasi-bound state is a radioactive atomic nucleus, which decays into a new atomic nucleus by emitting a radiation particle. Figure 2.2 shows how resonances can arise in the case of excitons. The bound state in the Coulomb potential (cf. Figure 2.2a) becomes a resonance when an external electric field is applied (cf. Figure 2.2b). The Coulomb-Stark potential

$$V_\mathrm{CS}(\boldsymbol{r}) = -\frac{e^2}{4\pi\varepsilon_0\varepsilon\,|\boldsymbol{r}|} + \boldsymbol{f}\cdot\boldsymbol{r} \tag{2.21}$$

describes the entire interaction. Here $\boldsymbol{f}$ is the electric field. The field lowers the potential barrier, allowing the previously bound state with infinite lifetime to tunnel through this barrier, leading to a finite lifetime [9].

2.3.1 Complex eigenvalues

The time evolution of resonances can be expressed by the wave function [1, 32]

$$\psi(t) = \mathrm{e}^{-\mathrm{i}\frac{\tilde{E}t}{\hbar}}\psi(0) \tag{2.22}$$

with the complex energy eigenvalue

$$\tilde{E} = E - \mathrm{i}\frac{\Gamma}{2}, \tag{2.23}$$

which represents its finite lifetime. The real part $\mathrm{Re}\left(\tilde{E}\right) = E$ describes the energy, whereas the imaginary part $\mathrm{Im}\left(\tilde{E}\right) = -\frac{\Gamma}{2}$ leads to an exponential decay and hence defines the width. Due to the fact that the eigenvalues of a Hermitian Hamiltonian are always real, the Hamiltonian has to be non-Hermitian [9]. To uncover complex energies, the complex-coordinate-rotation method described below can be utilized as one possible technique.

2.3.2 Complex-coordinate-rotation

The introduction of complex scaling can be achieved through the application of a unitary operator $U(\theta)$ on both the wave functions and Hamiltonian of the considered system [32],

$$\left(U(\theta)\mathcal{H}U^{-1}(\theta)\right)\left(U(\theta)\psi_n\right) = E_n\left(U(\theta)\psi_n\right) . \tag{2.24}$$

Various forms of similarity transformations have been employed to derive the Schrödinger equations with complex rotation (cf. [31]). The fundamental idea is to apply complex rotation or scaling

$$\boldsymbol{r} \to \mathrm{e}^{\mathrm{i}\theta}\boldsymbol{r} \tag{2.25}$$

to every instance of the relative coordinate $\boldsymbol{r}$ in both the wave function and the Hamiltonian. For the purpose of the current discussion, attention can be centered on an operator that acts on both the wave function

$$U(\theta)\psi(\boldsymbol{r}) = \mathrm{e}^{\mathrm{i}\frac{3\theta}{2}}\psi(\boldsymbol{r}\mathrm{e}^{\mathrm{i}\theta}) \tag{2.26}$$

and the Hamilton operator

$$\bar{\mathcal{H}}(\theta) = \left(U(\theta)\mathcal{H}U^{-1}(\theta)\right) = -\frac{1}{2}\mathrm{e}^{-2\mathrm{i}\theta}\Delta + V(\boldsymbol{r}\mathrm{e}^{\mathrm{i}\theta}) \tag{2.27}$$

as depicted. When discussing expectation values, it is convenient to define the action of the operator on the wave function with a phase to account for the transformation of the integration measure. For simplicity, Equations (2.26) and (2.27) are given for a Hamiltonian that considers two bodies. To extend this approach to an N-body system, the complex-coordinate-rotation method is applied to all independent center-of-mass coordinates $\boldsymbol{r}_i$ [32].

The representation of complex rotation in Equations (2.26) and (2.27) offers a significant advantage due to its close association with the integration variable during the calculation of energy expectation values. This advantage becomes particularly relevant when considering a normalized wave function that is both radially symmetric and the solution to the Hamilton operator

$$\mathcal{H}(r) = -\frac{1}{2}\frac{1}{r^2}\frac{\mathrm{d}}{\mathrm{d}r}r^2\frac{\mathrm{d}}{\mathrm{d}r} + V(r) \tag{2.28}$$

featuring a radially symmetric potential $V(r)$. In this case, the energy expectation value adopts the form

$$\langle E\rangle = \int_0^\infty R(r)\left(-\frac{1}{2}\frac{1}{r^2}\frac{\mathrm{d}}{\mathrm{d}r}r^2\frac{\mathrm{d}}{\mathrm{d}r} + V(r)\right)R(r)r^2\,\mathrm{d}r\ . \tag{2.29}$$

Inserting the Equations (2.26) and (2.27) results in

$$\begin{aligned}\langle E\rangle &= \int_0^\infty \mathrm{e}^{\mathrm{i}\frac{3\theta}{2}}R(\mathrm{e}^{\mathrm{i}\theta}r)\left(-\frac{\mathrm{e}^{-\mathrm{i}2\theta}}{2}\frac{1}{r}\frac{\mathrm{d}}{\mathrm{d}r}r^2\frac{\mathrm{d}}{\mathrm{d}r} + V(\mathrm{e}^{\mathrm{i}\theta}r)\right)\mathrm{e}^{\mathrm{i}\frac{3\theta}{2}}R(\mathrm{e}^{\mathrm{i}\theta}r)r^2\,\mathrm{d}r \\ &= \int_0^\infty R(\mathrm{e}^{\mathrm{i}\theta}r)\left(-\frac{1}{2}\frac{1}{(\mathrm{e}^{\mathrm{i}\theta}r)^2}\frac{\mathrm{d}}{\mathrm{d}(\mathrm{e}^{\mathrm{i}\theta}r)}(\mathrm{e}^{\mathrm{i}\theta}r)^2\frac{\mathrm{d}}{\mathrm{d}(\mathrm{e}^{\mathrm{i}\theta}r)} + V(\mathrm{e}^{\mathrm{i}\theta}r)\right)R(\mathrm{e}^{\mathrm{i}\theta}r)(\mathrm{e}^{\mathrm{i}\theta}r)^2\,\mathrm{d}(\mathrm{e}^{\mathrm{i}\theta}r)\ ,\end{aligned} \tag{2.30}$$

which is equivalent to integrating the variable $\rho = \mathrm{e}^{\mathrm{i}\theta}r$ along the complex contour $C = \{\rho = \mathrm{e}^{\mathrm{i}\theta}r\,|\,0 \le r < \infty\}$

$$\langle E\rangle = \int_C R(\rho)\left(-\frac{1}{2}\frac{1}{\rho}\frac{\mathrm{d}}{\mathrm{d}\rho}\rho^2\frac{\mathrm{d}}{\mathrm{d}\rho} + V(\rho)\right)R(\rho)\rho^2\,\mathrm{d}\rho\ . \tag{2.31}$$

Therefore, calculating the integral along a different contour in complex coordinate space has the same impact on the energy expectation value as using the method described in Equations (2.26) and (2.27). Two possible contours are shown in Figure 2.3. If a function is holomorphic between two contours that connect the same points in the

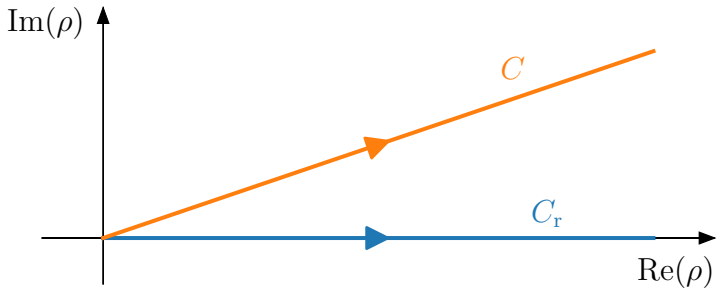

Figure 2.3: Two possible contours to evaluate the integral in Equation (2.31). The calculation of the energy expectation value for a bound state according to Equation (2.29) is equivalent to the path along the real axis C_r. For scaled wave functions and a complex rotated Hamiltonian as in Equation (2.30), the evaluation of the expectation value corresponds to the contour C. Adapted from [32].

complex plane, Cauchy's theorem states that the line integral will yield the same values for both contours. For $r \to \infty$ the bound state wave functions vanish, which is why the two contours C and C_r can be connected at infinite distance from the origin. This connection does not contribute to the line integral and thus has no effect on the result.

Based on the formulation of the contour integral (2.31), it is obvious that the complex rotation does not influence the energies of the bound states [1]. However, it does affect the energy spectrum of the quasi-bound states. The complex-coordinate-rotation causes the rotation of the continuum into the bottom half of the complex plane by an angle of 2θ, which can be very easily exemplified by short-range interaction potentials [1, 31]. The solution of a radial scattering problem is given by

$$\psi_\mathrm{scatt} = A(k)\frac{\mathrm{e}^{\mathrm{i}kr}}{r} + B(k)\frac{\mathrm{e}^{-\mathrm{i}kr}}{r}\,. \tag{2.32}$$

The energy ($m = \hbar = 1$) is

$$E = \frac{k^2}{2} \tag{2.33}$$

for $r \to \infty$. Applying the complex rotation on the wave function (2.32) leads to non-physical behavior due to the divergence of one of the exponential functions. This can be avoided by introducing $k \to k\mathrm{e}^{-\mathrm{i}\theta}$ [9, 31], which changes the energy to

$$\bar{E} = \frac{k^2\mathrm{e}^{-2\mathrm{i}\theta}}{2}\,. \tag{2.34}$$

This is the rotation of the continuum above mentioned by the angle 2θ into the bottom half of the complex plane [32]. Due to this rotation, resonances are exposed as illustrated

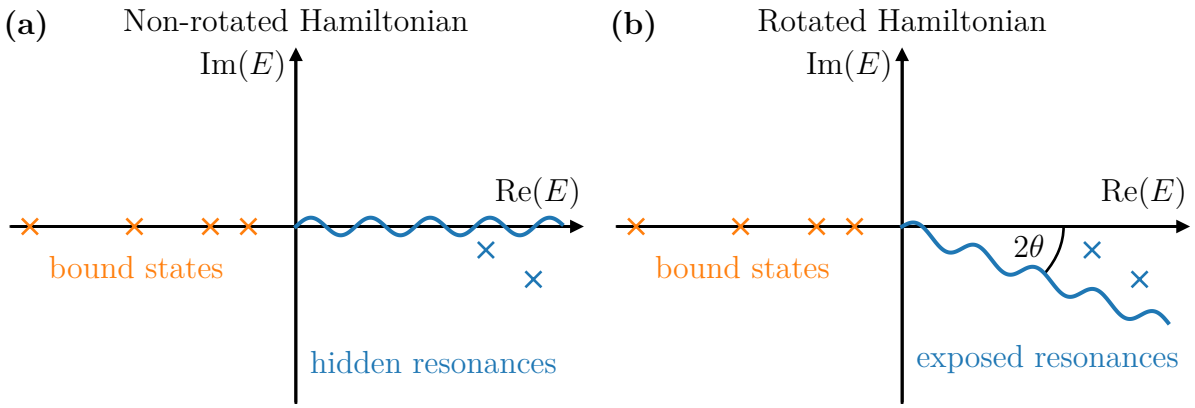

Figure 2.4: The effect of the complex-coordinate-rotation is depicted here. **(a)** For the non-rotated Hamiltonian no resonances are visible. All solutions lie on the real axis. **(b)** After the rotation the bound states are still located on the real axis but the continuum is rotated into the bottom half of the complex plane by the angle 2θ. Resonances with discrete complex energy eigenvalues which do not depend on the angle θ are exposed. Adapted from [32].

in Figure 2.4 which do not depend on the angle θ. The inverted harmonic oscillator, which can be represented as

$$\mathcal{H} = -\frac{1}{2}\frac{\mathrm{d}^2}{\mathrm{d}x^2} - \frac{1}{2}x^2\,, \tag{2.35}$$

visualizes this effect [31]. The solutions of the Schrödinger equation are exclusively unbound states [9]. Applying the complex rotation yields the Hamiltonian

$$\bar{\mathcal{H}} = -\frac{1}{2}\mathrm{e}^{-2\mathrm{i}\theta}\frac{\mathrm{d}^2}{\mathrm{d}x^2} - \mathrm{e}^{2\mathrm{i}\theta}\frac{1}{2}x^2\,. \tag{2.36}$$

The complex rotated and, for an appropriate chosen angle θ, square integrable wave functions

$$\psi_n\left(\mathrm{e}^{\mathrm{i}\theta}x\right) = cH_n\left(\frac{\mathrm{e}^{\mathrm{i}\theta}x}{\sqrt{\mathrm{i}}}\right)\exp\left(\mathrm{i}\frac{\mathrm{e}^{\mathrm{i}2\theta}x^2}{2}\right) \tag{2.37}$$

solve Equation (2.36). Here, c is a normalization constant and $H_n(x)$ are the Hermite polynomials. The corresponding energy eigenvalues

$$\bar{E}_n = -\mathrm{i}\left(n + \frac{1}{2}\right)\,, \quad n = 0, 1, 2, ... \tag{2.38}$$

are purely imaginary. By comparing Equations (2.23) and (2.38) it is evident that the inverted harmonic oscillator has an infinite number of resonances with the width $\Gamma = 2n + 1$ at the position $E = 0$.

The results of the complex-coordinate-rotation can be summarized as follows:

- The complex rotation has no effect on the bound states (cf. Figure 2.4).
- The continuum is rotated by the angle 2θ into the bottom half of the complex plane (cf. Figure 2.4b).
- Previously hidden resonances (cf. Figure 2.4a) are exposed (cf. Figure 2.4b). Their discrete energy eigenvalues are independent of the angle θ and have the form $\tilde{E} = E - \mathrm{i}\frac{\Gamma}{2}$ with position E and width Γ.

2.4 Numerical method to diagonalize the exciton Hamiltonian of Cu_2O

After introducing all relevant parameters, an explanation is provided on the method employed to acquire the eigenvalues of the exciton Hamiltonian. The stationary Schrödinger equation is expressed in terms of a complete basis in order to numerically determine the eigenvalues and eigenstates [8, 9]. The orbital angular part is described using the spherical harmonics with the quantum numbers L and M. To handle the electron and hole spins $\boldsymbol{S}_\mathrm{e}$ and $\boldsymbol{S}_\mathrm{h}$ as well as the quasi-spin $\boldsymbol{I}$, additional quantum numbers are required. From the already introduced effective hole spin $\boldsymbol{J} = \boldsymbol{I} + \boldsymbol{S}_\mathrm{h}$, which is the coupling of quasi- spin and hole spin, the angular momentum $\boldsymbol{F} = \boldsymbol{J} + \boldsymbol{L}$ can be obtained by adding the orbital angular momentum $\boldsymbol{L}$. Additionally, regarding the electron spin $\boldsymbol{S}_\mathrm{e}$ yields the total angular momentum $\boldsymbol{F}_\mathrm{t} = \boldsymbol{F} + \boldsymbol{S}_\mathrm{e}$ as well as its z-component M_{F_t}. The Coulomb-Sturmian functions [12, 33, 34]

$$U_{N,L} = N_{N,L,\alpha} \left(\frac{2r}{\alpha}\right)^L \mathrm{e}^{-\frac{r}{\alpha}} L_N^{2L+1}\left(\frac{2r}{\alpha}\right), \tag{2.39}$$

with a normalization factor $N_{N,L,\alpha}$ and the Laguerre polynomials $L_n^m(x)$, are used to calculate the radial part. Instead of the principal quantum number (n), the index $N = n - L - 1$ denotes the radial quantum number. The parameter α is a convergence parameter and can in principle be chosen arbitrarily. By setting it to

$$\alpha = |\alpha|\mathrm{e}^{\mathrm{i}\theta} \tag{2.40}$$

and thus considering the complex rotation angle θ from Equation (2.25) as well as $|\alpha|$, the latter only affecting the convergence, it is possible to implement the complex-coordinate-

rotation. Hence, resonances can be calculated. The set of used quantum numbers are abbreviated by $\mathit{\Pi} = \left\{N, L; (I, S_\mathrm{h}), J; F, S_\mathrm{e}; F_t, M_{F_t}\right\}$, which is why the basis states can be expressed via

$$|\mathit{\Pi}\rangle = \left|N, L; (I, S_\mathrm{h}), J; F, S_\mathrm{e}; F_t, M_{F_t}\right\rangle . \tag{2.41}$$

Although not being orthogonal regarding the standard scalar product, this basis has the benefit of being complete despite the absence of the hydrogen continuum.

Spherical tensor notation is used to represent the Hamiltonian [11, 12]. The [001] direction serves as the symmetry axis for aligning the magnetic and electric fields. To ensure consistency between the orientation of the fields and the quantization axis, the coordinates of the Hamiltonian are rotated accordingly. To calculate the exciton wave function $|\Psi\rangle$, the ansatz

$$|\Psi\rangle = \sum_{\mathit{\Pi}} c_{\mathit{\Pi}} |\mathit{\Pi}\rangle \tag{2.42}$$

is used. This leads to a generalized eigenvalue problem for the Schrödinger equation

$$\boldsymbol{H}\boldsymbol{c} = E\boldsymbol{M}\boldsymbol{c}\,, \tag{2.43}$$

where $\boldsymbol{H}$ is the Hamiltonian matrix and $\boldsymbol{M}$ the overlap matrix. Cut-offs to the quantum numbers $N + L + 1 \leq n_\mathrm{max}$ and $F \leq F_\mathrm{max}$ are incorporated in order to obtain finite matrices and vectors. It is crucial for achieving accurate and well-converged results to select these parameters, along with $|\alpha|$ and rotation angle θ, properly. If variations in these parameters do not cause significant alterations in the calculated spectra, convergence is considered satisfactory. The eigenvalues E and the eigenvectors $\boldsymbol{c}$ containing the coefficients of Equation (2.42) are obtained by using a suitable ARPACK routine [35]. When incorporating the two delta terms of the CCC into the Hamiltonian, a two-step approach is followed. Firstly, the Hamiltonian is diagonalized without considering the delta terms. In this step, the eigenstates and eigenvalues are obtained. Subsequently, a second eigenvalue problem is established, incorporating the delta terms, but utilizing only the converged eigenstates obtained from the initial diagonalization step. This approach allows for an effective treatment of the delta terms while building upon the accurate solutions obtained in the first diagonalization.

2.5 Exceptional points

In eigenvalue problems which depend on a parameter, EPs can occur [9, 32, 36–38]. Varying this usually complex parameter can lead to branch points where the eigenvalues as well as the eigenvectors coalesce. As an illustration, consider the case where the linear map

$$\boldsymbol{y} = \boldsymbol{T}(\kappa)\boldsymbol{x}\,, \tag{2.44}$$

which is represented by the matrix $T(\kappa)$, depends holomorphically on the scalar complex parameter κ in the domain D_0 of the complex plane, where $\boldsymbol{x}, \boldsymbol{y} \in \mathbb{R}^n$. The eigenvalues can be calculated by

$$\det(\boldsymbol{T}(\kappa) - \lambda\mathbb{1}) = 0\,. \tag{2.45}$$

This algebraic equation is of degree n. The eigenvalues λ in the domain D_0 are themselves branches of analytic functions or analytic functions of κ, which only have algebraic singularities [39].

When an analytic function has at least two eigenvalues that are shared by at least two of the function's branches, i.e. which are on two different Riemann sheets [2], EPs can be found. They are branch point singularities of the analytic function and occur at isolated points in the two-dimensional parameter space of κ. At these points, the eigenvalues and the eigenvectors coincide, i.e. degenerate, which results in less distinct eigenvalues and eigenvectors. The amount of eigenvalues does not depend on κ at any other locations in the domain D_0 [36].

The presence of branch point singularities within the structure of EPs carries significant implications for the corresponding eigenvectors and eigenvalues.

- By traversing a closed curve in the parameter space surrounding the EP (excluding the branch point $\kappa = \kappa_{\mathrm{EP}}$), a permutation of the eigenvalues can be detected [36]. Discretizing the closed curve by k points and solving Equation (2.45) for each point on this curve results in groups of eigenvalues [32]

$$\left\{\lambda_{1,1}(\kappa), \dots, \lambda_{1,k}(\kappa)\right\}, \quad \left\{\lambda_{2,1}(\kappa), \dots, \lambda_{2,k}(\kappa)\right\}. \tag{2.46}$$

  The most common scenario observed in physical systems involves a square root branch point singularity, also known as EP2, in which two eigenvalues exhibit permutation while any further eigenvalues of the system do not. Thus, each group of eigenvalues belonging to the EP does not form a closed loop. Upon encircling the EP, where $\kappa = \kappa_{\mathrm{EP}}$, the two eigenvalues representing the two branches of an

analytic function are exchanged. Starting at an arbitrary value of κ_0, crossing the border between both Riemann sheets occurs precisely once during a single turn around κ_{EP}, and the continuation of $\lambda_1(\kappa_0)$ ends at the starting point of $\lambda_2(\kappa_0)$.

- With the exception of the EPs $\kappa \neq \kappa_{\mathrm{EP}}$, the eigenvalues corresponding to these points are distinct, and each of them is associated with a unique eigenvector. Analogous to the eigenvalues, they also pass through a branch point singularity at the EP and thus degenerate [36]. In contrast to the "normal" degeneracy not only the eigenvalues but also the eigenvectors degenerate and there is only one linearly independent eigenvector at the EP. So it is rather a coalescence than a degeneracy [40]. The dimension of the eigenvector space is reduced at the EP compared to the rest of the parameter space [32], which is why the matrix can not be diagonalized [38].

- In the most common physical systems an EP2 occurs, which has to be encircled four times to obtain the initial state due to Berry's phase. After two circulations the eigenvalues return to their original position but the eigenvectors pick up a phase of the form [40]

$$\boldsymbol{v}_1 \overset{2\text{ circles}}{\rightarrow} -\boldsymbol{v}_1 \quad \text{and} \quad \boldsymbol{v}_2 \overset{2\text{ circles}}{\rightarrow} -\boldsymbol{v}_2\,. \tag{2.47}$$

  This indicates the presence of an algebraic singularity which exhibits the behavior of a fourth root at the EP.

EPs can appear in classical and quantum mechanical problems as well as in optics and other fields [38]. For a Poiseuille flow the instabilities and particular behavior of the Reynolds number is related to EPs. In Bose-Einstein condensates, an EP denotes the transition point at which individual atoms begin to form clusters or molecules.

2.5.1 Simple example

In order to visualize an EP and its behavior, a linear non-Hermitian map represented by the two-dimensional matrix [32, 36]

$$\boldsymbol{M}(\kappa) = \begin{pmatrix} 1 & \kappa \\ \kappa & -1 \end{pmatrix} \tag{2.48}$$

can be used as a simple example with $\kappa \in \mathbb{C}$. Despite being a straightforward illustration, all significant aspects of EPs can be demonstrated since the close vicinity of an EP in an

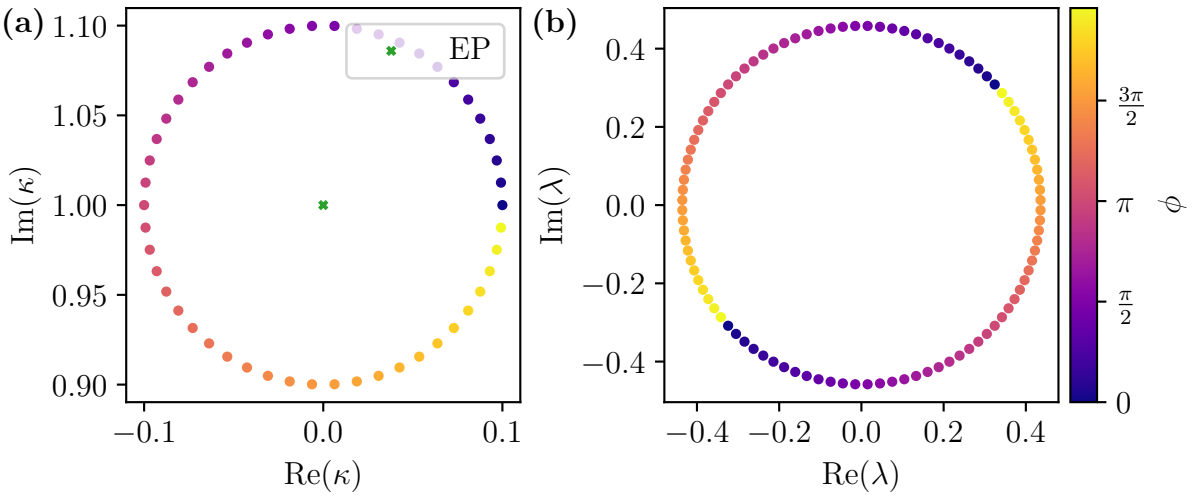

Figure 2.5: **(a)** The exceptional point (EP) $\kappa_+ = \mathrm{i}$ of the simple example (2.48) is encircled in the parameter space κ. Each point in the complex plane is described by the angle ϕ in Euler form as depicted in Equation (2.52). **(b)** This leads to an exchange of the positions of the two eigenvalues in the complex energy plane. The eigenvalues calculated for each point on the circle are marked by the respective color of the color bar indicating the angle ϕ, in order to illustrate the path of each eigenvalue and the associated permutation.

n-dimensional system can be expressed by a two-dimensional problem [2]. Calculating the eigenvalues of Equation (2.48) results in

$$\lambda_1 = \sqrt{1+\kappa^2} \quad \text{and} \quad \lambda_2 = -\sqrt{1+\kappa^2}\,. \tag{2.49}$$

It is evident that the eigenvalues are two branches of the same analytic function in κ. They coalesce at $\kappa_\pm = \pm\mathrm{i}$, which means that there exist two EPs in this system. The corresponding eigenvectors are

$$\boldsymbol{v}_1(\kappa) = \begin{pmatrix} -\kappa \\ 1-\sqrt{1+\kappa^2} \end{pmatrix} \quad \text{and} \quad \boldsymbol{v}_2(\kappa) = \begin{pmatrix} -\kappa \\ 1+\sqrt{1+\kappa^2} \end{pmatrix} \tag{2.50}$$

from which it is obvious that these also coalesce at $\kappa_\pm = \pm\mathrm{i}$ and that there is therefore only one linearly independent eigenvector

$$\boldsymbol{v}(\pm\mathrm{i}) = \begin{pmatrix} \mp\mathrm{i} \\ 1 \end{pmatrix}. \tag{2.51}$$

The exchange behavior of the two eigenvalues when encircling the EP can be visualized by

$$\kappa(\phi) = \mathrm{i} + \varrho \mathrm{e}^{\mathrm{i}\phi} \,, \tag{2.52}$$

which describes a circle with radius ϱ around the EP $\kappa_+ = \mathrm{i}$. This orbit is shown in Figure 2.5a, where the color bar denotes the angle ϕ. The permutation of the eigenvalues in the complex energy plane can be seen in Figure 2.5b. After one closed loop in the parameter space the eigenvalues exchange their positions. The path of each eigenvalue is depicted by the colors of the color bar. Due to the simplicity of this example, this permutation can also be shown analytically by substituting the circular parametrization (2.52) into the eigenvalues from Equation (2.49)

$$\lambda_{1,2} = \pm\sqrt{1 + \left(\mathrm{i} + \varrho \mathrm{e}^{\mathrm{i}\phi}\right)^2} = \pm\sqrt{\varrho}\mathrm{e}^{\mathrm{i}\frac{\phi}{2}}\sqrt{2\mathrm{i} + \varrho \mathrm{e}^{\mathrm{i}\phi}} \overset{\varrho \ll 2}{\approx} \pm\sqrt{2\varrho}\mathrm{e}^{\mathrm{i}\frac{\pi}{4}}\mathrm{e}^{\mathrm{i}\frac{\phi}{2}} \,, \tag{2.53}$$

which leads to

$$\lambda_1 = \sqrt{2\varrho}\mathrm{e}^{\mathrm{i}\left(\frac{\pi}{4}+\frac{\phi}{2}\right)} \quad \text{and} \quad \lambda_2 = \sqrt{2\varrho}\mathrm{e}^{\mathrm{i}\left(\frac{5\pi}{4}+\frac{\phi}{2}\right)} \,. \tag{2.54}$$

After one closed loop in the parameter plane, i.e. $\phi = 2\pi$, λ_1 changes to λ_2 and vice versa, which is exactly the behavior shown in Figure 2.5.

Due to the small radius both paths of the eigenvalues in the complex energy plane build a half circle. For larger radii or elliptical orbits this shape can be much more complex.

2.5.2 Methods to find EPs

Methods for the localization of EPs include the three-point method and the octagon method. These are briefly explained hereafter. Only the eigenvalues associated with the EP are considered and the analytical functions

$$p \equiv (\lambda_1 - \lambda_2)^2 \,, \tag{2.55}$$

$$s \equiv \frac{1}{2}(\lambda_1 + \lambda_2) \,, \tag{2.56}$$

are introduced. To ensure analyticity, the eigenvalue difference of the two-dimensional matrix is squared in the variable p, owing to its square root behavior. Due to the degeneracy of the eigenvalues, p is zero at the EP, so a root search is performed on p. Both methods mentioned above use a Taylor expansion to approximate p.

Three-point method

The three-point method was invented by Uzdin and Lefebvre [5]. It is an iterative algorithm to locate the EP in the parameter space, which is based on an arbitrarily chosen evolution point (γ_0, f_0) [9]. Here, the complex parameter κ is divided into two real valued parameters $\mathrm{Re}(\kappa) = \gamma$ and $\mathrm{Im}(\kappa) = f$. As already mentioned, the EP can be described by a two-dimensional matrix model [2]

$$\boldsymbol{M} = \begin{pmatrix} a_0 + a_\gamma(\gamma - \gamma_0) + a_f(f - f_0) & b_0 + b_\gamma(\gamma - \gamma_0) + b_f(f - f_0) \\ b_0 + b_\gamma(\gamma - \gamma_0) + b_f(f - f_0) & c_0 + c_\gamma(\gamma - \gamma_0) + c_f(f - f_0) \end{pmatrix}, \tag{2.57}$$

which is non-Hermitian and complex symmetric, similar to the example in Section 2.5.1. The linear evolutions in the two real parameters γ and f around the evolution point (γ_0, f_0) with complex coefficients are depicted by the entries of this matrix [37]. Coupling to other states is neglected because of this two dimensional approach, which only considers the two states belonging to the EP. The eigenvalues of the matrix λ_i can be expressed by

$$s \equiv \frac{1}{2}(\lambda_1 + \lambda_2) = \mathrm{tr}(\boldsymbol{M}) = A + B(\gamma - \gamma_0) + C(f - f_0)\,, \tag{2.58a}$$

$$\begin{aligned} p \equiv (\lambda_1 - \lambda_2)^2 = \mathrm{tr}^2(\boldsymbol{M}) - 4\det(\boldsymbol{M}) = D + E(\gamma - \gamma_0) + F(f - f_0) \\ + \mathcal{O}\Big((\gamma - \gamma_0)^2, (f - f_0)^2, (\gamma - \gamma_0)(f - f_0)\Big)\,, \end{aligned} \tag{2.58b}$$

where s and p are analytic functions depending on the parameters γ and f. For the new coefficients holds $A, B, C, D, E, F \in \mathbb{C}$. The evolution point is now set to values at the EP ($\gamma_0 = \gamma_{\mathrm{EP}}, f_0 = f_{\mathrm{EP}}$), which are still unknown, to determine them. The three-point method neglects all quadratic terms in Equation (2.58b). Due to the coalescence of the eigenvalues at the EP and thus $p = 0$, D can be set to $D = 0$, which results in

$$p = E(\gamma - \gamma_{\mathrm{EP}}) + F(f - f_{\mathrm{EP}})\,. \tag{2.59}$$

It is assumed that the close vicinity of the EP is sufficiently well described by the two coefficients E and F.

The eigenvalues $\lambda_{1,i}$ and $\lambda_{2,i}$ are calculated at three different points in the parameter space (γ_i, f_i) and inserted in Equation (2.59). Subtracting them leads to the linear set

of equations

$$p_2 - p_1 = E\,(\gamma_2 - \gamma_1) + F(f_2 - f_1)\;, \tag{2.60a}$$
$$p_3 - p_1 = E\,(\gamma_3 - \gamma_1) + F(f_3 - f_1)\;, \tag{2.60b}$$

which can be solved to obtain the complex coefficients E and F. Substituting these coefficients and one of the points (γ_i, f_i) in Equation (2.59) and dividing this equation into real and imaginary part, yields another linear set of equations

$$\begin{pmatrix} \mathrm{Re}(E) & \mathrm{Re}(F) \\ \mathrm{Im}(E) & \mathrm{Im}(F) \end{pmatrix} \begin{pmatrix} \gamma_{\mathrm{EP}} \\ f_{\mathrm{EP}} \end{pmatrix} = \begin{pmatrix} d_1 \\ d_2 \end{pmatrix}, \tag{2.61a}$$
$$d_1 = \mathrm{Re}(E)\gamma_1 + \mathrm{Re}(F)f_1 - \mathrm{Re}(p_1)\,, \tag{2.61b}$$
$$d_2 = \mathrm{Im}(E)\gamma_1 + \mathrm{Im}(F)f_1 - \mathrm{Im}(p_1)\,. \tag{2.61c}$$

Resolving Equation (2.61) results in an approximation for the EP in the parameter space $(\gamma_{\mathrm{EP}}, f_{\mathrm{EP}})$, around which three new points can be computed with smaller distance than the previous ones, thus creating an iterative process.

Since in higher-dimensional systems there are more than two eigenvalues, a complete orbit around the EP must be calculated to uniquely identify the two eigenvalues belonging to the EP, although only three of these calculated points are used for the method. In addition, a sufficient number of points on the orbit need to be computed to unambiguously verify the permutation of the eigenvalues. This means high computational cost, with much of the calculated data being useless. Another problem is the convergence of this method. Due to the linear approach of Equation (2.58b) the three-points already have to be close to the actual position of the EP. The method shows convergence for a relative radius of the parameters γ and f of about 0.03 % [37] for excitons in cuprous oxide in parallel magnetic (γ) and electric fields (f). So if the points are too far away the three-point method will not converge and other methods must be used to narrow the search region (cf. [9, 37]). This is why the octagon method was developed.

Octagon method

Unlike the three-point method, Equation (2.58b) is not linearly approximated in the octagon method [37], which leads to

$$\begin{aligned} p \equiv (\lambda_1 - \lambda_2)^2 = \mathrm{tr}^2(\boldsymbol{M}) - 4\det(\boldsymbol{M}) = D + E\,(\gamma - \gamma_0) + F(f - f_0) \\ + G\,(\gamma - \gamma_0)^2 + H\,(\gamma - \gamma_0)\,(f - f_0) + I\,(f - f_0)^2\;, \end{aligned} \tag{2.62}$$

with the additional complex coefficients $G, H, I \in \mathbb{C}$. To determine all coefficients from Equation (2.62), nine points are needed, eight of which lie on a regular octagon and the ninth is its center (more details are given in [37]). Instead of orbiting the EP, small octagons are calculated, preventing groups of eigenvalues belonging to different states from overlapping. The two sets of eigenvalues belonging to the EP can be found by comparing their energies to that of an avoided crossing of two states, which is also a good starting point for the center of the first octagon. Each prediction for the EP $(\gamma_{\mathrm{EP}}, f_{\mathrm{EP}})$ is used as the center for the next octagon. Because of the quadratic terms in Equation (2.62) there is not only one solution. All other possibly complex solutions have no physical meaning and only exist due to the mathematical structure of this method. To get the one giving an approximation of the EP the so called ε-method can be used which is described in [37]. Nonetheless, this method could lead to an infinite loop of the octagon method and hence no convergence.

As already mentioned above, one of the main disadvantages of the three-point method is the very small convergence radius due to the linear Taylor expansion. The octagon method has in fact a larger convergence radius than the three-point method, but is still quite computationally expensive. For each iteration step, at least nine points need to be calculated, but to ensure the convergence of the computed points, there are usually significantly more. As already mentioned above, the ε-method, needed to get the right physical solution, can result in non convergence of the octagon method, which is another problem of this method. For these reasons, a novel method will be developed in this thesis using machine learning, namely Gaussian process regression. The used data to train a GPR model is obtained by simulations. Hence, the error is only due to numerical inaccuracies, which can be neglected. In contrast to neural networks, it is possible to ensure that the trained GPR model passes exactly through the given training points, which is one of the main reasons for using GPR.

3 Gaussian Processes Used in Machine Learning

Gaussian processes (GPs) are a widely accepted and sophisticated approach used for performing Bayesian non-linear non-parametric regression and classification tasks [41]. They belong to the group of supervised machine learning algorithms [7, 42]. By incorporating prior knowledge of the function being searched using a kernel, it is possible not only to make predictions, but also to provide model uncertainty for that prediction. In physics, e.g., GPR can be used to fit a model to experimental or simulated data.

3.1 Mathematical basics

For a better understanding of GPR, first some mathematical basics are explained. In doing so, a closer look is taken at what a GP is and how it can be described. Prior and posterior distributions are introduced along with the concept of kernel functions and covariance matrices.

3.1.1 Multivariate normal distribution

For simplicity, a two-dimensional space is assumed denoted by x and y. Generating two vectors $\boldsymbol{y}_i$ with $i = 1, 2$ which contain random values sampled from a normal distribution, plotting them at x_1 and x_2 respectively and connecting each value in $\boldsymbol{y}_1$ with one in $\boldsymbol{y}_2$ yields a set of linear functions which in general can be used for regression tasks [43]. The bi-variate normal distribution is given by

$$\begin{bmatrix} \boldsymbol{y}_1 \\ \boldsymbol{y}_2 \end{bmatrix} \sim \mathcal{N}\left(\boldsymbol{\mu}, \boldsymbol{\Sigma}\right) = \mathcal{N}\left(\begin{bmatrix} \mu_1 \\ \mu_2 \end{bmatrix}, \begin{bmatrix} \sigma_{11} & \sigma_{12} \\ \sigma_{21} & \sigma_{22} \end{bmatrix} \right) , \tag{3.1}$$

with the mean vector $\boldsymbol{\mu}$ and the covariance matrix $\boldsymbol{\Sigma}$. This distribution characterizes the joint probability distribution $P(\boldsymbol{y}_1, \boldsymbol{y}_2)$. The covariance matrix $\boldsymbol{\Sigma}$ captures the correlations between $\boldsymbol{y}_1$ and $\boldsymbol{y}_2$ through its off-diagonal elements, σ_{12} and σ_{21}. By extending this concept to an infinite number of vectors $\boldsymbol{y}$ at different positions x and connecting values from adjacent vectors, a set of functions can be obtained. To achieve smoother functions, a suitable covariance function $k(x, x')$ can be employed to account for correlations among nearby values. This will be discussed in more detail below. Thus, an infinite-dimensional Gaussian can be used to produce a continuous function space.

3.1.2 Gaussian processes

A GP is defined as a set of random variables where the joint distribution of any finite subset follows a Gaussian distribution, therefore it describes a distribution over functions [7]. For a given function, $f(\boldsymbol{x})$, the mean $m(\boldsymbol{x})$ and covariance function $k(\boldsymbol{x}, \boldsymbol{x}')$ are defined as

$$m(\boldsymbol{x}) = \mathbb{E}[f(\boldsymbol{x})]\,, \tag{3.2}$$

$$k(\boldsymbol{x}, \boldsymbol{x}') = \mathbb{E}[(f(\boldsymbol{x}) - m(\boldsymbol{x}))(f(\boldsymbol{x}') - m(\boldsymbol{x}'))]\,, \tag{3.3}$$

which fully specify a GP via

$$f(\boldsymbol{x}) \sim \mathcal{GP}(m(\boldsymbol{x}), k(\boldsymbol{x}, \boldsymbol{x}'))\,. \tag{3.4}$$

The vector $\boldsymbol{x} \in X \subset \mathbb{R}^D$ can be D-dimensional and belongs to the input set X which contains all possible inputs. At a particular position $\boldsymbol{x}$ the function value $f(\boldsymbol{x})$ is expressed by the random variables.

3.1.3 Prior and posterior of a Gaussian process

A linear regression model

$$f(\boldsymbol{x}) = \boldsymbol{\phi}(\boldsymbol{x})^\top \boldsymbol{w} \tag{3.5}$$

can provide a straightforward instance of a GP. Specifying a prior over the parameters — usually a Gaussian $\boldsymbol{w} \sim \mathcal{GP}(0, \Sigma_p)$ with zero mean and covariance matrix Σ_p — is necessary to encapsulate assumptions regarding these parameters prior to inspecting the observed data. A GP prior distribution and some sample functions randomly selected from it are illustrated in Figure 3.1a. Inserting Equation (3.5) and the above assumption

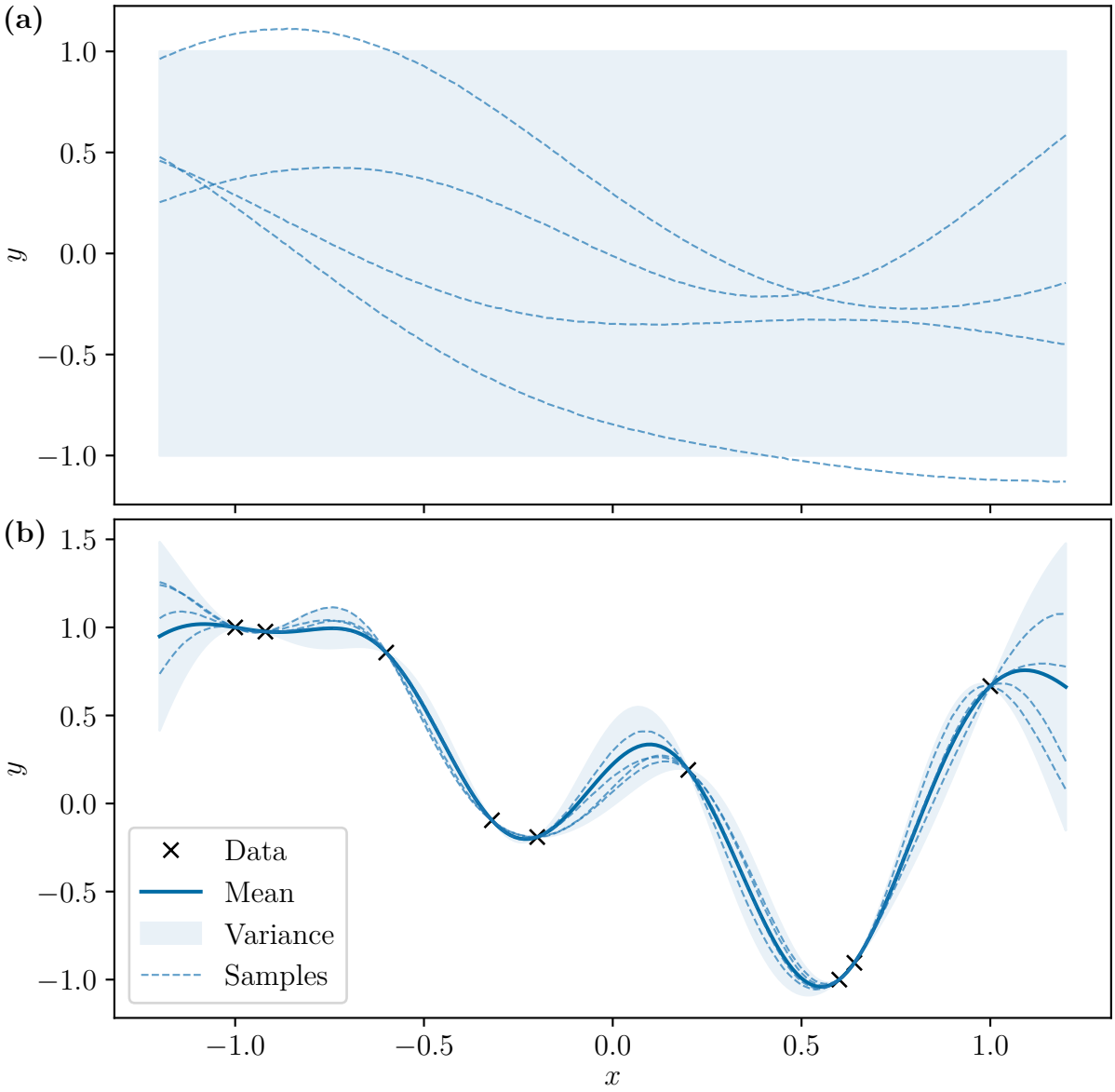

Figure 3.1: **(a)** A Gaussian process (GP) prior distribution is visualized, including four sample functions which are randomly chosen from this prior. Due to a large number of given input points, they are displayed as dashed lines rather than individual points, which would be more accurate. **(b)** The posterior distribution obtained after fitting the model to the observed, noise free, data points, marked as black crosses. Again, four sample functions randomly selected from the posterior are shown as dashed lines. Taking the mean of all possible functions that fit the given data points results in the solid blue line, which is used to make predictions. The shaded region in both plots marks the 95 % confidence interval calculated from the variance of the model. Adapted from [7].

about the weights $\boldsymbol{w}$ into Equations (3.2) and (3.3) results in

$$m(\boldsymbol{x}) = \boldsymbol{\phi}(\boldsymbol{x})^\top \mathbb{E}[\boldsymbol{w}] = 0\,, \tag{3.6}$$

$$k(\boldsymbol{x}, \boldsymbol{x}') = \boldsymbol{\phi}(\boldsymbol{x})^\top \mathbb{E}[\boldsymbol{w}\boldsymbol{w}^\top] \boldsymbol{\phi}(\boldsymbol{x}') = \boldsymbol{\phi}(\boldsymbol{x})^\top \Sigma_p \boldsymbol{\phi}(\boldsymbol{x}') \tag{3.7}$$

for the mean and covariance function, respectively.

It is essential to make a clear distinction between the prior and the posterior distributions. The posterior distribution over the weights $\boldsymbol{w}$ is used to make predictions as depicted in Figure 3.1b. It contains all known information, i.e. it is obtained after fitting the model to the observed data points.

3.1.4 Covariance and kernel function

The covariance function, also referred to as kernel function or simply kernel, determines the level of correlation between two random variables [7]. A popular kernel is the radial basis function (RBF) also known as squared exponential (SE), which is given by

$$\operatorname{cov}\big(f(\boldsymbol{x}_p), f(\boldsymbol{x}_q)\big) = k(\boldsymbol{x}_p, \boldsymbol{x}_q) = \mathrm{e}^{-\frac{1}{2}|\boldsymbol{x}_p - \boldsymbol{x}_q|^2} \tag{3.8}$$

and thus only depends on the distance between the inputs $\boldsymbol{x}_p$ and $\boldsymbol{x}_q$.

Mercer's theorem [7, 44, 45] states that any positive definite kernel function can be represented using a possibly infinite number of basis functions, e.g. the linear combination of an infinite number of basis functions with Gaussian shapes results in the RBF covariance function. Hence, defining the kernel function corresponds to a distribution over possible functions. Some sample functions distributed around a zero mean are shown in Figure 3.1a.

The kernel has to be selected according to the problem, since the smoothness of the basis functions, and thus that of the model, depends on it. For instance the RBF is infinitely mean-square differentiable and thus has smooth basis functions (cf. Figure 3.1). To achieve better results, the kernel usually contains free positive parameters that can be varied, so called hyperparameters Θ. These are the function variance σ_f^2 and the characteristic length-scale l. If, for example, experimental data with noise is used for training, there is an additional hyperparameter, the noise variance σ_n^2. An alternative to the RBF kernel function is the Matérn class of kernels

$$k_{\text{Matérn}}(r) = \sigma_f^2 \frac{2^{1-\nu}}{\Gamma(\nu)} \left(\sqrt{2\nu} r\right)^\nu K_\nu \left(\sqrt{2\nu} r\right) \quad \text{with} \quad r = \frac{|\boldsymbol{x}_p - \boldsymbol{x}_q|}{l}\,, \tag{3.9}$$

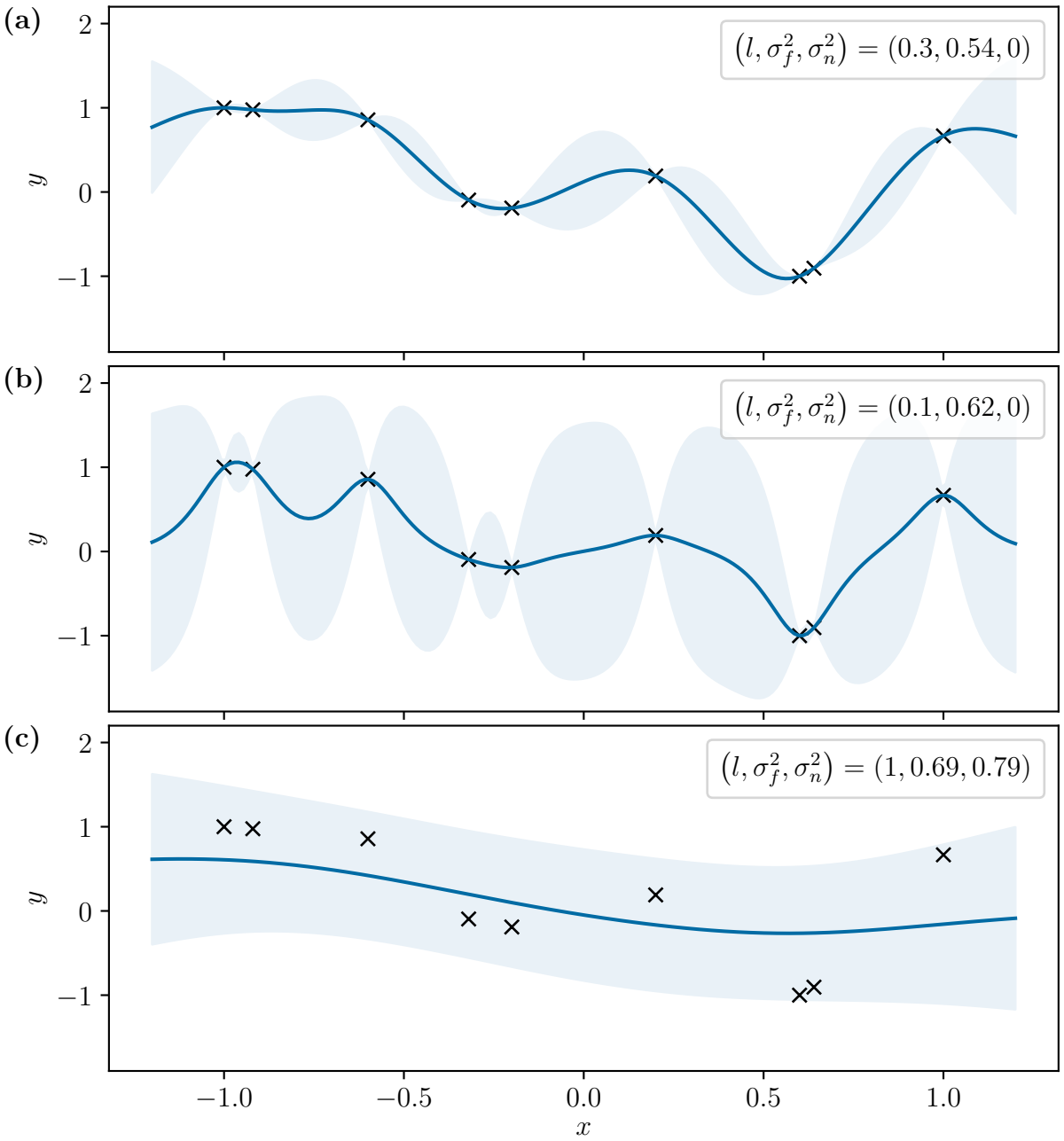

Figure 3.2: **(a)** A Gaussian process regression (GPR) model is fitted to the observed noise free data points (black crosses). The resulting hyperparameters are $\left(l, \sigma_f^2, \sigma_n^2\right) = (0.3, 0.54, 0)$. For all plots the mean is drawn as a solid blue line and the blue shaded region depicts the 95 % confidence interval, i.e. the uncertainty. **(b)** The hyperparameters, mainly the characteristic length-scale, are changed to $(0.1, 0.62, 0)$. This leads to a greater flexibility of the searched function f, i.e. the mean, and also to a much larger uncertainty. **(c)** The values of the hyperparameters are $(1, 0.69, 0.79)$, which results in a slowly varying function f. Here, noise is assumed on the observed data points. Adapted from [7].

where ν is a positive parameter and K_ν a modified Bessel function [7]. The Euclidean distance of $\boldsymbol{x}_p$ and $\boldsymbol{x}_q$ is scaled by the characteristic length-scale l. For $\nu \to \infty$ the RBF kernel is obtained. Inserting half-integer values for ν in Equation (3.9) results in quite simple equations. In particular, $\nu = \frac{5}{2}$ is widely used in machine learning. It is twice mean-square differentiable and has the form

$$k(\boldsymbol{r}) = \sigma_f^2 \left(1 + \sqrt{5}r + \frac{5}{3}r^2\right) \mathrm{e}^{-\sqrt{5}r} + \sigma_n^2 \delta_{pq} \tag{3.10}$$

considering all hyperparameters, where δ_{pq} is the Kronecker delta. If the inputs are multivariate, usually a separate length-scale l is introduced for each dimension.

To visualize the influence of these hyperparameters, the length-scale l is varied in Figure 3.2. Fitting the GPR model with the Matérn kernel from Equation (3.10) to the data points marked as black crosses yields $l = 0.3$, as shown in Figure 3.2a. Decreasing the length-scale to $l = 0.1$ results in a greater flexibility of the function f. Due to assumed noise free data points there is no decrease in the noise variance σ_n^2, but for a noisy data set there is, because of the greater flexibility already mentioned. Furthermore, it is noticeable that the confidence interval in Figure 3.2b and thus the uncertainty is significantly larger than before and it increases sharply after each data point. For a longer length-scale $l = 1$, as in Figure 3.2c, the model assumes noisy data, which is why it does not traverse the data points exactly. Instead, it is a slowly varying function.

It is crucial to highlight that the selection of the kernel not only influences the accuracy of the predictions but also affects the quality of the model uncertainty.

3.2 Gaussian process regression

In order to make predictions, the posterior is needed, which contains the knowledge about the observed data used for training. For the sake of generality, noisy data

$$y = f(\boldsymbol{x}) + \epsilon \tag{3.11}$$

is assumed with independent Gaussian noise ϵ, which has the variance σ_n^2. This changes the prior from Equation (3.3) analogously to Equation (3.10), where the variance σ_n^2 is simply added to the kernel with a Kronecker delta. The points used for training are $\{(\boldsymbol{x}_i, y_i) | i = 1, \dots, n\}$. According to the prior, the joint distribution of the training and

the test outputs, $\boldsymbol{y}$ and $\boldsymbol{f}_*$, is [7]

$$\begin{bmatrix} \boldsymbol{y} \\ \boldsymbol{f}_* \end{bmatrix} \sim \mathcal{GP}\left(0, \begin{bmatrix} \boldsymbol{K}(X,X) + \sigma_n^2 \mathbb{1} & \boldsymbol{K}(X,X_*) \\ \boldsymbol{K}(X_*,X) & \boldsymbol{K}(X_*,X_*) \end{bmatrix}\right) . \tag{3.12}$$

Here, X_* is the set of new input points at which the predictions $\boldsymbol{f}_*$ of GP are sought. Assuming there are n_* number of test points, then $\boldsymbol{K}(X,X_*)$ is an $n \times n_*$ matrix containing all pairwise covariances between the training and test points. The same applies for $\boldsymbol{K}(X,X)$, $\boldsymbol{K}(X_*,X_*)$ and $\boldsymbol{K}(X_*,X)$. Considering only the functions which traverse through the training points results in the posterior distribution. This is illustrated in Figure 3.1. For this purpose, the joint Gaussian prior distribution is conditioned on the training points, leading to

$$\boldsymbol{f}_*|X,\boldsymbol{y},X_* \sim \mathcal{GP}\left(\bar{\boldsymbol{f}}_*, \mathrm{cov}(\boldsymbol{f}_*)\right) , \tag{3.13}$$

with

$$\boldsymbol{\mu}(X_*|X,\boldsymbol{y}) = \bar{\boldsymbol{f}}_* = \mathbb{E}[\boldsymbol{f}_*|X,\boldsymbol{y},X_*] = \boldsymbol{K}(X_*,X)[\boldsymbol{K}(X,X) + \sigma_n^2\mathbb{1}]^{-1}\boldsymbol{y} , \tag{3.14}$$

$$\boldsymbol{\sigma}^2(X_*|X) = \mathrm{cov}(\boldsymbol{f}_*) = \boldsymbol{K}(X_*,X_*) - \boldsymbol{K}(X_*,X)[\boldsymbol{K}(X,X) + \sigma_n^2\mathbb{1}]^{-1}\boldsymbol{K}(X,X_*) . \tag{3.15}$$

These are the key predictive equations for GPR [7], resulting in the posterior distribution, with the mean function $\boldsymbol{\mu}$ ($\mu_i = m(\boldsymbol{x}_i)$) in Equation (3.14) and the covariance function $\boldsymbol{\sigma}^2$ in Equation (3.15), that can be used to predict $\boldsymbol{f}_*$ at the respective input points X_*, as shown in Figure 3.1b.

To optimize the hyperparameters Θ, the log marginal likelihood (LML) is required, which is defined as

$$\log p(\boldsymbol{y}|X) = -\frac{1}{2}\boldsymbol{y}^\top(\boldsymbol{K}(X,X) + \sigma_n^2\mathbb{1})^{-1}\boldsymbol{y} - \frac{1}{2}\log\left|\boldsymbol{K}(X,X) + \sigma_n^2\mathbb{1}\right| - \frac{n}{2}\log 2\pi . \tag{3.16}$$

A short characteristic length-scale that might improve the data fit is not preferred by the LML. Rather, maximizing the LML (maximum likelihood estimation) leads to a value which increases the likelihood that the training data would be generated by the distribution over functions [46]. This technique is particularly powerful because the LML is differentiable with respect to the hyperparameters Θ_i and utilizes only the available training data.

There are different Python packages to perform GPR. The one used in this work is GPflow.

4 Low-Dimensional Matrix Models

The main goal of the new method for finding EPs using GPR is to reduce the number of exact diagonalizations to calculate the eigenvalues, as this is the most time-consuming and computationally expensive step. Similar to the three-point and octagon method the new GPR method requires the two eigenvalues associated with the EP. An observed permutation of these eigenvalues is used as initial training set, since it confirms the existence of an EP inside the orbit. In higher-dimensional systems, it is not straightforward to select the eigenvalues that perform the permutation due to overlap with other resonances. For this purpose, in Section 4.1, the stepwise grouping algorithm is developed to filter the permutation and thus obtain the initial training set. In Section 4.2, a GPR model is trained on the κ and their corresponding p and s values (cf. Equations (2.55) and (2.56)). By performing a two-dimensional root search on the model prediction of p, a prediction for the position of the EP in parameter space κ is obtained. The eigenvalues of the κ dependent matrix can be calculated exactly for the predicted κ value. Again, the eigenvalues belonging to the EP need to be selected from the computed eigenvalues. Therefore, a similarity measure is introduced in Section 4.3 where the exact eigenvalues are compared to the GPR model prediction. The selected exact eigenvalues and their corresponding κ value is used as additional training point to improve the GPR model and obtain a better prediction. Thus, an iterative process is constructed. To terminate this procedure, a convergence criterion is required. Some possible criteria are discussed in Section 4.4.

The new method for finding EPs using GPR is first presented using matrix models to verify its functionality as well as its accuracy. The matrix in Equation (2.48) has two EPs which can be calculated analytically (cf. Section 2.5.1). In the following, only the one at $\kappa_+ = \mathrm{i}$ is considered, which is shown in Figure 2.5 with the corresponding permutation behavior of the two eigenvalues.

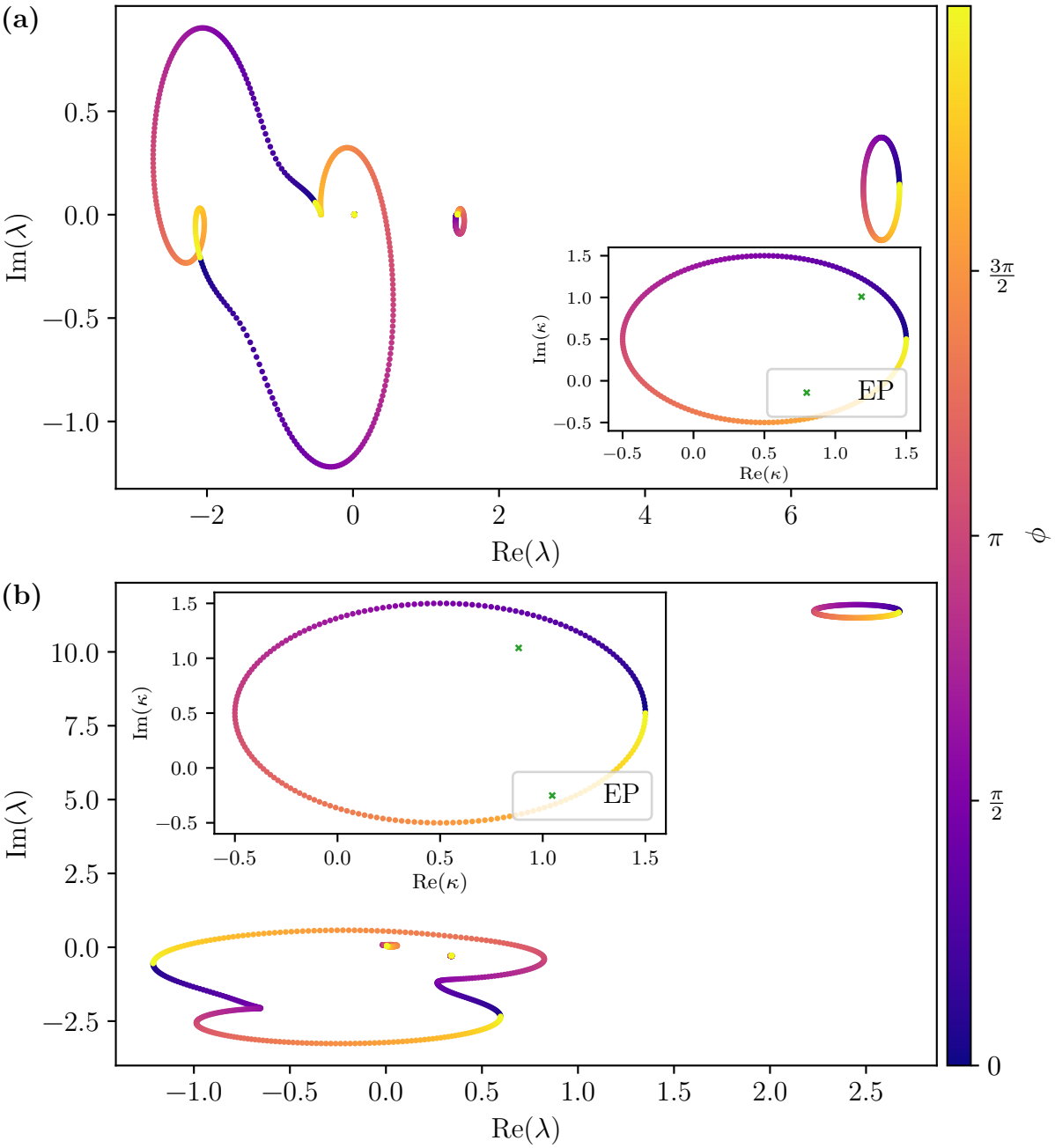

Figure 4.1: Both investigated five-dimensional matrix models are visualized with their respective energy and parameter plane. The EP, found via a two-dimensional root search on p without a GPR model, is marked as a green cross for each system. Due to their dimensionality, five eigenvalues are visible, and their course can be traced via the color bar, which represents the angle ϕ, when the EP is encircled. Both models show one permutation each, which indicates the existence of an EP. The shape of these permutations is complex because of the large radius and the fact that the EP is not at the center of the orbit. **(a)** In the first model, one eigenvalue lies within the visible exchange behavior. **(b)** For the second system, there are two eigenvalues therein.

To address the complexity of more challenging systems, two five-dimensional matrix models are introduced for which no analytic solution exists. Due to their complexity, the method must account for difficulties that are not present in the two-dimensional model due to its simplicity. By extending the analysis to higher-dimensional systems, the properties and characteristics of EPs in the context of more realistic environments will be examined.

Both five-dimensional matrix models are illustrated in Figure 4.1. The parameter plane with the orbit around the EP, highlighted in green, as well as the energy plane are presented. As already mentioned, both systems are not analytically solvable. However, the computational effort to diagonalize the matrix and hence get the eigenvalues is low, which is why the EP can be found by performing a two-dimensional root search on p without the GPR model, where only the two eigenvalues belonging to the EP are considered. The result is marked as a green cross in the parameter plane for both models. Due to their dimensionality, each diagonalization yields five eigenvalues. In the first model (cf. Figure 4.1a), one eigenvalue lies within the visible permutation of the two eigenvalues of the EP, while in the second system (cf. Figure 4.1b) there are two. All eigenvalues not belonging to an EP form a closed orbit similar to the one in parameter space. Given that the EPs do not occupy the central position within the parameter plane's orbit, the shapes of the observed permutation paths exhibit significantly greater complexity compared to the relatively straightforward two-dimensional example depicted in Figure 2.5.

As the GPR model necessitates the incorporation of the two eigenvalues associated with the EP, the observed permutation needs to be distinguished from the other eigenvalues. To address this challenge a stepwise grouping algorithm is developed in the subsequent Section to acquire the initial training set.

4.1 Stepwise grouping algorithm

By confining the analysis solely to the start and end point of the orbit, it becomes comparatively straightforward to discern the permutation. Specifically, the distance between the two eigenvalues associated with a given resonance should be zero throughout, except for the two resonances affiliated with the EP. However, due to the sorting of eigenvalues based on their real components, the arrangement of eigenvalues can vary across different points in the parameter space. Consequently, group them based on the resonances to which the eigenvalues correspond would yield a simple and effective approach to obtain an initial dataset suitable for training the GPR model. This is why the stepwise group-

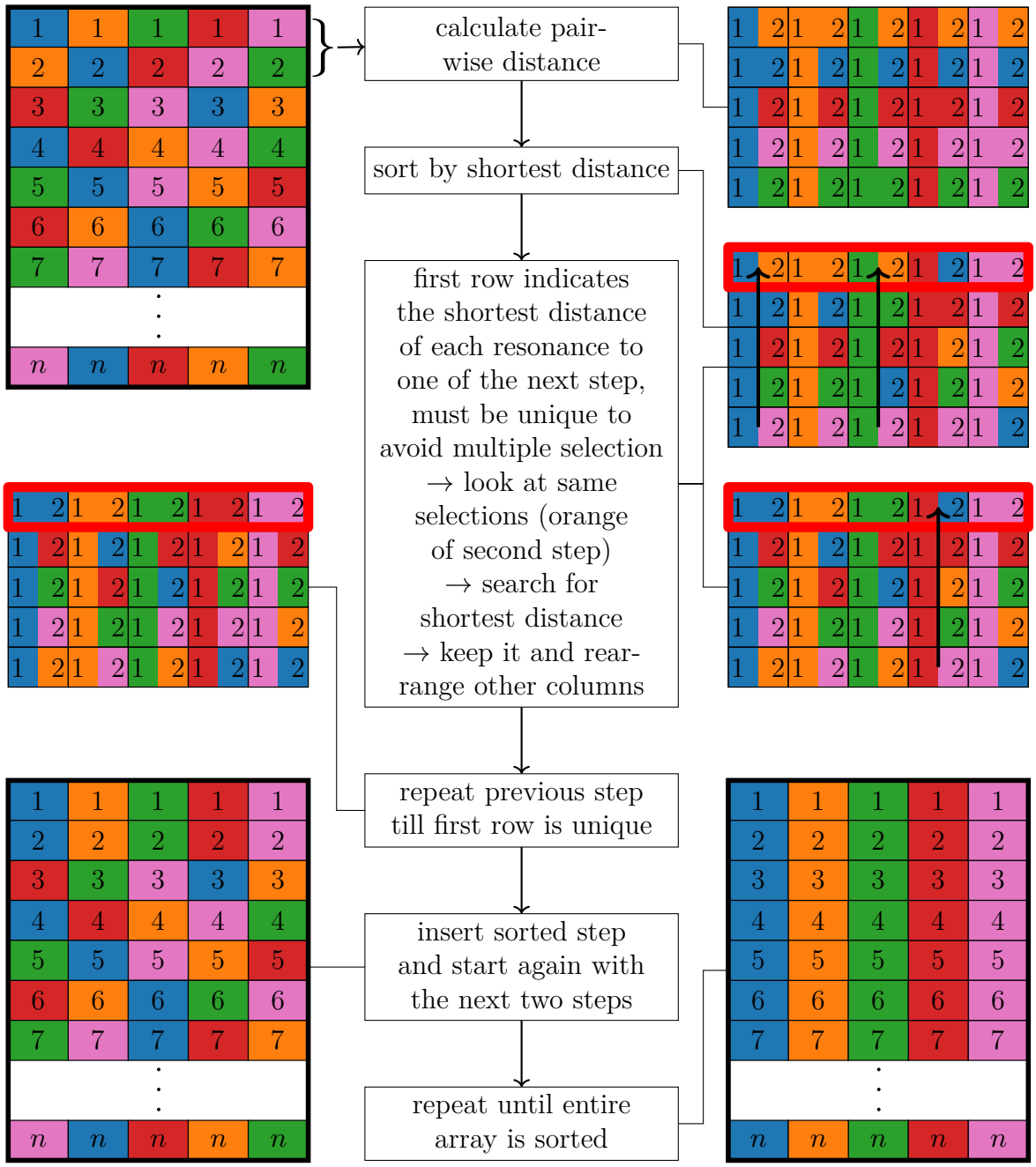

Figure 4.2: The stepwise grouping algorithm is illustrated. Colors represent resonances, while numbers indicate angles in the parameter space. Initially, eigenvalues are sorted by their real part in the top-left array. Pairwise distances between the first two rows are computed, resulting in the top-right matrix. Columns are then sorted by shortest distance, resulting in the matrix below. To ensure unique selections, only the shortest distance of multiple selections are kept and iterative rearrangements according to the arrows are done until the first row becomes unique, as shown in the middle-left matrix. The sorted row is inserted into the bottom-left array, and the process is repeated for each angle, yielding a sorted array based on resonances (bottom-right).

ing algorithm was developed. The fundamental concept behind it is that, for a given resonance, the eigenvalue associated with the subsequent angle is determined as the one with the closest proximity to the eigenvalue of the current angle, utilizing an appropriate distance metric.

Its functionality is illustrated in Figure 4.2. The five distinct colors employed in this figure correspond to five resonances, hence representing five eigenvalues for each diagonalization. The numbers signify the specific angle on the orbit within the parameter space, denoted as $\{\kappa_i = \kappa_\mathrm{c} + \varrho \mathrm{e}^{\mathrm{i}\phi_i} | i = 1, 2, \dots, n\}$, where κ_c denotes the orbit's center. The array located in the top-left exhibits all eigenvalues for each step i, sorted by their real components and thus unsorted with respect to the resonances. To facilitate grouping, the first two rows are extracted and the pairwise distances between them are computed, yielding the resulting matrix in the top-right. Since each column represents the distances from one resonance of the first step to all resonances of the second step, the columns are sorted in ascending order based on the shortest distance, generating the matrix below. The first row of this matrix, highlighted by a red frame, displays the shortest distance for each eigenvalue in the first row to one of the eigenvalues in the second row. To ensure the unique selection of each eigenvalue, this row must contain distinct elements. However, in the present case, the orange resonance of the second step appears three times. Consequently, a closer examination of these three distances is conducted to identify the shortest among them, ideally corresponding to the distance between the orange resonance of the first step and the orange resonance of the second step. The remaining two columns are then rearranged according to the indicated arrows, shifting the second shortest distance to the first row and moving the previous entry to the bottom of the column. This process leads to the creation of the third matrix on the right. The procedure is repeated iteratively until the first row of the resulting matrix becomes unique, as illustrated on the left side. The sorted row is subsequently inserted into the array displayed in the bottom-left, and the entire process is initiated again with the subsequent two rows, namely the second and third rows. By repeating this process for all angles, the final sorted array depicted in the bottom-right is obtained. A Python implementation of this algorithm can be found in Appendix A.

In calculating pairwise distances, various metrics can be utilized depending on the available data. For the matrix models, the real and imaginary parts of the eigenvalues are computed and combined into a vector

$$\boldsymbol{\lambda} = \begin{pmatrix} \mathrm{Re}(\lambda) \\ \mathrm{Im}(\lambda) \end{pmatrix}. \tag{4.1}$$

The Euclidean distance metric is employed, defined as

$$d_\mathrm{e} = \|\boldsymbol{\lambda}_1 - \boldsymbol{\lambda}_2\| = \sqrt{\left(\mathrm{Re}(\lambda_1) - \mathrm{Re}(\lambda_2)\right)^2 + \left(\mathrm{Im}(\lambda_1) - \mathrm{Im}(\lambda_2)\right)^2}\,, \tag{4.2}$$

which is suitable for the matrix models. However, for cuprous oxide, the complex-valued eigenvalues and additional quantum numbers are computed, which can be combined into an M-dimensional vector $\boldsymbol{\Psi}$. In this case, it is preferable to employ the cosine similarity

$$d_\mathrm{c} = 1 - \frac{\boldsymbol{\Psi}_1 \cdot \boldsymbol{\Psi}_2}{\|\boldsymbol{\Psi}_1\|\|\boldsymbol{\Psi}_2\|} = 1 - \frac{\sum_{l=1}^{M} \Psi_{1,l}\Psi_{2,l}}{\sqrt{\sum_{l=1}^{M} \Psi_{1,l}^2}\sqrt{\sum_{l=1}^{M} \Psi_{2,l}^2}}\,, \tag{4.3}$$

where the conventional definition of cosine similarity is subtracted from 1 to obtain small values for similar vectors.

Despite the algorithm's impressive performance, it is crucial to highlight an important consideration. In order to achieve accurate sorting of resonances, a sufficient number of points must be computed along the orbit to avoid significant variations in the eigenvalues between consecutive points. The exact number of points required depends on the radius of the orbit.

4.2 Model training

Similar to the three-point and octagon method, the eigenvalues are used to train the GPR. The permutation of the eigenvalues serves as a starting point because it indicates the existence of an EP. The two functions $p, s \in \mathbb{C}$ are defined in Equations (2.55) and (2.56), which depend on the eigenvalues and hence on κ. s will be important later on. Due to the coalescence of the eigenvalues, p should be zero at the EP. To train the GPR model,

$$\boldsymbol{p} = \begin{pmatrix} \mathrm{Re}(p) \\ \mathrm{Im}(p) \end{pmatrix} \in \mathbb{R}^2 \tag{4.4}$$

is used as observed function values $\boldsymbol{y}$ at specific points

$$\boldsymbol{\kappa} = \begin{pmatrix} \mathrm{Re}(\kappa) \\ \mathrm{Im}(\kappa) \end{pmatrix} \in \mathbb{R}^2 \tag{4.5}$$

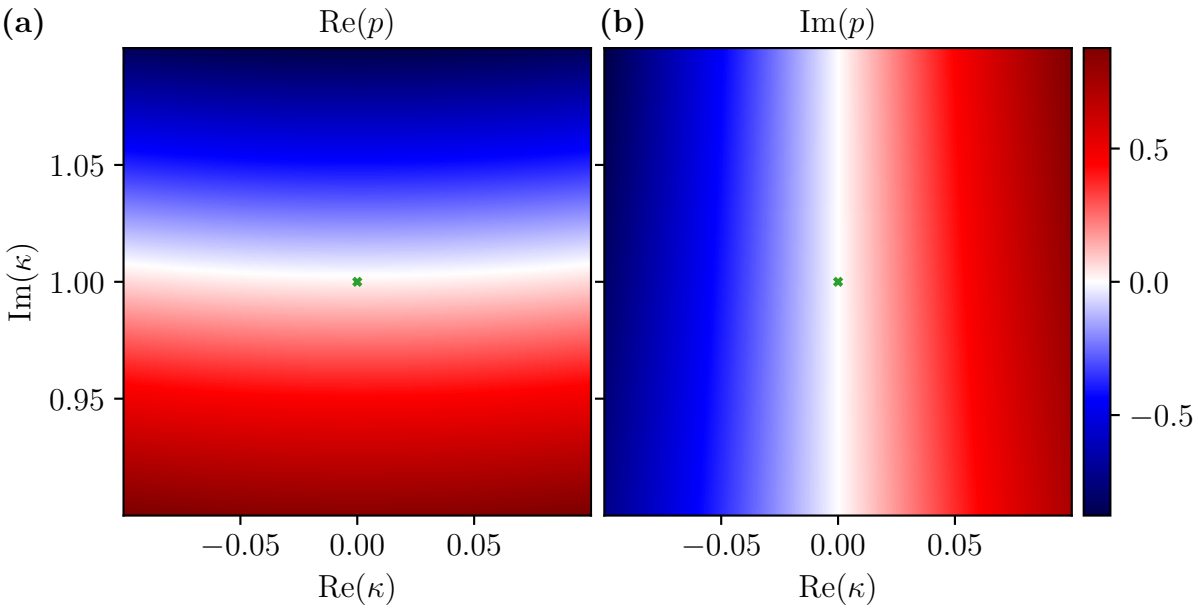

Figure 4.3: The GPR model prediction of $\boldsymbol{p}$ for the two-dimensional model system. The values of $\mathrm{Re}(p)$ and $\mathrm{Im}(p)$ are represented by the color bar and the exact position of the EP is marked as a green cross. Performing a two-dimensional root search on $\boldsymbol{p}$, yields a prediction for the position of the EP. This can be visualized by superimposing both plots and searching for the intersection of the two white lines. **(a)** The prediction for the real part of p has a curved zero line just above the exact position. **(b)** The imaginary part on the other hand already gives a good estimate because its zero line is almost exactly on top of the exact position.

corresponding to the training points X of Equation (3.13). Thus, it is possible to make predictions for $\boldsymbol{p}$ at new test points $\boldsymbol{\kappa}$. Performing a two-dimensional root search on the model output $\boldsymbol{p}$ yields a prediction of $\boldsymbol{\kappa}_{\mathrm{EP}}$ for the EP. The model prediction for the two-dimensional matrix model is shown in Figure 4.3, where the real and imaginary part of p are illustrated in Figures 4.3a and 4.3b, respectively. As visible, the two-dimensional root is already quite close to the exact position of the EP in parameter space κ, which is marked as a green cross.

The model prediction of $\boldsymbol{p}$ for both five-dimensional models is illustrated in Figure 4.4, where the numerical calculated EP is marked as a green cross. Compared to the simple system in Figure 4.3, the plane shows a much more complex behavior for the five-dimensional systems, which is expectable due to its dimension. Another reason is the larger radius of the orbit around the EP. The two-dimensional root of model 1 (cf. Figures 4.4a and 4.4b) as well as of model 2 (cf. Figures 4.4c and 4.4d) after the first

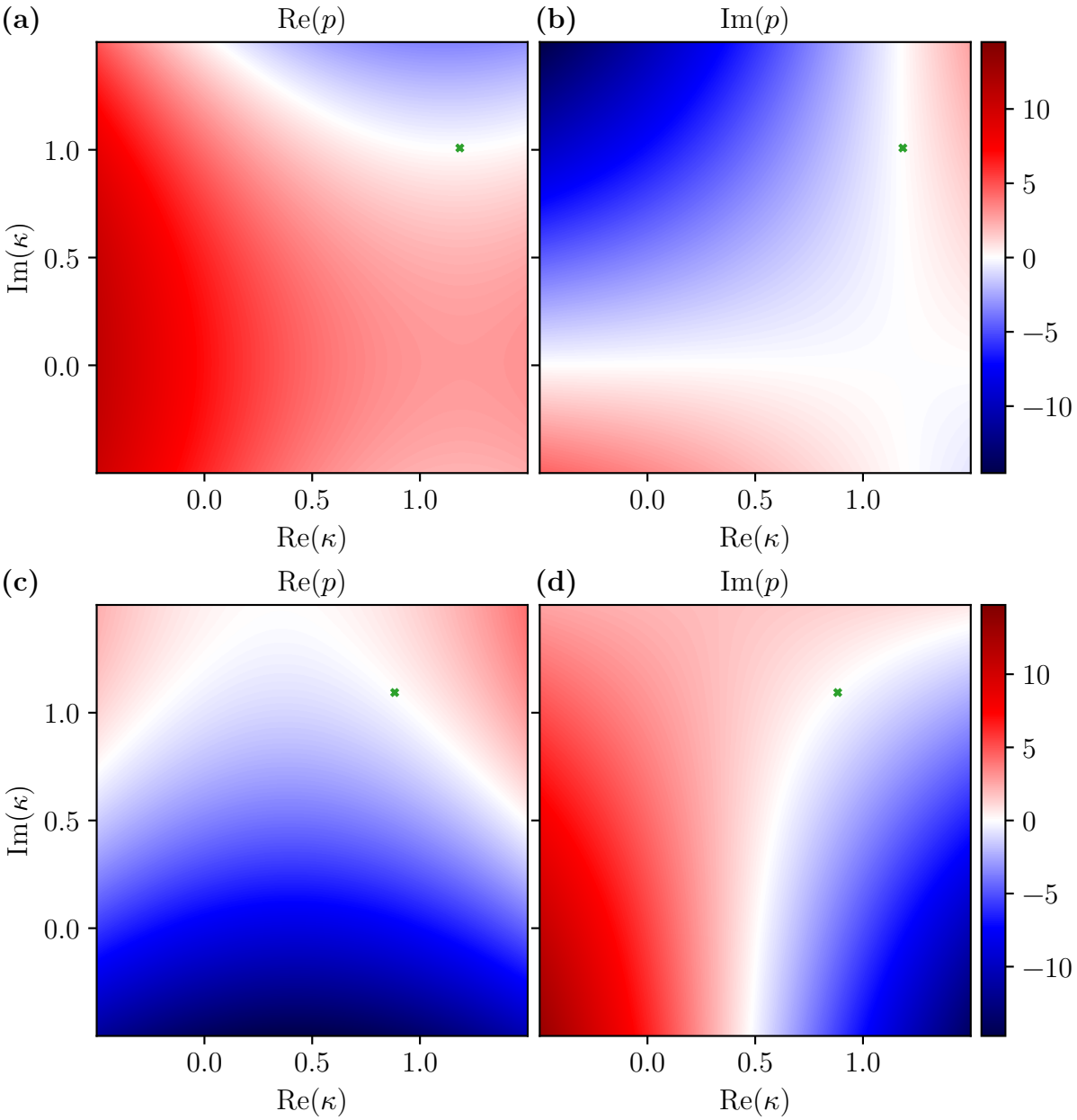

Figure 4.4: GPR model prediction of $\boldsymbol{p}$ for five-dimensional matrix model 1 (**(a)** and **(b)**) and 2 (**(c)** and **(d)**). The values of Re(p) and Im(p) are represented by the color bar and the exact position of the EP is marked as a green cross. The plots on the left show the prediction for the real part of p, while the imaginary part is on the right. Compared to the predicted $\boldsymbol{p}$ plane in Figure 4.3 a much more complex behavior is visible. This is due to the higher dimension of the systems, but is also related to the larger radius of the orbit. Analogous to the simple system, a prediction for the position of the EP is obtained by performing a two-dimensional root search which can be visualized by superimposing both plots of the respective model and searching for the intersection of the two white lines.

training step is already quite close to the exact position of the EP. Due to the large scale it is not possible to see any details in the close vicinity of the EP.

To construct an iterative process, an exact diagonalization is performed with the predicted parameter value. Then, the new pair of eigenvalues is used as additional training point for the GPR model. Repetitive iterations of this procedure yield a highly precise model, consequently enabling the determination of the precise location of the EP. However, the identification of the two eigenvalues associated with the EP in each iteration is not a straightforward task for higher-dimensional systems. The diagonalization of a five-dimensional matrix yields a total of five eigenvalues, but only the ones related to the EP warrant selection. Complicating matters further, there is no discernible permutation pattern that guides the selection process. In order to address this issue, a similarity measure is employed in the following Section to accurately identify the appropriate eigenvalues at each iteration.

4.3 New eigenvalue selection

To find the two eigenvalues associated with the EP in each iteration of the iterative process a similarity measure is introduced based on a Gaussian distribution

$$\mathcal{N}(\mu,\sigma) = \mathrm{e}^{-\frac{(x-\mu)^2}{2\sigma^2}} . \tag{4.6}$$

Here, the value of s in Equation (2.56) plays a significant role. The model predictions $\boldsymbol{p}$ and $\boldsymbol{s}$ at the predicted κ point are considered as μ and compared to the exact eigenvalues of the matrix at this κ point. To perform this comparison, all possible pairs of eigenvalues are formed, and their respective p and s values are calculated. Comparing them yields a compatibility

$$\begin{aligned} c = &\frac{\left(\mathrm{Re}(p)-\mathrm{Re}(p_\mathrm{m})\right)^2}{2\sigma^2_{\mathrm{p,Re}}} + \frac{\left(\mathrm{Im}(p)-\mathrm{Im}(p_\mathrm{m})\right)^2}{2\sigma^2_{\mathrm{p,Im}}} \\ &+\frac{\left(\mathrm{Re}(s)-\mathrm{Re}(s_\mathrm{m})\right)^2}{2\sigma^2_{\mathrm{s,Re}}} + \frac{\left(\mathrm{Im}(s)-\mathrm{Im}(s_\mathrm{m})\right)^2}{2\sigma^2_{\mathrm{s,Im}}} , \end{aligned} \tag{4.7}$$

which is small when there is good agreement between model prediction and exact eigenvalue pair. The index m indicates a model-predicted value and σ is the variance obtained from the GPR model for the respective prediction. For simplicity in calculation, only the exponent of Equation (4.6) is considered in the compatibility measure.

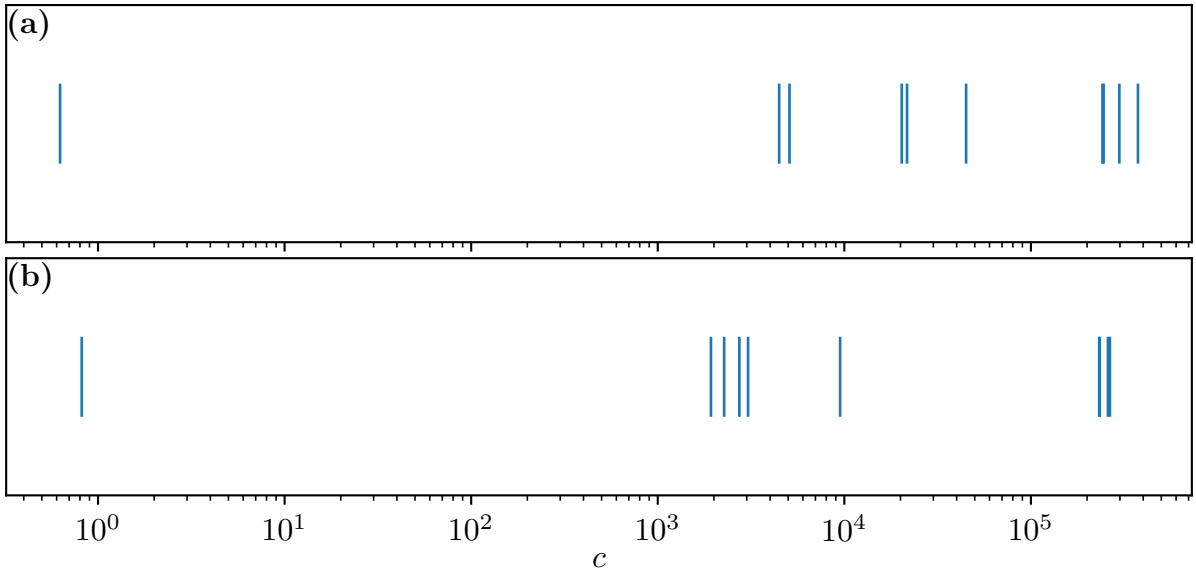

Figure 4.5: The figure presents the similarity measure employed for selecting the new eigenvalues in each iteration. The logarithmic plot displays the compatibility values defined in Equation (4.7). The calculations are performed after the first training step for **(a)** model 1 in Figure 4.1 and **(b)** model 2. In both models, a noticeable gap is observed between the smallest and second smallest compatibility values. This indicates that the eigenvalue pair with the lowest c value in each model is highly likely to correspond to the respective EP.

Ideally, there should be a large gap between the smallest and second smallest c value to make sure, that the correct eigenvalue pair is selected. Applying this similarity measure to both models in Figure 4.1 after the first training step, leads to the c values shown in Figure 4.5. As visible, there is indeed a large gap between the smallest and second smallest c value in both models. This observation strongly suggests that the eigenvalue pair that has the lowest c value in each model is most likely associated with the corresponding EP. Thus, this eigenvalue pair can be added to the training set to continue the iterative process.

It is worth noting that there are situations where the aforementioned gap may not be observed. This occurs when the variance of the model prediction is high, indicating a significant uncertainty in the model's prediction at that specific point. In such cases, the lowest c value does not necessarily correspond to the eigenvalue pair associated with the EP. This scenario typically arises when the predicted κ point lies outside of the orbit, indicating that the model's prediction is less reliable in capturing the behavior of the system in that region.

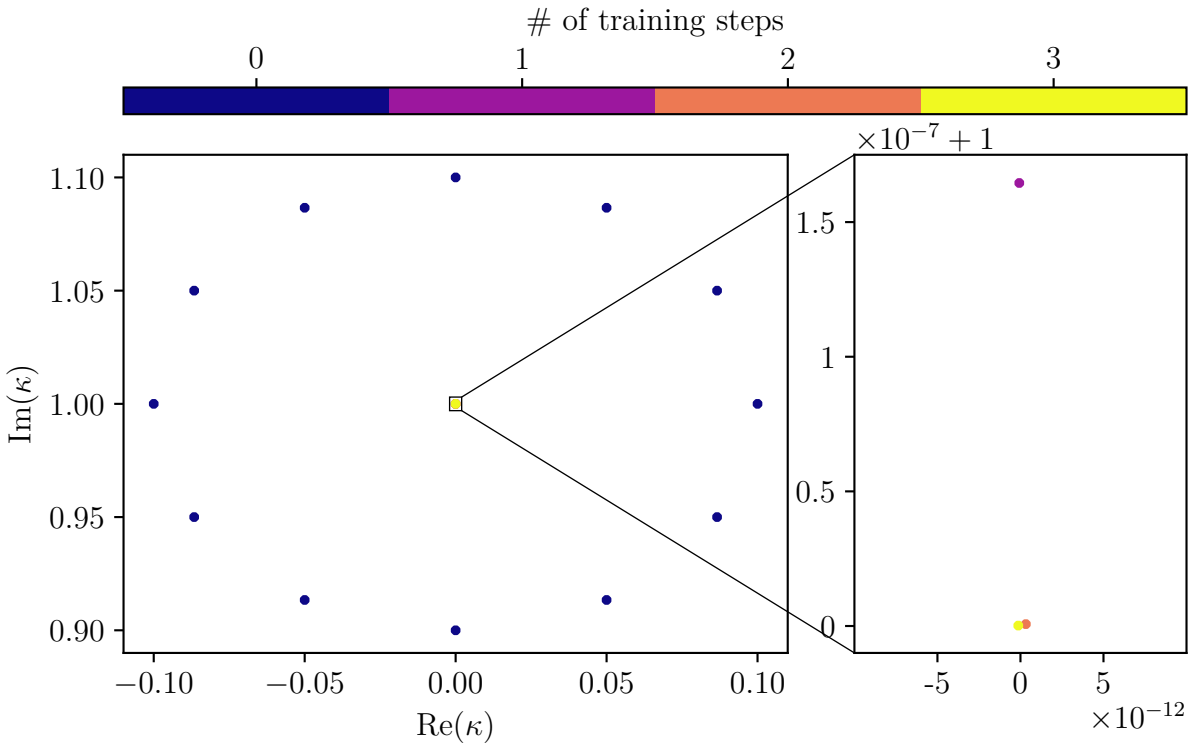

Figure 4.6: Illustration of the iterative process by means of the two-dimensional simple example. The EP at $\kappa_{\mathrm{EP}} = \mathrm{i}$ is encircled. These points, marked in blue, and their associated eigenvalues are used as initial training set. The model prediction of the exact position of the EP after this first training step is depicted in purple. For this κ-value, the eigenvalues of the matrix are calculated exactly and used together with the initial training set to optimize the GPR model. After the third training step, highlighted in yellow, the Euclidean distance between model prediction and exact position is $d = 1.62 \times 10^{-10}$.

After solving the challenge to find the two eigenvalues associated with the EP in each iteration, the iterative process can be applied to the matrix models. In Figure 4.6, the iterative process is illustrated using the simple two-dimensional example. Due to its simplicity, the prediction is already quite good after the first training step. However, after the second iteration it is significantly better and even the third training step improves the prediction slightly. The Euclidean distance between model prediction after the third training step and exact position of the EP is $d = 1.62 \times 10^{-10}$. In contrast to the illustration presented in Figure 2.5, a significantly reduced number of orbit points is employed during the model training process. This discrepancy arises due to the utilization of a numerical technique for computing the inverse of the covariance matrix $\boldsymbol{K}^{-1}$, a prerequisite for generating predictions, as described in Equations (3.14) and (3.15). When an excessive number of closely situated points is provided, numerical inaccuracies

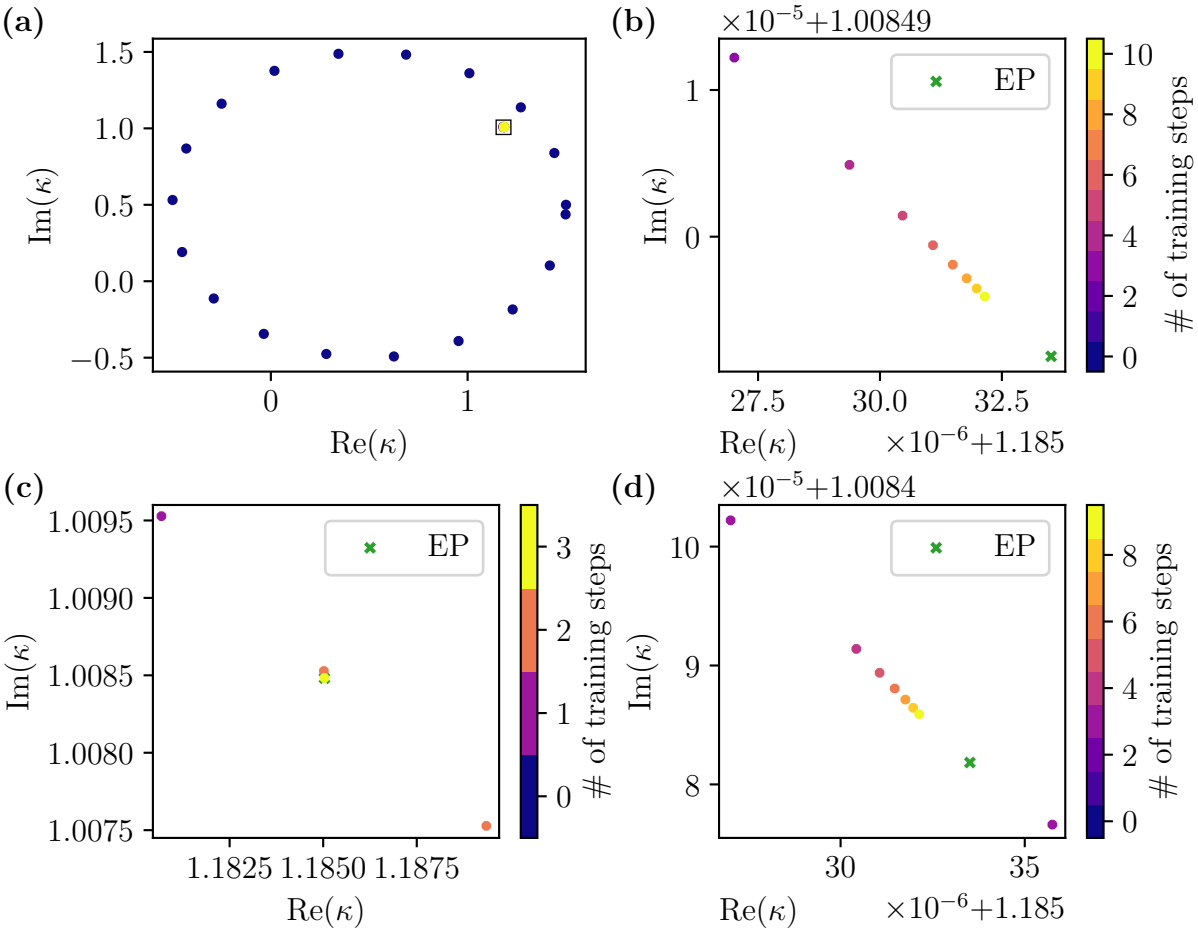

Figure 4.7: Illustration of the iterative process by means of the five-dimensional matrix model 1. **(a)** The points on the orbit around the EP, marked in blue, and their associated eigenvalues are used as initial training set. **(b)** The model slowly approaches the EP, marked as a green cross. After ten training steps the GPR model is converged and the Euclidean distance between the last model prediction and the exact EP is $d_e = 4.303 \times 10^{-6}$. Two different attempts are made to optimize convergence and reduce the number of exact diagonalizations. **(c)** First, an additional training point is added after the second iteration to explore the energy plane. For this purpose, the difference of the last two predictions is calculated and added to the second prediction. This leads to convergence after the third training step, i.e. after the fourth diagonalization (considering the additional point). Not only the number of diagonalizations is significantly reduced, but also the Euclidean distance to $d_e = 8.620 \times 10^{-7}$. **(d)** Similarly to the previous approach, an additional training point is added after the third iteration. This does not reduce the number of diagonalizations (nine training steps, ten diagonalizations) nor does it improve convergence ($d_e = 4.294 \times 10^{-6}$).

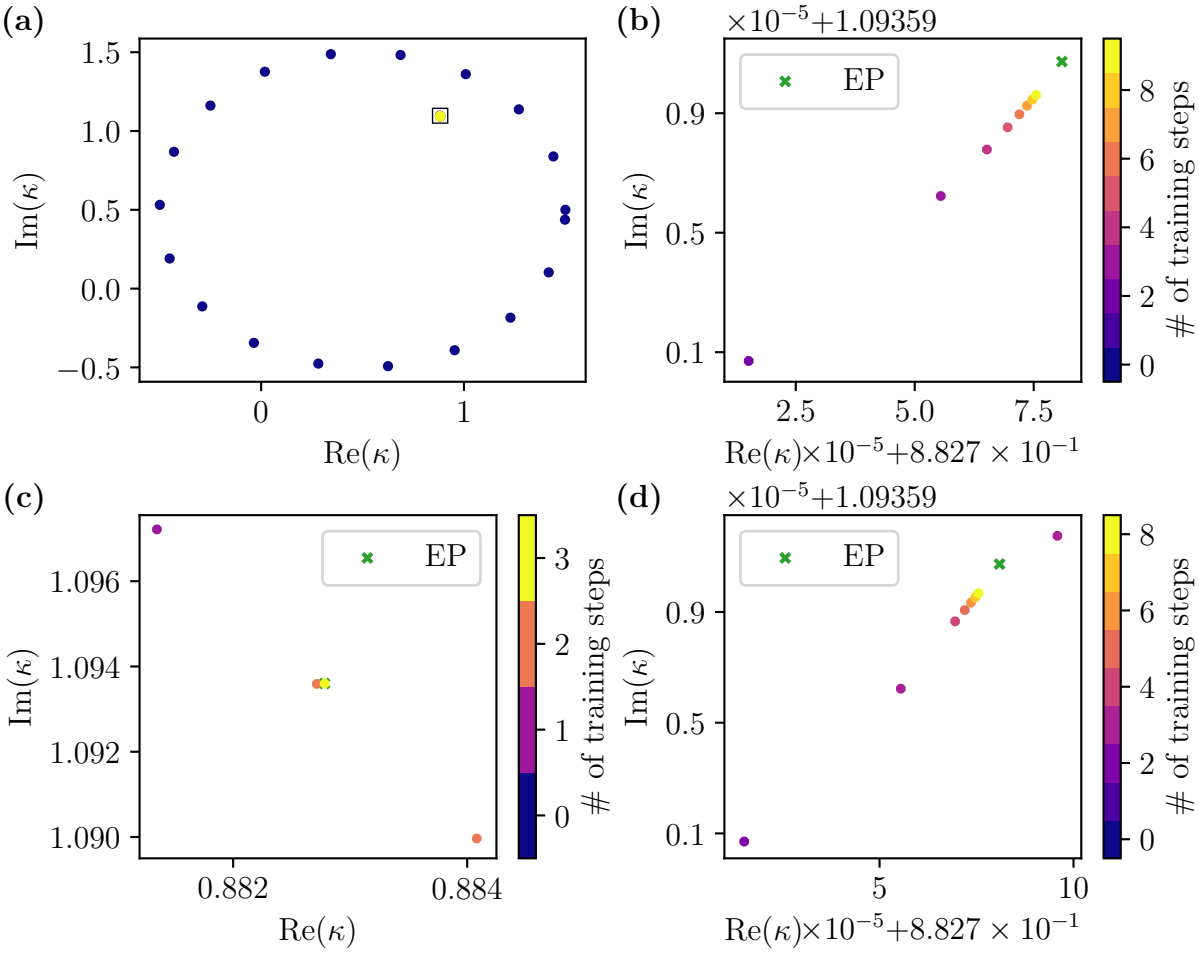

Figure 4.8: Illustration of the iterative process by means of the five-dimensional matrix model 2. For all four subfigures **(a)**, **(b)**, **(c)** and **(d)** holds the same as in Figure 4.7. The Euclidean distance between the exact position of the EP and the last prediction after the ninth training step in **(b)** is $d_e = 5.526 \times 10^{-6}$. Again, in **(c)** the number of diagonalizations is significantly reduced as well as the Euclidean distance to $d_e = 1.342 \times 10^{-6}$. In **(d)**, neither the number of diagonalizations is reduced (eight training steps, nine diagonalizations) nor the convergence is improved ($d_e = 5.537 \times 10^{-6}$).

can prevent the invertibility of the matrix $\boldsymbol{K}$, leading to a failure of the method.

The whole iterative process performed on the five-dimensional matrix models is depicted in Figures 4.7a and 4.7b for model 1 and in Figures 4.8a and 4.8b for model 2. In both cases the GPR model slowly approaches the EP until it converges after ten and nine training steps, respectively. The respective Euclidean distance between the exact EP and the last prediction is $d_\mathrm{e} = 4.303 \times 10^{-6}$ and $d_\mathrm{e} = 5.526 \times 10^{-6}$. In order to explore the energy plane and thus give more information to the GPR model, two attempts are made to both improve convergence and reduce the number of diagonalizations. An additional training point is added to the training set by calculating the distance between the last two predictions, adding it to the last prediction and computing the exact eigenvalues at this new κ point. If this is executed after the second iteration, not only the convergence improves significantly, but also the number of diagonalizations is reduced, both visible in Figure 4.7c for model 1 and in Figure 4.8c for model 2. For either model the number of training steps is decreased to three, i.e. four diagonalizations, and the respective Euclidean distance to the exact EP is $d_\mathrm{e} = 8.620 \times 10^{-7}$ and $d_\mathrm{e} = 1.342 \times 10^{-6}$. Adding the extra training point after the third iteration can be seen in Figure 4.7d for model 1 and in Figure 4.8d for model 2. Here, no improved convergence or reduced number of diagonalizations is observable. Compared to the original training process, the Euclidean distance is almost identical with $d_\mathrm{e} = 4.294 \times 10^{-6}$ and $d_\mathrm{e} = 5.537 \times 10^{-6}$ for model 1 and 2 respectively.

4.4 Convergence criteria

To terminate the iterative procedure, it is essential to establish a convergence criterion. Several potential options will be presented and discussed below.

4.4.1 Variance given by the GPR model

Equation (3.15) provides a variance and thus an uncertainty about the model prediction. As visible in Figure 3.1b, it is small in the vicinity of observed data points. If the variance for the predicted EP is small the model should be converged and hence the prediction quite good. However, determining an appropriate threshold value for this criterion can be challenging, and it is possible for the aforementioned matrix inversion error to arise prior to satisfying the convergence criterion. Furthermore, it is important to note that the criterion primarily evaluates the convergence of the model itself and does not address the convergence of the EP.

4.4.2 Distance between the last two predictions

In relation to the variance, an alternative approach involves examining the Euclidean distance between the last two predicted values. As previously mentioned, when these values are in close proximity, the variance is small. Selecting a suitable threshold value for this distance metric relies on the radius of the initial orbit around the EP, making it a more straightforward task to establish. However, similar to the previous convergence criterion, this method shares the same limitations in that it does not directly assess the convergence of the EP itself, and there remains a possibility of encountering issues with the invertibility of the matrix.

4.4.3 Eigenvalues of the covariance matrix

The eigenvalues $\lambda_{\boldsymbol{K}}$ of the covariance matrix $\boldsymbol{K}$ can be calculated for each training iteration. The parameter space (i.e. the κ-space) is the input space of the kernel function and thus the covariance matrix. As the number of κ-values increases, the eigenvalues decrease. If there are a lot of training points, especially if they are close together, a drop in the eigenvalues is visible from order $\mathcal{O}(10^{-7})$ to $\mathcal{O}(10^{-17})$. An interpretation for this drop is that the model has already seen this new training point, thus yielding no significant additional knowledge. This can also be used as a convergence criterion. As shown in Figure 4.9a for the two-dimensional matrix model, the drop occurs for the third training step depicted in yellow, coinciding with the proximity of the last two predictions (cf. Figure 4.6). Consequently, defining a threshold value for this criterion becomes relatively straightforward due to the noticeable deviation from the preceding training iterations.

The kernel eigenvalues of both models are plotted over the number of training points in Figure 4.10. The utilized data originates from the training process, where an extra training point is incorporated following the second iteration. Similar to the simple example in Figure 4.9a a drop ($\mathcal{O}(10^{-4})$ to $\mathcal{O}(10^{-10})$) in the kernel eigenvalues appears in the last training step in Figures 4.10a and 4.10c for model 1 and 2 respectively. This deviation from the previous training step facilitates the establishment of a threshold.

It is important to note that while this criterion does not provide insights into the convergence of the EP itself, its detection prompts the consideration of utilizing new training points, such as computing a new orbit in parameter space centered around the predicted EP with a smaller radius, to ensure the invertibility of the matrix. This criterion can be combined with other convergence parameters.

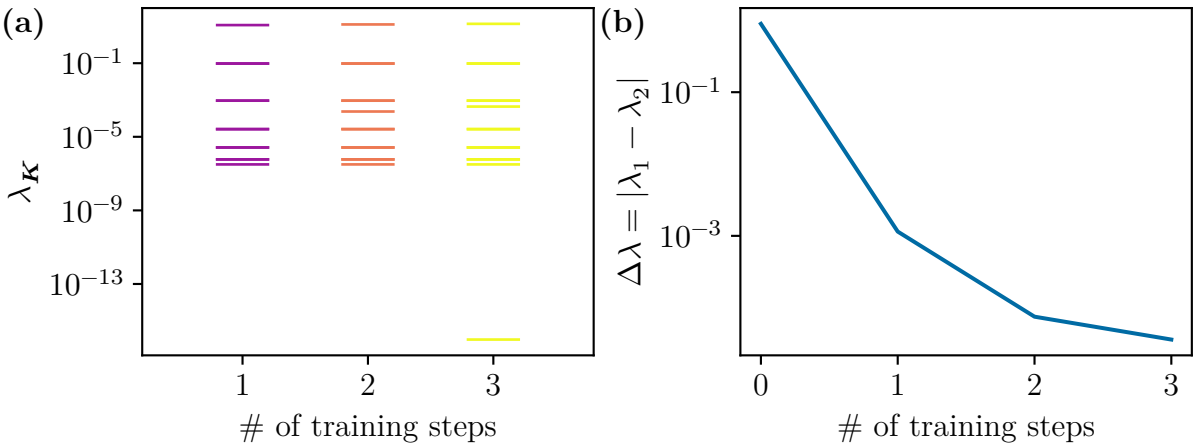

Figure 4.9: **(a)** The eigenvalues $\lambda_{\boldsymbol{K}}$ of the covariance matrix $\boldsymbol{K}$ are illustrated for each training step. A drop is visible in the third iteration from order $\mathcal{O}(10^{-7})$ to $\mathcal{O}(10^{-17})$ compared to the previous step. This indicates an already seen training point that does not provide any new information. Due to the clear deviation from the previous iteration an appropriate threshold value can be defined easily. **(b)** Another convergence criterion is the eigenvalue difference of the two eigenvalues belonging to the EP. It takes advantage of a direct property of the EP, namely the coalescence of the eigenvalues, and indeed decreases strictly monotonically. Defining a threshold value is not as straightforward as for the kernel eigenvalues, since no clear change is visible between the last two iterations.

4.4.4 Eigenvalue difference

At the EP the difference of the two eigenvalues $\Delta\lambda = |\lambda_1 - \lambda_2|$ should be zero due to their degeneracy. Because of the square root behavior mentioned in Section 2.5 the gradient is infinite at the EP. As a consequence, even slight changes in the κ-value can lead to significant variations in the difference between the eigenvalues. This strong dependency poses a challenge in identifying an appropriate threshold value for the eigenvalue difference as a convergence parameter. However, this is the only criterion directly related to a property of an EP. In Figure 4.9b, the eigenvalue difference $\Delta\lambda$ is plotted as a function of the number of training steps. Here, the eigenvalue difference of the zeroth training is calculated via

$$\Delta\lambda_0 = \frac{1}{N}\sum_{i=1}^{N} \left|\lambda_{1,i} - \lambda_{2,i}\right|, \tag{4.8}$$

where i denotes the index of the i-th training point κ_i on the orbit. As visible, the eigenvalue difference decreases strictly monotonically.

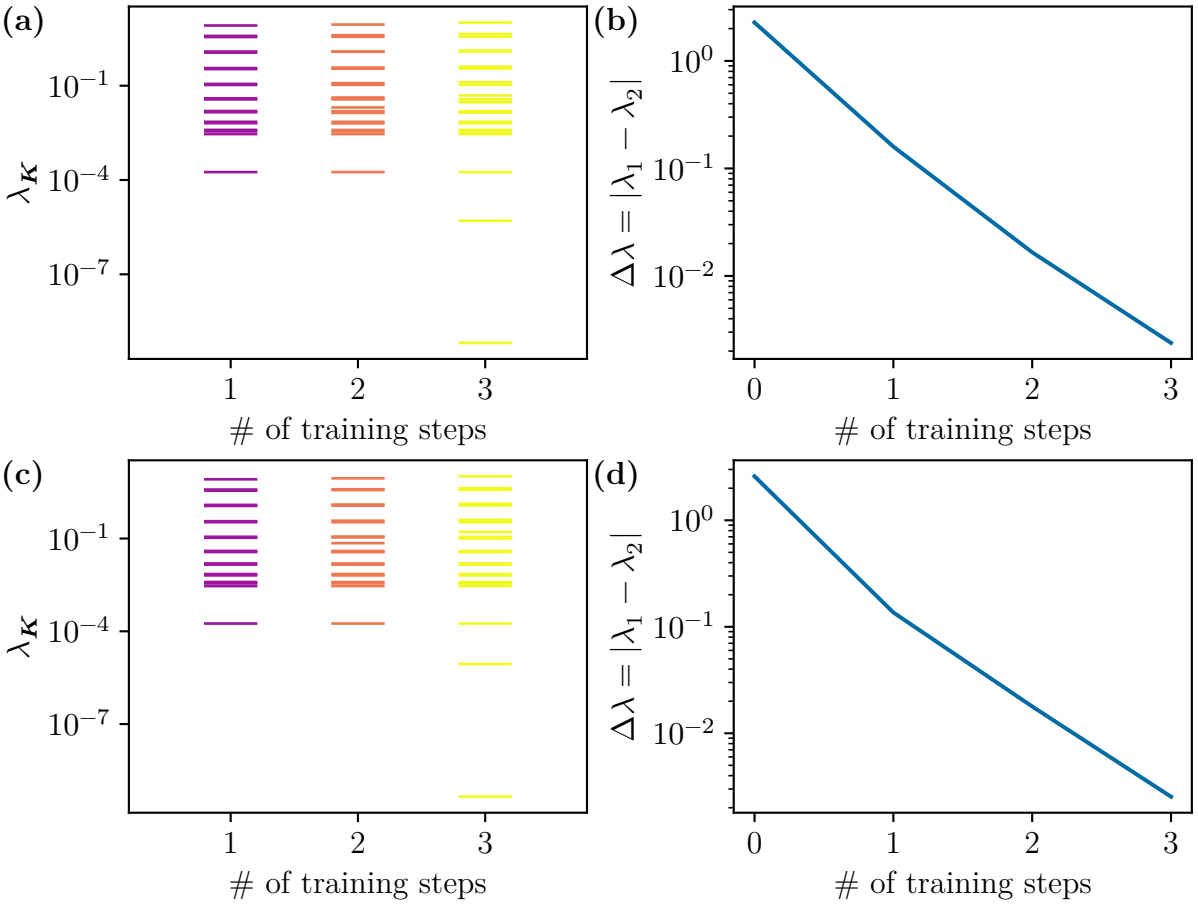

Figure 4.10: The two convergence criteria, namely the eigenvalues of the covariance matrix (cf. Section 4.4.3) and the eigenvalue difference (cf. Section 4.4.4), are shown for both model systems. For **(a)** model 1 and **(c)** model 2 the eigenvalues $\lambda_{\boldsymbol{K}}$ of the covariance matrix $\boldsymbol{K}$ are depicted for each training step. A drop is visible in the third iteration from order $\mathcal{O}(10^{-4})$ to $\mathcal{O}(10^{-10})$ compared to the previous step. This indicates an already seen training point that does not provide any new information. Similar to the simple example in Figure 4.9a a clear deviation to the previous training step is visible. Thus an appropriate threshold value can be defined easily to ensure the invertibility of the matrix. The eigenvalue difference of the two eigenvalues belonging to the EP for **(b)** model 1 and **(d)** model 2 is plotted over the number of training steps. The eigenvalue difference of the zeroth training step is calculated according to Equation (4.8), where N is the number of points on the orbit. For both models it decreases strictly monotonically, verifying convergence of the iterative process. Defining a threshold value is not as straightforward as for the kernel eigenvalues, since no clear change is visible between the last two iterations.

The eigenvalue difference the for five-dimensional matrix models are visualized in Figure 4.10. Again, the strictly monotonous decrease is observable which verifies the model's convergence towards the EP.

To terminate the iterative procedure, a combination of two convergence criteria is used, namely the eigenvalues of the covariance matrix and the eigenvalue difference of the two eigenvalues belonging to the EP.

5 Exceptional Points in Cuprous Oxide

The existence of EPs is already proven for the hydrogen atom [32]. Due to limitations especially in magnetic field strengths, only EPs of resonances with high quantum numbers are experimentally accessible in a hydrogen atom. The numerical calculations for these high quantum numbers are very expensive. For Cu_2O the field strengths to observe EPs of resonances with small quantum numbers are much lower compared to the field strengths for the hydrogen atom, which is why it is favorable to find EPs in this system. This was already done for a hydrogen-like model, but to obtain experimentally comparable results the band structure terms need to be considered. However, this increases the computational cost drastically for each diagonalization of the Hamiltonian. To minimize the number of diagonalizations and thus the computational cost, the new GPR method is now applied to the Hamiltonian (2.20) of Cu_2O. The Hamiltonian is dependent on the magnetic and electric field strength, γ and f respectively, which are expressed by

$$\kappa = \mathrm{e}^{\mathrm{i}\phi}\,, \tag{5.1}$$

$$\gamma = \gamma_\mathrm{c}\left(1 + \frac{\Delta\gamma}{\gamma_\mathrm{c}}\,\mathrm{Re}(\kappa)\right)\,, \tag{5.2}$$

$$f = f_\mathrm{c}\left(1 + \frac{\Delta f}{f_\mathrm{c}}\,\mathrm{Im}(\kappa)\right)\,, \tag{5.3}$$

$$\varrho = \frac{\Delta\gamma}{\gamma_\mathrm{c}} = \frac{\Delta f}{f_\mathrm{c}}\,. \tag{5.4}$$

These fields are aligned parallel to the symmetry axis [001] of Cu_2O. Here, κ is the unit circle in the complex plane and ϱ the so-called relative radius, so the variation of the field strengths, $\Delta\gamma$ and Δf respectively, depends on the center of the ellipse $(\gamma_\mathrm{c}, f_\mathrm{c})$. Due to this representation, the field strengths on the ellipse can be converted to their respective points on the unit circle in the complex plane κ, which is used to train the GPR model as explained in Section 4.2. For more details about the optimization of the

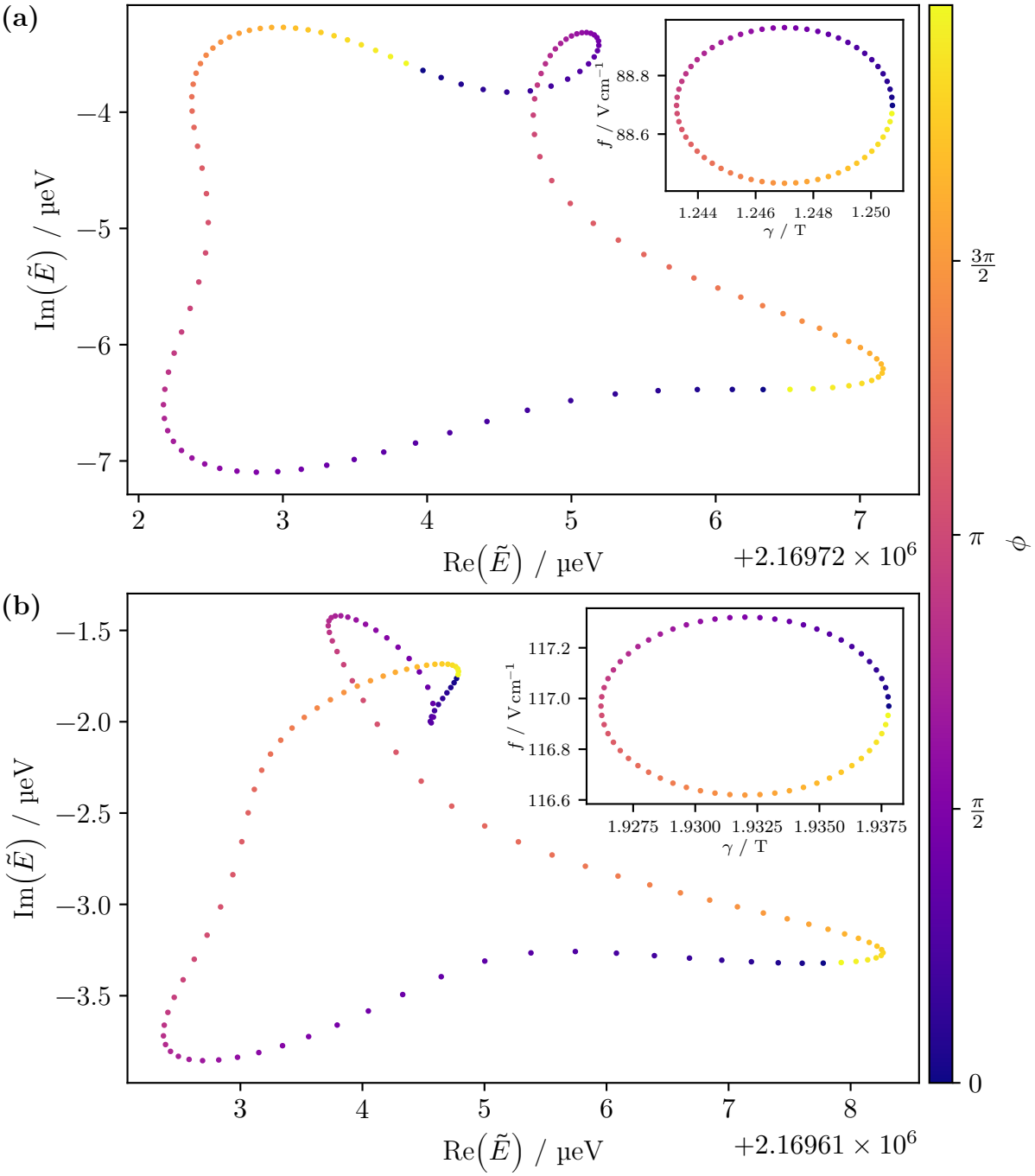

Figure 5.1: Two orbits in the field plane of magnetic (γ) and electric (f) field and their respective two eigenvalues which belong to the EP. To illustrate the permutation the color bar denotes the angle ϕ on the orbit. **(a)** Ellipse 1 and **(b)** 2 both show an exchange behavior, indicating an EP inside the respective orbit.

training process see Appendix B.

Ellipses in the field plane are computed to search for a permutation of two eigenvalues. Two example orbits and for each the two eigenvalues associated with the EP are shown in Figure 5.1. The different convergence parameters described in Section 2.4 are set to $N = 30$, $F_{\max} = 14$, $|\alpha| = 42$ and $\theta = 0.14$. In this case the radius is $\varrho = 0.3\,\%$ for both ellipses, corresponding to $\Delta\gamma = 5.796\,\mathrm{mT}, \Delta f = 0.351\,\mathrm{V/cm}$ and $\Delta\gamma = 3.741\,\mathrm{mT}, \Delta f = 0.266\,\mathrm{V/cm}$ for the respective ellipse, which is already quite small. Another crucial observation to emphasize is that both the real as well as the imaginary part of the energies are given in µeV, i.e. $\mathcal{O}(10^{-6})$. Due to these variations in the field strengths and the small energies it is necessary to adjust and optimize the iterative process. More details about this optimization can be found in Appendix B.

In Section 5.1, the application of the GPR method to Cu_2O is discussed, and several results are provided. Additionally, Section 5.2 explores the convergence radius in greater detail and presents relevant outcomes of the stepwise grouping algorithm as well as further results of the GPR method.

5.1 Applying the GPR method to Cu_2O

Due to the above mentioned scaling it is possible to apply the iterative process on the two orbits illustrated in Figure 5.1. After the first training step the prediction of $\boldsymbol{p}$ for both orbits is shown in Figure 5.2. Due to the small radius of $\varrho = 0.3\,\%$, which corresponds to $\Delta\gamma = 5.796\,\mathrm{mT}, \Delta f = 0.351\,\mathrm{V/cm}$ and $\Delta\gamma = 3.741\,\mathrm{mT}, \Delta f = 0.266\,\mathrm{V/cm}$ for the respective ellipse in Figure 5.1, their behavior looks quite simple. The two-dimensional zero search is performed on these predictions which yields a first educated guess of the position of the respective EP.

The eigenvalue selection described in Section 4.3 is applied on the resulting exact eigenvalues at that prediction, obtained by a diagonalization of the Hamiltonian (2.20) with the predicted field strengths. The gap in the compatibility c (cf. Equation (4.7)) between the best and the second best matching pair is of order $\mathcal{O}(10^6)$, indicating that the correct eigenvalues belonging to the EP are selected.

The iterative process converges after the fourth iteration for both ellipses as visible in Figure 5.3. In both cases, the first prediction is a little off. For the ellipse in Figure 5.3b the prediction of the third and fourth training step lie on top of each other. Regarding the last training steps, all field strengths vary only in the sixth significant digit, suggesting a decent result.

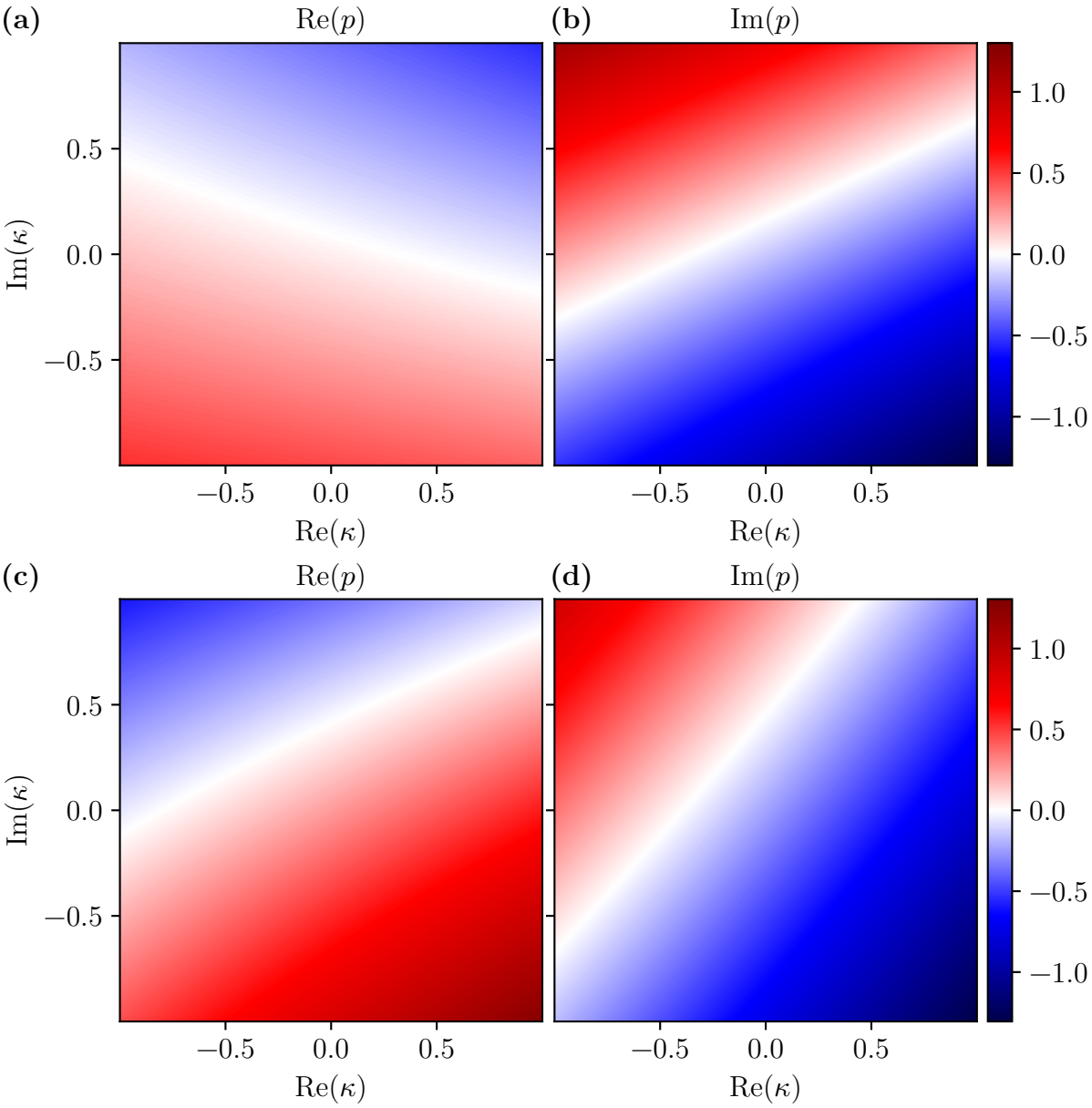

Figure 5.2: Prediction of $\boldsymbol{p}$ after the first training step. The subfigures **(a)** and **(b)** show the prediction for the orbit in Figure 5.1a, **(c)** and **(d)** show the prediction of the orbit in Figure 5.1b. Due to their small relative radius of $\varrho = 0.3\,\%$, corresponding to $\Delta\gamma = 5.796\,\mathrm{mT}, \Delta f = 0.351\,\mathrm{V/cm}$ and $\Delta\gamma = 3.741\,\mathrm{mT}, \Delta f = 0.266\,\mathrm{V/cm}$ for the respective ellipse, the observed behavior looks quite simple. Analogous to the model systems, a prediction for the position of the EP is obtained by performing a two-dimensional root search which can be visualized by superimposing both plots of the respective orbit and searching for the intersection of the two white lines.

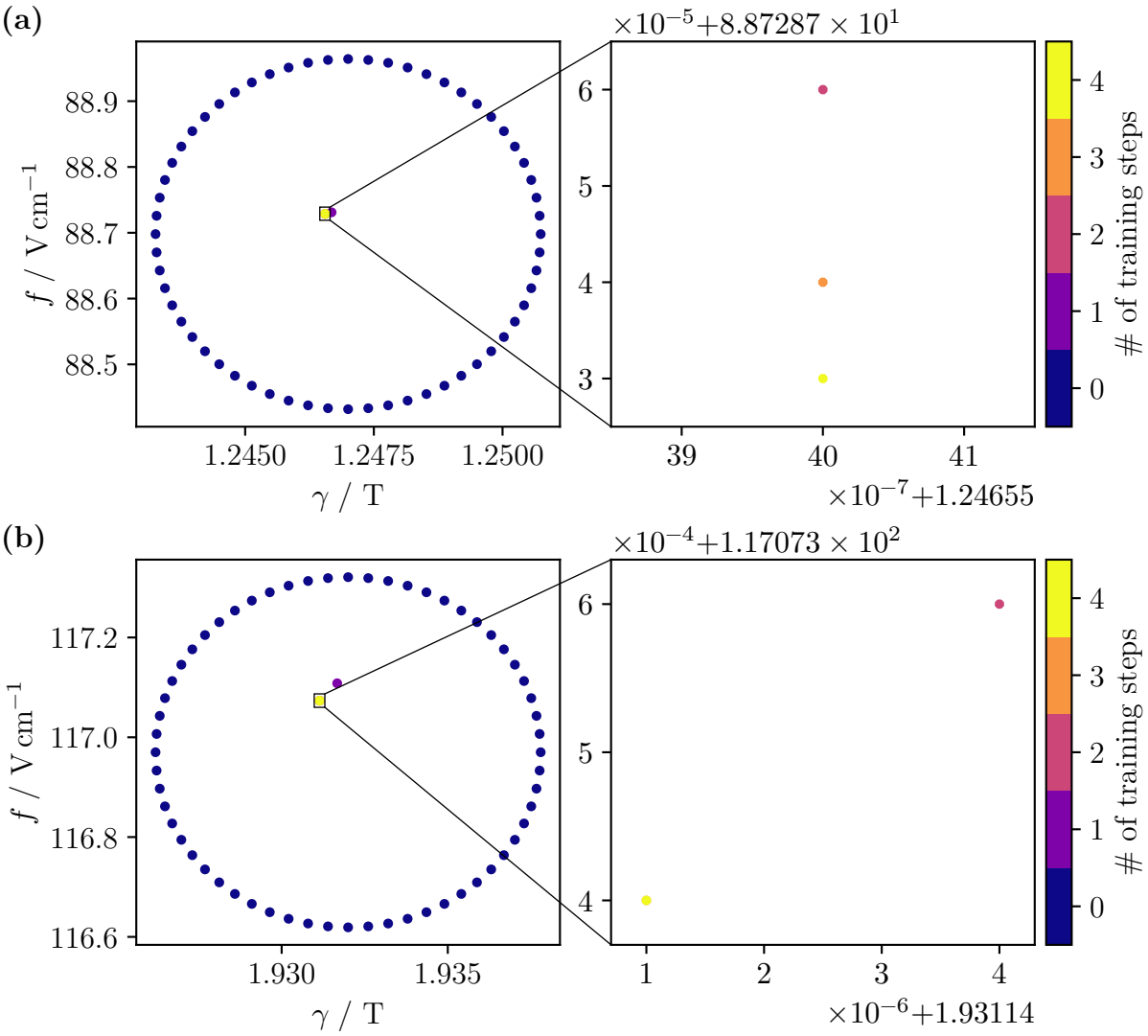

Figure 5.3: Applying the iterative process to the two orbits in Figure 5.1 yields the illustrated predictions of the respective EP. The iterative process for **(a)** ellipse 1 as well as **(b)** ellipse 2 converges already after the fourth training step. In **(b)** the last and second to last prediction lie on top of each other.

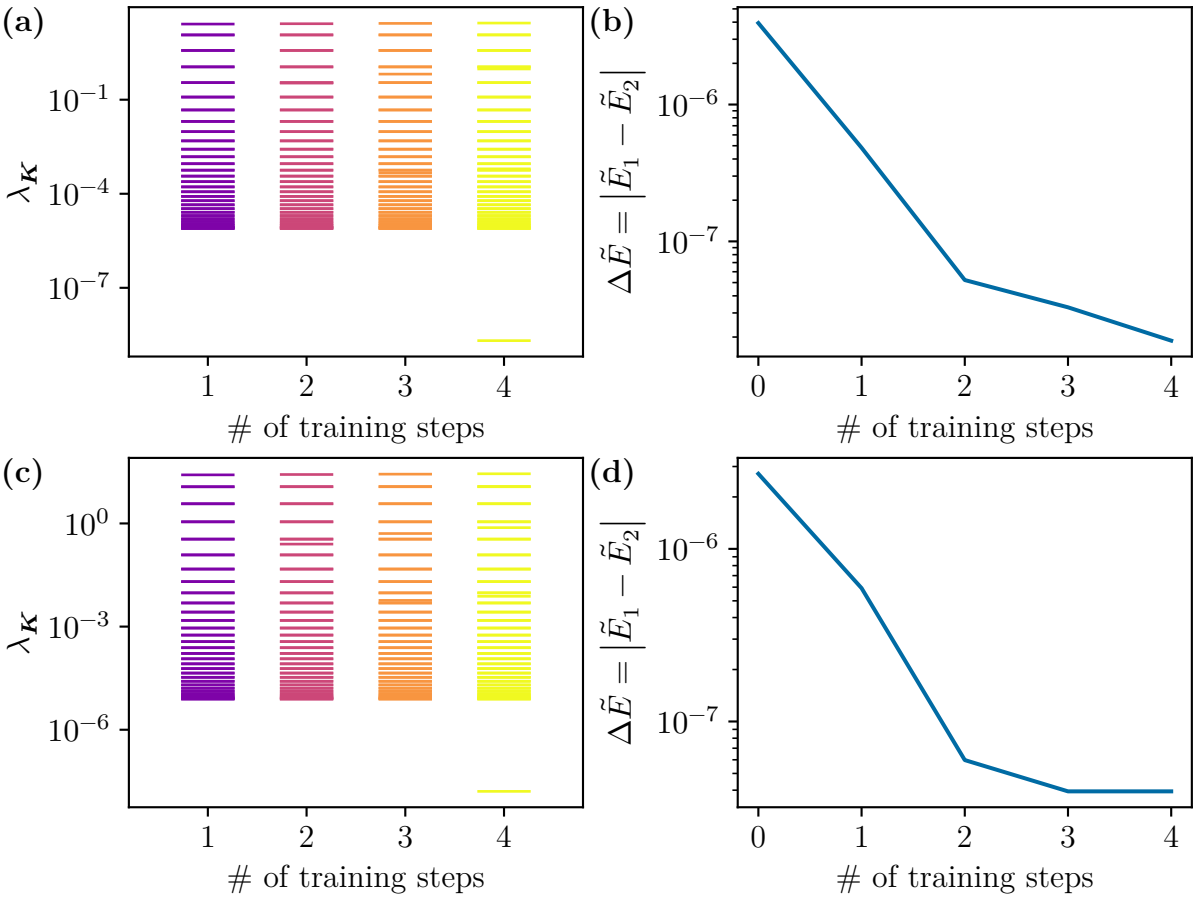

Figure 5.4: Convergence of the two EPs by means of the kernel eigenvalues $\lambda_{\boldsymbol{K}}$ described in Section 4.4.3 and the eigenvalue difference $\Delta\tilde{E}$ of the two eigenvalues belonging to the respective EP for the training processes in Figure 5.3a (**(a)** and **(b)**) and in Figure 5.3b (**(c)** and **(d)**). In both cases the significant drop in the kernel eigenvalues from order $\mathcal{O}(10^{-6})$ to $\mathcal{O}(10^{-9})$ and $\mathcal{O}(10^{-8})$ respectively is visible. This drop is accompanied by a very small or no change in the eigenvalue difference, suggesting the convergence of the method.

Having a look at the two convergence criteria in Figure 5.4 supports the assumption of a converged training process. Not only the drop in the kernel eigenvalues $\lambda_{\boldsymbol{K}}$ from order $\mathcal{O}(10^{-6})$ to $\mathcal{O}(10^{-9})$ and $\mathcal{O}(10^{-8})$ for the respective ellipse occurs, but also the eigenvalue distance $\Delta\tilde{E}$ of the two eigenvalues associated with the EP reduces significantly during the iterative process. Furthermore, the drop is accompanied by minimal or negligible alteration in the eigenvalue difference, indicating the convergence of the method.

Since the exact positions of the EPs are unknown, it is not possible to determine the exactness of the last predictions. However, as mentioned before, the deviation only in the sixth significant digit as well as the small eigenvalue difference indicates a very accurate result. This accuracy is of course related to the small radius of $\varrho = 0.3\,\%$. Due to the high computational effort required to reach such a small radius, the question arises whether the method also converges for a larger radius and whether the result is still as accurate in this case.

5.2 Results

To investigate the accuracy and the convergence radius, an ellipse with a radius of $\varrho = 6\,\%$ is drawn in the field plane, which corresponds to $\Delta\gamma = 77.733\,\mathrm{mT}$ and $\Delta f = 5.1966\,\mathrm{V/cm}$. This ellipse and the observed permutations in the energy plane are depicted in Figure 5.5. As a result of the large radius, there is a substantial overlap with other resonances. Consequently, when plotting all eigenvalues for each angle ϕ (cf. Figure 5.5a), only the leftmost permutation, which corresponds to the EP in Figure 5.3a, is visually distinguishable. Applying the stepwise grouping algorithm yields all permutations shown in Figure 5.5b. Therefore, it functions as a powerful tool to efficiently filter these permutations, facilitating the discovery of additional EPs. Thus, it generates a greater amount of training data for a single ellipse. To avoid possible issues with the stepwise grouping algorithm mentioned in Section 4.1, the orbit was discretized using 400 points to ensure that eigenvalues and their respective quantum numbers changed minimally between steps. This is of course computationally expensive, but nevertheless the overall computational workload is reduced drastically due to the discovery of additional EPs.

The leftmost permutation in Figure 5.5 is taken as initial training set to study the convergence of the method. Figure 5.6 visualizes the result of the iterative process. It

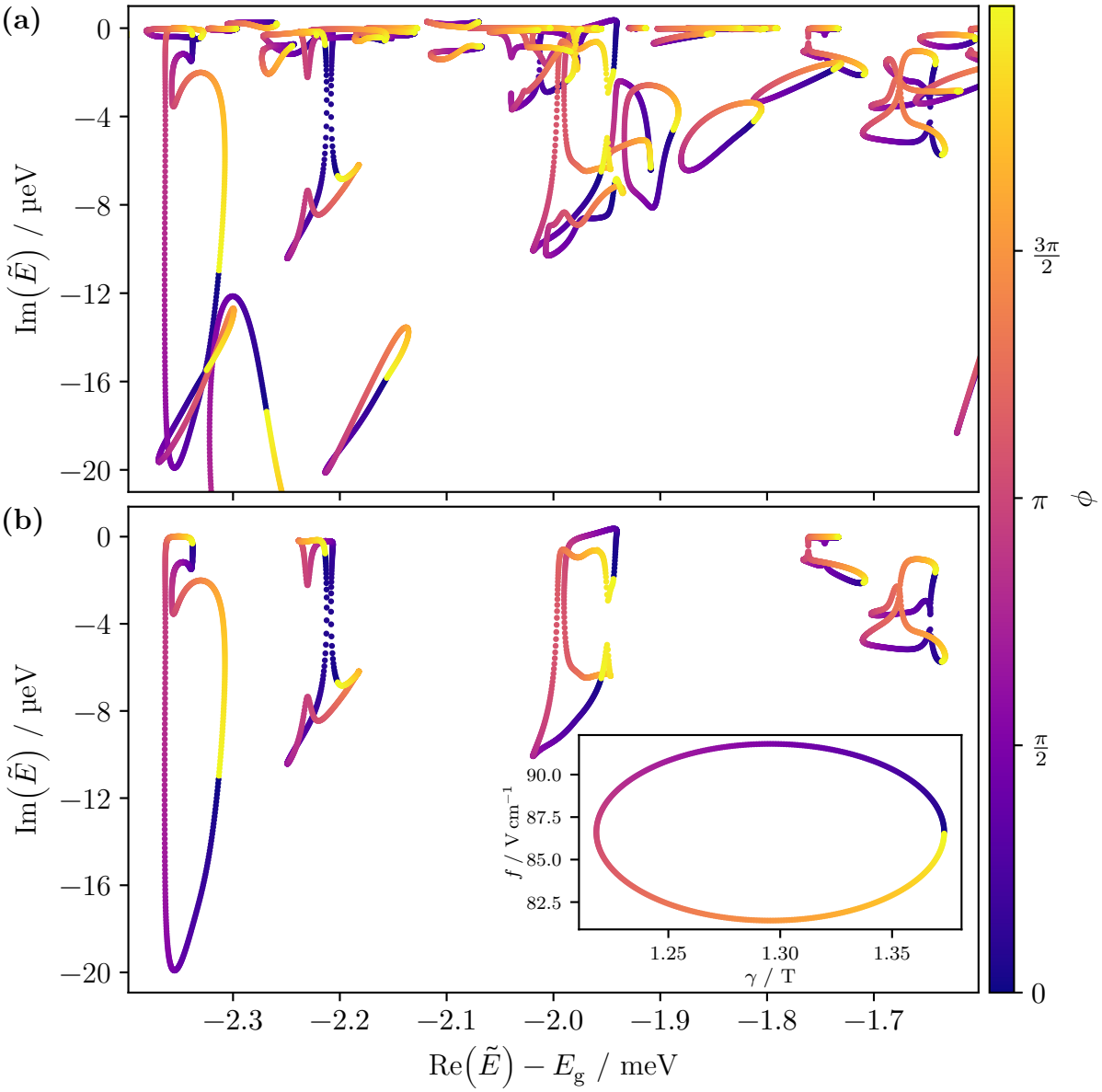

Figure 5.5: **(a)** Drawing an ellipse with a radius of $\varrho = 6\,\%$, corresponding to $\Delta\gamma = 77.733\,\mathrm{mT}$ and $\Delta f = 5.1966\,\mathrm{V/cm}$, results in the visible resonances for the given energy range. Here, the band gap energy E_g is subtracted from the real part of the energy. Due to the large radius, there exists a significant overlap with other resonances, resulting in only the leftmost permutation, which belongs to the EP in Figure 5.3a, being visually discernible when plotting all eigenvalues for each angle ϕ. **(b)** Applying the stepwise grouping algorithm yields five permutations. Consequently, this algorithm serves as a powerful tool to effectively filter these permutations, enabling the identification of additional EPs and, subsequently, generating more training data for a single ellipse. This approach effectively reduces the overall computational workload while increasing the number of EPs discovered.

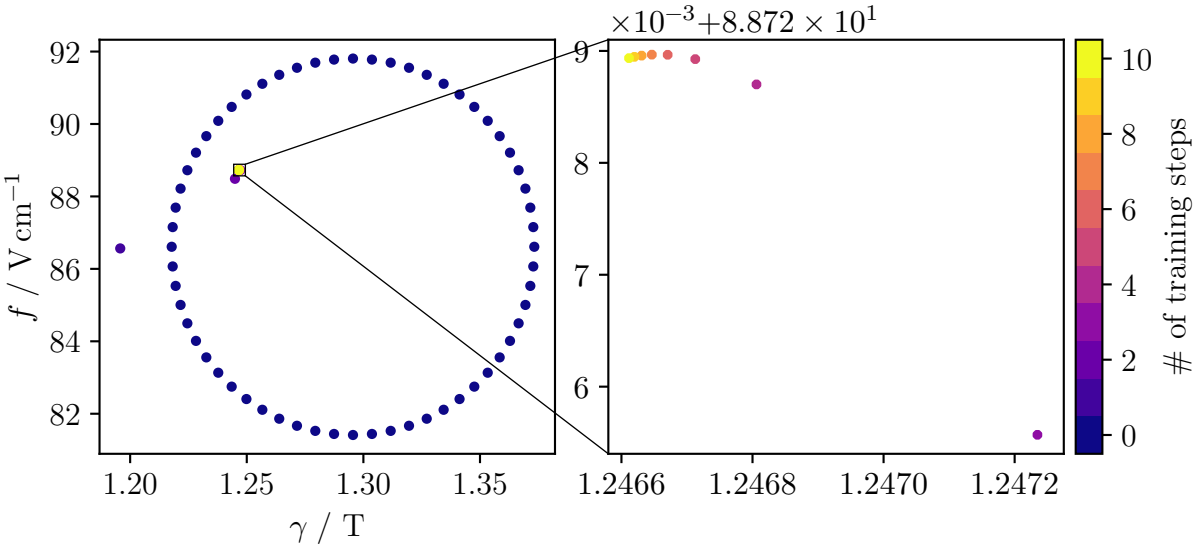

Figure 5.6: Applying the iterative process to the orbit in Figure 5.5 combined with the leftmost permutation as initial training set yields the illustrated prediction of the EP. It converges after ten training steps. The Euclidean distance to the prediction of the EP in Figure 5.3a is $d_e = 2.140 \times 10^{-4}$, thus the predicted field strengths are identical up to and including the fifth significant digit.

converges after ten training steps and leads to a similar position of the EP

$$\gamma_{\mathrm{EP,lr}} = 1.246\,612\,\mathrm{T}\,, \tag{5.5}$$

$$f_{\mathrm{EP,lr}} = 88.728\,936\,\frac{\mathrm{V}}{\mathrm{cm}} \tag{5.6}$$

as the prediction of the small radius in Figure 5.3a

$$\gamma_{\mathrm{EP,sr}} = 1.246\,554\,\mathrm{T}\,, \tag{5.7}$$

$$f_{\mathrm{EP,sr}} = 88.728\,730\,\frac{\mathrm{V}}{\mathrm{cm}}\,. \tag{5.8}$$

The indices lr and sr represent the large and small radius, respectively. Hence, the predicted field strengths are identical at least up to and including the fifth significant digit and the Euclidean distance is only $d_e = 2.140 \times 10^{-4}$. Thus, the iterative process converges and yields a fairly accurate prediction of the position of the EP even for such a large radius. The calculated eigenvalues of the Hamiltonian for the predicted field strengths (5.5) and (5.6) are illustrated in Figure 5.7. To distinguish the two eigenvalues belonging to the EP, they are marked by an arrow. Since the eigenvalues are almost degenerate, they are visually indistinguishable.

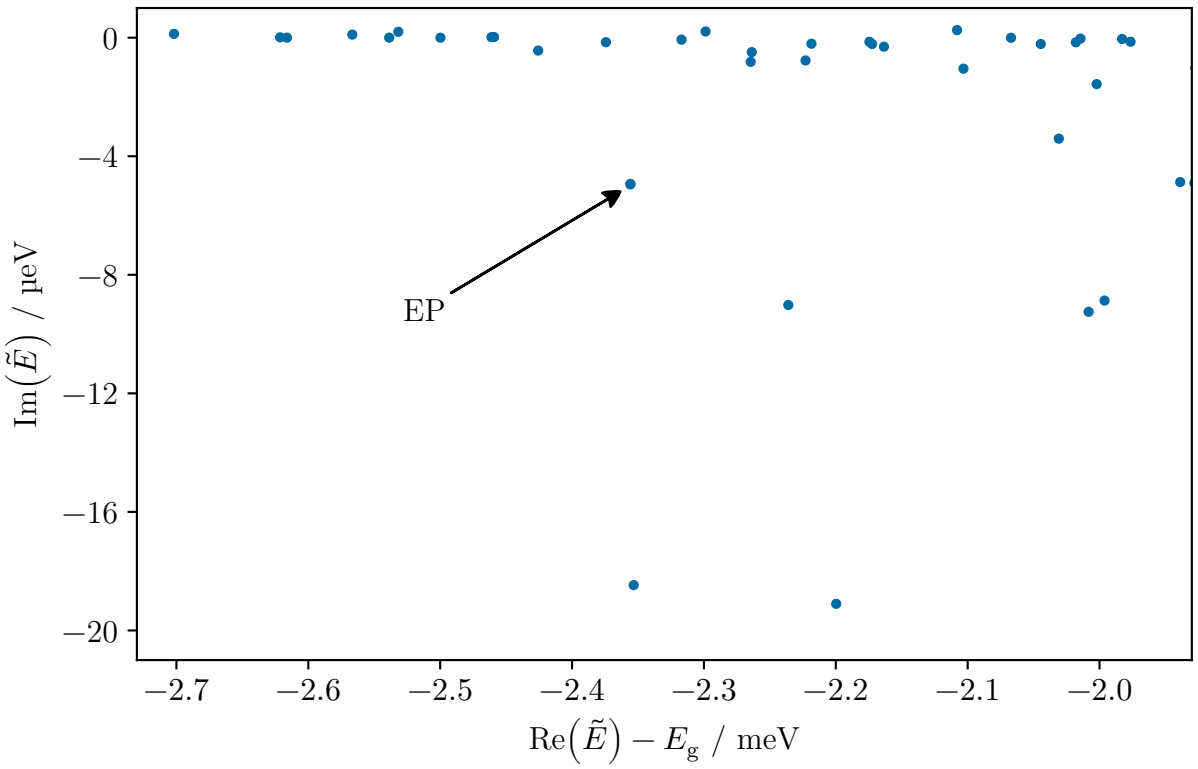

Figure 5.7: All eigenvalues for the given energy range calculated by diagonalizing the Hamiltonian (2.20) with the predicted field strengths of the EP in Equations (5.5) and (5.6). Here, the band gap energy E_g is subtracted from the real part of the energy. The two eigenvalues associated with the EP are marked by an arrow, but since they are degenerate, it is impossible to distinguish them visually.

By taking into account the efficiency of the stepwise grouping algorithm and the extensive convergence radius of the iterative procedure, there is a substantial reduction in computational costs. This is particularly evident when comparing it to the trial-and-error approach that involves using smaller ellipses to cover the region spanned by the larger ellipse, as discussed in references [9] and [37], but also compared to the existing methods, namely the three-point and octagon method.

It is worth emphasizing that the chosen radius of $\varrho = 6\,\%$ does not represent the maximum convergence radius. The largest radius tested is $\varrho = 15\,\%$, which corresponds to $\Delta\gamma = 319.650\,\mathrm{mT}, \Delta f = 20.558\,\mathrm{V/cm}$. The excellent results achieved with a relatively small number of training steps and the high accuracy suggest the potential for an even larger convergence radius. However, further testing would be required to confirm this. As the radius increases, the overlap between different resonances becomes even more significant, making it increasingly difficult to visually identify permutations.

Table 5.1: EPs in Cu_2O found using the new GPR method. For each EP, the magnetic (γ) and electric (f) field strengths as well as the complex energy $\tilde{E}$ are given. Here, the band gap energy E_g is subtracted from the real part of the energy. However, the convergence of the diagonalization of the Hamiltonian is questionable because some parameters could not be varied to ensure convergence.

EP	γ / T	f / V/cm	$\mathrm{Re}\left(\tilde{E}\right) - E_g$ / meV	$\mathrm{Im}\left(\tilde{E}\right)$ / µeV
1	1.184 658	85.348 284	−1.999 440	−4.103
2	1.218 638	85.829 520	−1.761 387	−0.545
3	1.246 554	88.728 730	−2.355 771	−4.942
4	1.252 867	82.244 780	−1.675 592	−2.798
5	1.308 150	87.574 636	−2.219 199	−4.282
6	1.338 139	108.084 785	−2.331 259	−3.295
7	1.931 141	117.073 400	−2.465 701	−2.575
8	1.931 221	117.076 754	−2.465 689	−2.576
9	1.950 923	106.762 009	−2.087 715	−1.249
10	2.049 782	156.927 751	−2.363 292	−0.965
11	2.356 121	143.134 723	−1.902 537	−12.337
12	2.419 380	131.213 089	−1.654 835	−2.685

Consequently, in order to ensure the effectiveness of the stepwise grouping algorithm, a greater number of points on the orbit would need to be computed for larger radii.

The first prediction in Figure 5.6 is located outside the orbit, which could cause problems in selecting the new eigenvalues of this point. If the predicted position of the EP is too far from the ellipse, the GPR model's prediction at that point becomes highly uncertain, resulting in a large variance $\boldsymbol{\sigma}^2$. According to Equation (4.7), this high variance leads to numerous eigenvalue pairs with extremely small values of c, increasing the probability of selecting an eigenvalue pair that does not correspond to the EP. Failure to select the correct pair can hinder the convergence of the GPR method. However, in the given scenario, there is still a notable gap between the lowest and second lowest values of c, on the order of $\mathcal{O}(10^2)$, suggesting that the correct eigenvalue pair is successfully selected.

Another possible issue observed when training with different EPs was that if the EP is in close proximity to the orbit, the matrix inversion error may occur before the GPR method converges. This can be remedied by using fewer points on the orbit to train the model, or by drawing a new ellipse with a slightly different center. In fact, this problem occurred only once in several cases where the EP was close to the ellipse.

All EPs found with the new method are listed in Table 5.1. The convergence of the diagonalization process for the Hamiltonian is hindered by certain challenges associated with the delta terms and the limited ability to adjust the convergence parameters related to the complex rotation angle, $|\alpha|$ and θ. Nonetheless, it is possible to vary the parameters N and F_{max}, which was done for one of the predicted EPs. Even with small variations a shift in the eigenvalues is observable, contradicting the convergence of the diagonalization. As a result, the reliability of the convergence of these EPs is questionable and needs to be investigated further. However, it is important to note that this issue does not impact the effectiveness and accuracy of the GPR method itself.

6 | Conclusion and Outlook

Applying an external magnetic and electric field to excitons in cuprous oxide results in resonances, i.e., quasi-bound states which can decay and possess a complex energy eigenvalue, the imaginary part describing the inverse lifetime. At certain electric and magnetic field strengths, exceptional points (EPs) can occur where the eigenvalues and eigenvectors of two resonances coalesce. One property of these EPs is that for an orbit around the EP in the field plane, the two eigenvalues belonging to this EP permute, i.e. they exchange their positions. Determining EPs is not so straightforward, mainly due to the computational cost of diagonalizing the exciton Hamiltonian of Cu_2O. Thus, a new method to find EPs is developed in this thesis.

In Chapter 3, the concept of Gaussian processes (GPs) was introduced within the framework of machine learning. By specifying a distribution over functions and considering only those that fit the observed data points, predictions can be made for new data points, given a model uncertainty for these predictions. This Gaussian process regression (GPR) approach was employed in the new method.

The GPR method was developed gradually by means of matrix models in Chapter 4. An observed permutation of the eigenvalues belonging to the EP was used as initial training set, since it confirms the existence of an EP inside the orbit. In higher-dimensional systems, it is not straightforward to select the eigenvalues that perform the permutation due to overlap with other resonances. The main challenge was to extract these eigenvalues, so the stepwise grouping algorithm was developed in Section 4.1 to solve the initial training set problem. The underlying principle of this approach is to determine the eigenvalue corresponding to the next angle on the orbit for a given resonance. This is accomplished by selecting the eigenvalue that exhibits the closest proximity to the eigenvalue of the current angle, utilizing a suitable distance metric. The grouping algorithm allows filtering the eigenvalues corresponding to the EP and hence simplifies obtaining the initial training set. For all parameter values, e.g. field strengths, the centroid and the difference of the eigenvalues can be calculated respectively. These are passed to the GPR model together with the field strengths. Thus, the latter provides a prediction of

these quantities as a function of the field strengths. Due to the degeneracy at the EP, the eigenvalue difference has to be zero at this point, which is why a two-dimensional root search applied to the model provides a prediction for the position of the EP in the field plane. A diagonalization with the predicted field strengths was performed to obtain the exact eigenvalues. These were added to the training set to improve the prediction of the model. Hence, an iterative process was established. In higher-dimensional systems, diagonalization involves computing more than just the two eigenvalues associated with the EP. Selecting the correct eigenvalues in each iteration was achieved by introducing a similarity measure in Section 4.3, which compares the model prediction with the exact eigenvalues. This so-called compatibility c is defined in Equation (4.7). The smallest c value should correspond to the eigenvalue pair belonging to the EP. To ensure proper selection, a large gap between the smallest and second smallest c value is desirable, which was indeed observed. To determine the convergence of this method, several convergence criteria were discussed in Section 4.4. A combination of the drop in the kernel eigenvalues and the difference of the eigenvalues associated with the EP appeared to be a promising convergence criterion. Training the GPR model and applying the method resulted in a relatively fast convergence to the EP with a high accuracy.

Prior to applying the GPR method for identifying EPs in Cu_2O, it was necessary to perform scaling and projection operations (cf. Appendix B) on the centroid and the difference of the eigenvalues, as well as the field strengths. This preprocessing step served to standardize and enhance the training procedure of the GPR model, providing a more generalized and optimized approach. For small relative radii (see Equation (5.4)) of the orbit around the EP the method yielded promising results, but in order to minimize the computational cost a large convergence radius would be favorable. Hence, in Section 5.2, convergence was investigated for very large radii of $\varrho = 6\,\%$, which corresponds to $\Delta\gamma = 77.733\,\mathrm{mT}$ and $\Delta f = 5.1966\,\mathrm{V/cm}$ in the specified case. The method converged to the prediction of the small radius after only ten diagonalizations with high accuracy. This radius of $\varrho = 6\,\%$ does not represent the largest convergence radius. The largest one tested was $\varrho = 15\,\%$, which corresponds to $\Delta\gamma = 319.650\,\mathrm{mT}, \Delta f = 20.558\,\mathrm{V/cm}$. The remarkable results obtained with a relatively small number of training steps and the notable precision achieved point to the possibility of an even larger convergence radius. While filtering the permutation of the eigenvalues for the large ellipse, additional permutations were obtained which could not be visibly distinguished due to a huge overlap with other resonances. Thus, not only the computational cost is reduced drastically with the new GPR method due to its large convergence radius, but also the stepwise grouping

algorithm provides additional training sets for different EPs, reducing the computational and time effort even further.

Within the scope of this research, a Python package called Search-for-EPs was developed and made publicly available. The package is primarily tailored to address the specific challenges and requirements encountered in this study, as well as being compatible with other software utilized in this thesis. Nonetheless, certain functions within the package can be applied to other problem domains as well, e.g. the stepwise grouping algorithm. Documentation for the package is also provided to facilitate its effective usage.

Future theoretical work should focus on the search for experimental accessible EPs. Oscillator strengths and other parameters need to be considered in the evaluation. Due to the questionable convergence of the EPs in Table 5.1, related to the diagonalization of the Hamiltonian, further tests are necessary to get accurate predictions. Of course promising EPs should be investigated experimentally. This could be done at the TU Dortmund using high-resolution spectroscopy [11, 47].

References

[1] W P Reinhardt. "Complex Coordinates in the Theory of Atomic and Molecular Structure and Dynamics". In: *Annual Review of Physical Chemistry* 33.1 (1982), pp. 223–255. DOI: 10.1146/annurev.pc.33.100182.001255.

[2] W. D. Heiss. "Repulsion of Resonance States and Exceptional Points". In: *Physical Review E* 61.1 (2000), pp. 929–932. DOI: 10.1103/PhysRevE.61.929.

[3] Holger Cartarius, Jörg Main, and Günter Wunner. "Exceptional Points in Atomic Spectra". In: *Physical Review Letters* 99.17 (2007), p. 173003. DOI: 10.1103/PhysRevLett.99.173003.

[4] T. Kazimierczuk, D. Fröhlich, S. Scheel, H. Stolz, and M. Bayer. "Giant Rydberg Excitons in the Copper Oxide Cu_2O". In: *Nature* 514.7522 (2014), pp. 343–347. DOI: 10.1038/nature13832.

[5] Raam Uzdin and Roland Lefebvre. "Finding and Pinpointing Exceptional Points of an Open Quantum System". In: *Journal of Physics B: Atomic, Molecular and Optical Physics* 43.23 (2010), p. 235004. DOI: 10.1088/0953-4075/43/23/235004.

[6] Matthias Feldmaier, Jörg Main, Frank Schweiner, Holger Cartarius, and Günter Wunner. "Rydberg Systems in Parallel Electric and Magnetic Fields: An Improved Method for Finding Exceptional Points". In: *Journal of Physics B: Atomic, Molecular and Optical Physics* 49.14 (2016), p. 144002. DOI: 10.1088/0953-4075/49/14/144002.

[7] Carl Edward Rasmussen and Christopher K. I. Williams. *Gaussian Processes for Machine Learning*. MIT Press, 2005. DOI: 10.7551/mitpress/3206.001.0001.

[8] Patric Rommel. "Theory of Yellow and Green Excitons in Cuprous Oxide with Emphasis on Correction Terms and External Fields". PhD thesis. University of Stuttgart, 2022. DOI: 10.18419/opus-12357.

[9] Patrick Egenlauf. "Suche nach exzeptionellen Punkten bei Exzitonen in Kupferoxydul in äußeren Feldern unter Berücksichtigung der Bandstruktur". Bachelor's thesis. University of Stuttgart, 2020. DOI: 10.18419/opus-11120.

[10] Frank Schweiner. "Theory of Excitons in Cuprous Oxide". PhD thesis. University of Stuttgart, 2017. DOI: 10.18419/opus-9483.

[11] Frank Schweiner, Jörg Main, Günter Wunner, Marcel Freitag, Julian Heckötter, Christoph Uihlein, Marc Aßmann, Dietmar Fröhlich, and Manfred Bayer. "Magnetoexcitons in Cuprous Oxide". In: *Physical Review B* 95.3 (2017), p. 035202. DOI: 10.1103/PhysRevB.95.035202.

[12] Frank Schweiner, Jörg Main, Matthias Feldmaier, Günter Wunner, and Christoph Uihlein. "Impact of the Valence Band Structure of Cu_2O on Excitonic Spectra". In: *Physical Review B* 93.19 (2016), p. 195203. DOI: 10.1103/PhysRevB.93.195203.

[13] G. F. Koster, J. O. Dimmock, R. G. Wheeler, and H. Statz. *Properties of the Thirty-Two Point Groups*. Massachusetts institute of technology press research monograph. M.I.T. Press, Cambridge 1963.

[14] J. M. Luttinger and W. Kohn. "Motion of Electrons and Holes in Perturbed Periodic Fields". In: *Physical Review* 97.4 (1955), pp. 869–883. DOI: 10.1103/PhysRev.97.869.

[15] K. Suzuki and J. C. Hensel. "Quantum Resonances in the Valence Bands of Germanium. I. Theoretical Considerations". In: *Physical Review B* 9.10 (1974), pp. 4184–4218. DOI: 10.1103/PhysRevB.9.4184.

[16] F. Schöne, S.-O. Krüger, P. Grünwald, H. Stolz, S. Scheel, M. Aßmann, J. Heckötter, J. Thewes, D. Fröhlich, and M. Bayer. "Deviations of the Exciton Level Spectrum in Cu_2O from the Hydrogen Series". In: *Physical Review B* 93.7 (2016), p. 075203. DOI: 10.1103/PhysRevB.93.075203.

[17] M. French, R. Schwartz, H. Stolz, and R. Redmer. "Electronic Band Structure of Cu_2O by Spin Density Functional Theory". In: *Journal of Physics: Condensed Matter* 21.1 (2008), p. 015502. DOI: 10.1088/0953-8984/21/1/015502.

[18] P. Schmelcher and L. S. Cederbaum. "Regularity and Chaos in the Center of Mass Motion of the Hydrogen Atom in a Magnetic Field". In: *Zeitschrift für Physik D Atoms, Molecules and Clusters* 24.4 (1992), pp. 311–323. DOI: 10.1007/BF01426678.

[19] J. E Avron, I. W Herbst, and B Simon. "Separation of Center of Mass in Homogeneous Magnetic Fields". In: *Annals of Physics* 114.1 (1978), pp. 431–451. DOI: 10.1016/0003-4916(78)90276-2.

[20] Frank Schweiner, Jan Ertl, Jörg Main, Günter Wunner, and Christoph Uihlein. "Exciton-Polaritons in Cuprous Oxide: Theory and Comparison with Experiment". In: *Physical Review B* 96.24 (2017), p. 245202. DOI: 10.1103/PhysRevB.96.245202.

[21] H. Haken. "Kopplung nichtrelativistischer Teilchen mit einem quantisierten Feld". In: *Il Nuovo Cimento (1955-1965)* 3.6 (1956), pp. 1230–1253. DOI: 10.1007/BF02785005.

[22] H. Haken and W. Schottky. "Die Behandlung des Exzitons nach der Vielelektronentheorie". In: *Zeitschrift für Physikalische Chemie* 16 (3_6 1958), pp. 218–244. DOI: 10.1524/zpch.1958.16.3_6.218.

[23] H. Haken. "Die Theorie des Exzitons im festen Körper". In: *Fortschritte der Physik* 6.6 (1958), pp. 271–334. DOI: 10.1002/prop.19580060602.

[24] Frank Schweiner, Jörg Main, Günter Wunner, and Christoph Uihlein. "Even Exciton Series in Cu_2O". In: *Physical Review B* 95.19 (2017), p. 195201. DOI: 10.1103/PhysRevB.95.195201.

[25] G. M. Kavoulakis, Yia-Chung Chang, and Gordon Baym. "Fine Structure of Excitons in Cu_2O". In: *Physical Review B* 55.12 (1997), pp. 7593–7599. DOI: 10.1103/PhysRevB.55.7593.

[26] J. W. Hodby, T. E. Jenkins, C. Schwab, H. Tamura, and D. Trivich. "Cyclotron Resonance of Electrons and of Holes in Cuprous Oxide, Cu_2O". In: *Journal of Physics C: Solid State Physics* 9.8 (1976), p. 1429. DOI: 10.1088/0022-3719/9/8/014.

[27] O. Madelung, U. Rössler, and M. Schulz. *Landolt-Börnstein - Group III Condensed Matter*. Springer-Verlag: Berlin, 1998.

[28] Howard E. Swanson and Ruth K. Fuyat. *Standard X-Ray Diffraction Powder Patterns*. Vol. II. 53. NBS Circular 539, 1953.

[29] Sergey Artyukhin. "Frustrated Magnets: Non-Collinear Spin Textures, Excitations and Dynamics". Thesis fully internal (DIV). Groningen: s.n., 2012.

[30] Patrik Zielinski. "Berechnung hochangeregter Exzitonen in elektrischen und magnetischen Feldern mit der Methode der komplexen Koordinatenrotation". Master's thesis. University of Stuttgart, 2018. DOI: 10.18419/opus-10130.

[31] Nimrod Moiseyev. "Quantum Theory of Resonances: Calculating Energies, Widths and Cross-Sections by Complex Scaling". In: *Physics Reports* 302.5 (1998), pp. 212–293. DOI: 10.1016/S0370-1573(98)00002-7.

[32] Holger Cartarius. "Exceptional Points in Atomic Spectra and Bose-Einstein Condensates". PhD thesis. 2008. DOI: 10.18419/opus-4844.

[33] J. Zamastil, F. Vinette, and M. Šimánek. "Calculation of Atomic Integrals Using Commutation Relations". In: *Physical Review A* 75.2 (2007), p. 022506. DOI: 10.1103/PhysRevA.75.022506.

[34] M. A. Caprio, P. Maris, and J. P. Vary. "Coulomb-Sturmian Basis for the Nuclear Many-Body Problem". In: *Physical Review C* 86.3 (2012), p. 034312. DOI: 10.1103/PhysRevC.86.034312.

[35] R. B. Lehoucq, D. C. Sorensen, and C. Yang. *ARPACK Users' Guide*. Software, Environments, and Tools. Society for Industrial and Applied Mathematics, 1998. 150 pp. DOI: 10.1137/1.9780898719628.

[36] Tosio Kato. *Perturbation Theory for Linear Operators*. Berlin, Heidelberg: Springer, 1966. DOI: 10.1007/978-3-662-12678-3.

[37] Matthias Feldmaier. "Untersuchung exzeptioneller Punkte bei Exzitonen in parallelen elektrischen und magnetischen Feldern". Master's thesis. University of Stuttgart, 2015. DOI: 10.18419/opus-10128.

[38] W. D. Heiss. "The Physics of Exceptional Points". In: *Journal of Physics A: Mathematical and Theoretical* 45.44 (2012), p. 444016. DOI: 10.1088/1751-8113/45/44/444016.

[39] Konrad Knopp. *Theory of Functions, Parts I and II*. Dover Edition. Mineola, N.Y: DOVER PUBN INC, 1996. 320 pp.

[40] W.D. Heiss. "Phases of Wave Functions and Level Repulsion". In: *The European Physical Journal D - Atomic, Molecular, Optical and Plasma Physics* 7.1 (1999), pp. 1–4. DOI: 10.1007/s100530050339.

[41] Edward Snelson and Zoubin Ghahramani. "Sparse Gaussian Processes Using Pseudo-Inputs". In: *Advances in Neural Information Processing Systems*. Ed. by Y. Weiss, B. Schölkopf, and J. Platt. Vol. 18. MIT Press, 2005.

[42] David JC MacKay. "Introduction to Gaussian Processes". In: *NATO ASI series F computer and systems sciences* 168 (1998), pp. 133–166.

[43] Jie Wang. *An Intuitive Tutorial to Gaussian Processes Regression*. 2022. DOI: 10.48550/arXiv.2009.10862. (Visited on 06/28/2023). preprint.

[44] James Mercer and Andrew Russell Forsyth. "XVI. Functions of Positive and Negative Type, and Their Connection the Theory of Integral Equations". In: *Philosophical Transactions of the Royal Society of London. Series A, Containing Papers of a Mathematical or Physical Character* 209.441-458 (1909), pp. 415–446. DOI: 10.1098/rsta.1909.0016.

[45] Hongwei Sun. "Mercer Theorem for RKHS on Noncompact Sets". In: *Journal of Complexity* 21.3 (2005), pp. 337–349. DOI: 10.1016/j.jco.2004.09.002.

[46] Sanae Lotfi, Pavel Izmailov, Gregory Benton, Micah Goldblum, and Andrew Gordon Wilson. "Bayesian Model Selection, the Marginal Likelihood, and Generalization". In: *Proceedings of the 39th International Conference on Machine Learning*. International Conference on Machine Learning. PMLR, 2022, pp. 14223–14247.

[47] Patric Rommel, Frank Schweiner, Jörg Main, Julian Heckötter, Marcel Freitag, Dietmar Fröhlich, Kevin Lehninger, Marc Aßmann, and Manfred Bayer. "Magneto-Stark Effect of Yellow Excitons in Cuprous Oxide". In: *Physical Review B* 98.8 (2018), p. 085206. DOI: 10.1103/PhysRevB.98.085206.

A Implementation of the Stepwise Grouping Algorithm

Below, a Python implementation of the stepwise grouping algorithm, described in Section 4.1, is shown. The unsorted vector, denoted as `vec`, has a shape of (l, m, n), where l represents the number of steps taken along the orbit, m indicates the number of resonances, and n represents the dimension of the n-dimensional vector. This vector allows the combination of various quantities, such as real and imaginary part of the eigenvalue and quantum numbers. Due to the fact that in each iteration two angles are selected, the for loop goes over all steps l except the last one. After calculating the pairwise distance by using a function from `scikit-learn` and sorting each column of the resulting matrix by shortest distance, the condition in the while loop prevents multiple selection of the same resonance. At the end of each iteration the sorted step is inserted into a new array, which is returned in the end and is thus the sorted array.

This function can be found on the GitHub page of the package developed during this thesis under *searchep/data.py/stepwise_grouping*. The documentation contains additional information about the package and how to use it.

```python
import numpy as np
from sklearn.metrics import pairwise_distances
from scipy.spatial.distance import cosine


def stepwise_grouping(vec: np.ndarray, vec_normalized: np.ndarray = None)
    -> np.ndarray:

    vec_normalized = vec_normalized if vec_normalized else vec
    vec_sorted = [vec[0]]
    vec_sorted_normalized = [vec_normalized[0]]
        for angle in range(vec.shape[0]-1):
```

```
12          current_angle = vec_sorted_normalized[angle]
13          next_angle = vec_normalized[angle+1]
14          nn_distance = pairwise_distances(next_angle, current_angle,
             ↪  metric='cosine')
15          nn_index = np.argsort(nn_distance, axis=0)
16          while len(nn_index[0]) > len(set(nn_index[0])):
17              u, inverse, counts = np.unique(nn_index[0],
                 ↪  return_inverse=True, return_counts=True)
18              index_multi_min = u[np.argmax(counts)]
19              unique_min = current_angle[np.where(inverse ==
                 ↪  np.argmax(counts))] - next_angle[index_multi_min]
20              index_current_angle = np.where(inverse ==
                 ↪  np.argmax(counts))[0][np.argmin(np.linalg.norm(unique_min,
                 ↪  axis=1))]
21              nn_index = np.column_stack([np.append(nn_index[:,
                 ↪  i][(nn_index[:, i] != index_multi_min)],
                 ↪  [index_multi_min])if i != index_current_angle else
                 ↪  nn_index[:, index_current_angle] for i in
                 ↪  range(nn_index.shape[1])])
22          vec_sorted.append(vec[angle+1][nn_index[0]])
23          vec_sorted_normalized.append(vec_normalized[angle+1][nn_index[0]])
24      vec_sorted = np.array(vec_sorted)
25      return vec_sorted
```

B Optimization of the Training Process

In order to optimize the training process and thus obtain more accurate results, two aspects need to be addressed, namely the varying radius of the orbits and the small energy eigenvalues. Since two separate programs are used, one for the diagonalization of the Hamiltonian and one for the GPR method, it is not as straightforward to project the field strengths onto the unit circle as depicted in Equations (5.1) to (5.3). For the following discussion κ is calculated via

$$\kappa = \gamma + \mathrm{i}f\,. \tag{B.1}$$

The GPR method requires κ to train the GPR model, but the diagonalization only provides γ and f. Thus, this is the simplest approach to implement in the GPR program.

B.1 Projection of the field strengths on the unit circle

To obtain a more generalized training set, the input, i.e. the κ points on the orbit, are projected onto the unit circle. This can be accomplished via

$$\begin{aligned}\kappa_\mathrm{c} = &\left(\frac{1}{2}\cdot\left[\max\left(\mathrm{Re}(\kappa_i) : i = 1,\dots,n\right) + \min\left(\mathrm{Re}(\kappa_i) : i = 1,\dots,n\right)\right]\right)\\ &+\mathrm{i}\left(\frac{1}{2}\cdot\left(\max\left(\mathrm{Im}(\kappa_i) : i = 1,\dots,n\right) + \min\left(\mathrm{Im}(\kappa_i) : i = 1,\dots,n\right)\right)\right)\,,\end{aligned} \tag{B.2}$$

$$\begin{aligned}\kappa_i \rightarrow &\frac{\mathrm{Re}(\kappa_i - \kappa_\mathrm{c})}{\max\left(\mathrm{Re}(\kappa_i) - \mathrm{Re}(\kappa_\mathrm{c}) : i = 1,\dots,n\right)}\\ &+\mathrm{i}\frac{\mathrm{Im}(\kappa_i - \kappa_\mathrm{c})}{\max\left(\mathrm{Im}(\kappa_i) - \mathrm{Im}(\kappa_\mathrm{c}) : i = 1,\dots,n\right)}\,.\end{aligned} \tag{B.3}$$

First the center of the orbit κ_c is calculated. Due to the discrete steps it is necessary to work with the min and max functions. Then, all κ_i are projected to their corresponding position on the unit circle. Hence, the input of the GPR model is independent of the relative as well as the absolute radius of the ellipse in the field plane.

B.2 Rescaling of the function values $\boldsymbol{p}$ and $\boldsymbol{s}$

Because of the already quite small energy eigenvalues of order $\mathcal{O}(10^{-6})$ their respective p values in Equation (2.55) are of order $\mathcal{O}(10^{-12})$. The GPR model does not yield accurate predictions, due to the fact that it assumes the function values to be zero. Thus, rescaling these function values is not only helpful to obtain a generalized training set, but also necessary for the model to provide good predictions. This scaling is given by

$$\boldsymbol{p}_i \to \frac{\boldsymbol{p}_i}{\max((|\mathrm{Re}(p_i)| : i = 1, \dots, n), (|\mathrm{Im}(p_i)| : i = 1, \dots, n))}\,, \tag{B.4}$$

$$\bar{s}_{\mathrm{Re}} = \frac{1}{N}\sum_{i=1}^{N} \mathrm{Re}(s_i) \tag{B.5}$$

$$\bar{s}_{\mathrm{Im}} = \frac{1}{N}\sum_{i=1}^{N} \mathrm{Im}(s_i) \tag{B.6}$$

$$\boldsymbol{s}_i \to \frac{\boldsymbol{s}_i - \begin{pmatrix} \bar{s}_{\mathrm{Re}} \\ \bar{s}_{\mathrm{Im}} \end{pmatrix}}{\max\left((|\mathrm{Re}(s_i) - \bar{s}_{\mathrm{Re}}| : i = 1, \dots, n)\,, (|\mathrm{Im}(s_i) - \bar{s}_{\mathrm{Im}}| : i = 1, \dots, n)\right)}\,. \tag{B.7}$$

Since a two-dimensional zero search is performed for $\boldsymbol{p}$ to obtain a prediction of the position of the EP, it is important to fix the zero values to their actual positions while rescaling. The rescaled function values lie in the intervals $[-1, 1]$ and $[-\mathrm{i}, \mathrm{i}]$ for the real and imaginary part respectively. For $\boldsymbol{s}$, which is employed only to identify the two eigenvalues after each training step that belong to the EP, a similar scaling operation is used to project the function values onto the same intervals.

Zusammenfassung in Deutscher Sprache

Das Anlegen von äußeren magnetischen und elektrischen Feldern an Exzitonen in Kupferoxydul führt zu Resonanzen, also zu quasi-gebundenen Zuständen, welche zerfallen können und einen komplexen Energieeigenwert besitzen. Der Imaginärteil beschreibt dabei die Lebensdauer des Zustands. Bei bestimmten Feldstärken können exzeptionelle Punkte (EPs) auftreten, bei denen sowohl die Eigenwerte als auch die Eigenvektoren von zwei Resonanzen miteinander verschmelzen. Eine Eigenschaft dieser EPs ist, dass bei einer Umlaufbahn um den EP in der Feldebene die beiden zu diesem EP gehörenden Eigenwerte permutieren, d.h. sie tauschen ihre Positionen. Die Bestimmung von EPs ist kompliziert, vor allem wegen der hohen Rechenkosten für die Diagonalisierung des Exzitonen-Hamiltonians von Cu_2O. Aufgrund dieser hohen Rechenkosten sind die existierenden Methoden um EPs zu finden, welche auf einer mehrdimensionalen Taylorentwicklung um den EP basieren, ineffizient oder sogar nicht anwendbar. Daher wurde in dieser Arbeit eine neue Methode zur Bestimmung von EPs entwickelt.

In Kapitel 3 wurde das Konzept von Gauß'schen Prozessen (GPs) im Rahmen des maschinellen Lernens eingeführt. Indem man eine Verteilung über Funktionen festlegt und nur diejenigen berücksichtigt, die auf die beobachteten Datenpunkte passen, können Vorhersagen für neue Datenpunkte gemacht werden, wobei eine Modellunsicherheit für diese Vorhersagen angegeben wird. Dieser Gaussian process regression (GPR) Ansatz wurde in der neuen Methode verwendet.

Die GPR Methode wurde schrittweise mit Hilfe von Matrixmodellen in Kapitel 4 entwickelt. Ein Satz von Eigenwertpaaren bei verschiedenen Parameterwerten, z.B. Feldstärken, wurde als anfänglicher Trainingssatz verwendet. In höherdimensionalen Systemen ist es nicht trivial, die Eigenwerte auszuwählen, welche zum EP gehören, da sie sich mit anderen Resonanzen überschneiden. Die größte Herausforderung bestand darin, die beiden zum EP gehörenden Eigenwerte herauszufiltern. Deshalb wurde in Abschnitt 4.1 der schrittweise Gruppieralgorithmus entwickelt, um die entsprechenden

Eigenwerte zu identifizieren und somit den anfänglichen Trainingsdatensatz zu erhalten. Das diesem Algorithmus zugrunde liegende Prinzip besteht darin, den Eigenwert zu bestimmen, der dem nächsten Winkel auf der Umlaufbahn für eine bestimmte Resonanz entspricht. Dies geschieht durch die Auswahl des Eigenwerts, der dem Eigenwert des aktuellen Winkels am nächsten liegt, wobei eine geeignete Abstandsmetrik verwendet wird. Der Gruppieralgorithmus ermöglicht das Filtern der entsprechenden Eigenwerte und macht es somit unkompliziert die anfängliche Trainingsmenge zu erhalten. Diese besteht aus den errechneten Schwerpunkten und Differenzen der Eigenwerte für alle Feldstärken. Durch das Trainieren des GPR Modells mit diesen Daten liefert dieses eine Vorhersage dieser Größen in Abhängigkeit der Feldstärken. Aufgrund der Entartung am EP muss die Eigenwertdifferenz dort Null ergeben, weshalb eine zweidimensionale Nullstellensuche angewandt auf das Modell eine Vorhersage für die Position des EP in der Feldebene liefert. Eine Diagonalisierung mit den vorhergesagten Feldstärken ergibt die genauen Eigenwerte an diesem Punkt. Diese wurden dem Datensatz, welcher für das Training verwendet wurde, hinzugefügt, um die Vorhersage des Modells zu verbessern. Auf diese Weise wurde ein iterativer Prozess aufgebaut. In höherdimensionalen Systemen werden bei der Diagonalisierung mehr als nur die Eigenwerte, welche zum EP gehören, berechnet. Die Auswahl der richtigen Eigenwerte in jeder Iteration erfolgte durch die Einführung eines Ähnlichkeitsmaßes in Abschnitt 4.3, welches die Modellvorhersage mit den exakten Eigenwerten vergleicht. Diese sogenannte Kompatibilität c ist in Gleichung (4.7) definiert. Der kleinste Wert von c sollte dem Eigenwertpaar entsprechen, das zum EP gehört. Um eine korrekte Auswahl zu gewährleisten, ist ein großer Abstand zwischen dem kleinsten und dem zweitkleinsten c Wert wünschenswert, was auch tatsächlich beobachtet wurde. Um die Konvergenz dieser Methode zu bestimmen, wurden in Abschnitt 4.4 mehrere Konvergenzkriterien diskutiert. Als vielversprechendes Konvergenzkriterium erwies sich eine Kombination aus dem Abfall der Kernel-Eigenwerte und der Differenz der zum EP gehörenden Eigenwerte. Das Training des GPR Modells und die Anwendung der Methode führten mit hoher Genauigkeit zu einer relativ schnellen Konvergenz zum EP.

Vor der Anwendung der GPR Methode zur Identifizierung von EPs in Cu_2O war es notwendig, Skalierungs- und Projektionsoperationen (vgl. Anhang B) am Schwerpunkt der Eigenwerte und der Eigenwertdifferenz sowie an den Feldstärken durchzuführen. Dieser Vorverarbeitungsschritt der Daten diente dazu, das Trainingsverfahren des GPR Modells zu standardisieren und zu verbessern, um einen allgemeineren und optimierten Ansatz zu erhalten. Für kleine Radien (siehe Gleichung (5.4)) der Umlaufbahn um den EP lieferte die Methode vielversprechende Ergebnisse, aber um die Rechenkosten zu mi-

nimieren, wäre ein großer Konvergenzradius vorteilhaft. Daher wurde in Abschnitt 5.2 die Konvergenz für sehr große Radien von $\varrho = 6\,\%$ untersucht, was im angegebenen Fall $\Delta\gamma = 77{,}733\,\mathrm{mT}$ und $\Delta f = 5{,}1966\,\mathrm{V/cm}$ entspricht. Die Methode konvergierte nach nur zehn Diagonalisierungen mit hoher Genauigkeit gegen die Vorhersage des kleinen Radius. Dieser Radius von $\varrho = 6\,\%$ entspricht nicht dem größten Konvergenzradius. Der größte getestete Wert war $\varrho = 15\,\%$, was $\Delta\gamma = 319{,}650\,\mathrm{mT}, \Delta f = 20{,}558\,\mathrm{V/cm}$ entspricht. Die hervorragenden Ergebnisse, die mit einer relativ geringen Anzahl an Trainingsschritten erzielt wurden, und die hohe Genauigkeit lassen einen noch größeren Konvergenzradius vermuten. Beim Filtern der Permutationen der Eigenwerte für die große Ellipse ergaben sich zusätzliche Permutationen, die aufgrund einer großen Überlappung mit anderen Resonanzen nicht sichtbar unterschieden werden konnten. Mit der neuen GPR-Methode wird also nicht nur der Rechenaufwand aufgrund ihres großen Konvergenzradius drastisch reduziert, sondern der schrittweise Gruppieralgorithmus liefert auch zusätzliche Trainingsdaten für verschiedene EPs, was den Rechen- und Zeitaufwand noch weiter verringert. Aufgrund dieser Vorteile konnten zwölf EPs bei realisierbaren Feldstärken ermittelt werden, welche an der TU Dortmund experimentell untersucht werden können.

Im Rahmen dieser Forschung wurde ein Python-Paket namens Search-for-EPs entwickelt und veröffentlicht. Das Paket wurde in erster Linie auf die spezifischen Herausforderungen und Anforderungen dieser Forschungsarbeit zugeschnitten und ist mit anderer in dieser Arbeit verwendeter Software kompatibel. Nichtsdestotrotz können bestimmte Funktionen innerhalb des Pakets auch auf andere Bereiche angewendet werden, beispielsweise der schrittweise Gruppieralgorithmus. Eine Dokumentation für das Paket wird ebenfalls zur Verfügung gestellt, um seine effektive Nutzung zu erleichtern.

Danksagung

An dieser Stelle möchte ich mich bei allen bedanken, die mich beim Schreiben dieser Arbeit unterstützt haben.

- Ein besonderer Dank geht an Prof. Dr. Jörg Main, der mir das Schreiben dieser Arbeit erst ermöglicht hat. Danke für die gute Betreuung!
- Danke auch an Dr. Patric Rommel, welcher mir die Daten zum Trainieren meiner Modelle lieferte und an den ich mich bei Fragen jederzeit wenden konnte.
- Thanks to Samuel James Tovey, who helped me especially at the beginning of this work with programming and understanding GPR.
- Danke an Prof. Dr. Christian Holm, welcher die Rolle des Zweitprüfers übernommen hat.
- Vielen Dank auch an meine Eltern, die mich während des ganzen Studiums unterstützt haben und ohne die studieren so nicht möglich gewesen wäre!
- Danke an alle Kollegen am ITP1 für die schöne Zeit und die freundliche und entspannte Atmosphäre.
- Thanks to the ML journal club, which gave me a deeper insight into the field of machine learning.
- Vielen Dank an Melina, die mich während der kompletten Arbeit immer unterstützt hat!
- Zu guter Letzt vielen Dank an alle die Korrektur gelesen haben!
  Last but not least, thanks to all who have proofread!

Erklärung

Ich versichere,

- dass ich diese Masterarbeit selbstständig verfasst habe,
- dass ich keine anderen als die angegebenen Quellen benutzt und alle wörtlich oder sinngemäß aus anderen Werken übernommenen Aussagen als solche gekennzeichnet habe,
- dass die eingereichte Arbeit weder vollständig noch in wesentlichen Teilen Gegenstand eines anderen Prüfungsverfahrens gewesen ist,
- und dass das elektronische Exemplar mit den anderen Exemplaren übereinstimmt.

Stuttgart, den 12. Juli 2023 *Patrick Egenlauf*